

INFORMATION TO USERS

This manuscript has been reproduced from the microfilm master. UMI films the text directly from the original or copy submitted. Thus, some thesis and dissertation copies are in typewriter face, while others may be from any type of computer printer.

The quality of this reproduction is dependent upon the quality of the copy submitted. Broken or indistinct print, colored or poor quality illustrations and photographs, print bleedthrough, substandard margins, and improper alignment can adversely affect reproduction.

In the unlikely event that the author did not send UMI a complete manuscript and there are missing pages, these will be noted. Also, if unauthorized copyright material had to be removed, a note will indicate the deletion.

Oversize materials (e.g., maps, drawings, charts) are reproduced by sectioning the original, beginning at the upper left-hand corner and continuing from left to right in equal sections with small overlaps. Each original is also photographed in one exposure and is included in reduced form at the back of the book.

Photographs included in the original manuscript have been reproduced xerographically in this copy. Higher quality 6" x 9" black and white photographic prints are available for any photographs or illustrations appearing in this copy for an additional charge. Contact UMI directly to order.

UMI

A Bell & Howell Information Company
300 North Zeeb Road, Ann Arbor MI 48106-1346 USA
313/761-4700 800/521-0600

Electromagnetic Wave Propagation and Scattering
in Dense, Discrete Random Media
with Application to Remote Sensing of Snow

by

Lisa M. Zurk

A dissertation submitted in partial fulfillment

of the requirements for the degree of

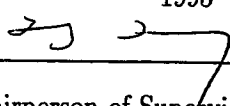
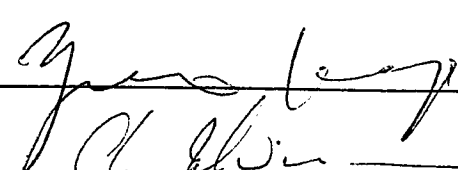
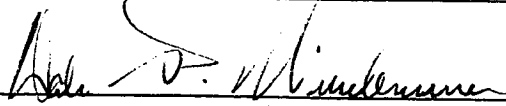
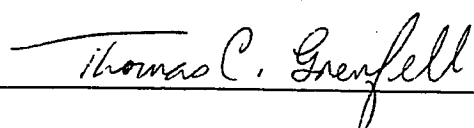
Doctor of Philosophy

University of Washington

1995

Approved by

(Chairperson of Supervisory Committee)

Program Authorized

to Offer Degree

Electrical Engineering

Date

12/16/95

UMI Number: 9616693

UMI Microform 9616693
Copyright 1996, by UMI Company. All rights reserved.

**This microform edition is protected against unauthorized
copying under Title 17, United States Code.**

UMI
300 North Zeeb Road
Ann Arbor, MI 48103

Doctoral Dissertation

In presenting this dissertation in partial fulfillment of the requirements for the Doctoral degree at the University of Washington, I agree that the Library shall make its copies freely available for inspection. I further agree that extensive copying of this dissertation is allowable only for scholarly purposes, consistent with "fair use" as prescribed in the U.S. Copyright Law. Requests for copying or reproduction of this dissertation may be referred to University Microfilms, 1490 Eisenhower Place, P.O. Box 975, Ann Arbor, MI 48106, to whom the author has granted "the right to reproduce and sell (a) copies of the manuscript and/or (b) printed copies of the manuscript from microform".

Signature Julia M Zink

Date 12/6/95

University of Washington

Abstract

Electromagnetic Wave Propagation and Scattering
in Dense, Discrete Random Media
with Application to Remote Sensing of Snow

by Lisa M. Zurk

Chairperson of Supervisory Committee: *Professor Leung Tsang*
 Electrical Engineering Department

This dissertation investigates wave propagation and scattering in dense, discrete random media using Monte Carlo simulations and analytic dense media theory. The Monte Carlo simulations use an exact numerical formulation based on the Foldy-Lax multiple scattering equations that allow computation of the incoherent field arising from scattering and absorption in systems of up to 5000 spheres with 40% fractional volume. The extinction coefficient obtained by simulation is compared to that obtained under classical methods and with dense media theory such as quasi-crystalline approximation (QCA) and quasi-crystalline approximation with coherent potential (QCA-CP). For dense media, the independent scattering approximation overestimates the amount of scattering while scattering calculated under QCA-CP agrees well with both simulation and carefully controlled experiment. At high fractional volumes the simulations predict a slightly larger extinction than QCA-CP. Monte Carlo simulations also predict the presence of absorption enhancement where the absorption coefficient exceeds that predicted under the independent absorption assumption.

The application of remote sensing of snow utilizes dense media radiative transfer

(DMRT) theory to predict the redistribution of radiant energy. Monte Carlo simulations provide a means to accurately determine the quantities necessary for DMRT, namely the extinction coefficient, absorption coefficient, phase matrix and effective permittivity. The phase matrix thus obtained differs from the classical assumption by containing non-zero off-diagonal elements while the effective permittivity agrees well with mixing formulae. A second order iterative solution to DMRT produces bi-static scattering levels that are comparable to those seen in actual snow data.

The effect of the scatterer placement on the electromagnetic wave is investigated by modeling the adhesive character of the particles that causes them to clump together with a sticky-particle pair distribution function. The adhesive character may provide a more accurate depiction of particles that exist in clusters (for example snow grains). The effect of the sticky-particles on the electromagnetic wave is calculated analytically using QCA and numerically with Monte Carlo simulations with both predicting much stronger scattering due to the larger particles. Snow sections prepared stereologically are analyzed to determine a family of pair distribution functions that can be used to calculate the scattering from a log-normal distribution of particle sizes.

TABLE OF CONTENTS

List of Figures	v
List of Tables	xii
Chapter 1: Introduction	1
1.1 Electromagnetic Wave scattering in Dense, Discrete Media	2
1.1.1 Monte Carlo Simulations	3
1.1.2 QCA and QCA-CP	4
1.2 Application to Remote Sensing of Snow Covered Regions	7
1.2.1 The Snow Medium Model	8
1.3 Overview of this dissertation	9
Chapter 2: Sticky Particles	12
2.1 Pair Distribution Function of the Sticky Sphere in the PY Approximation	13
2.2 QCA-CP Calculations with Sticky Particle Pair Function	19
2.3 Comparison with Results from Turbidity Studies	21
2.3.1 Description of the Turbidity Study	22
2.3.2 QCA-CP with the Adhesive Particles applied to the Turbidity Study	24
2.4 Equivalent Size Distributions	29
2.5 Conclusion	35
Chapter 3: Monte Carlo simulations for Sticky and Non-sticky Spheres	37

3.1	Sticky-Particle Placement	38
3.1.1	Placement for Higher Fractional Volumes	43
3.2	Solution of Multiple Scattering Equations	46
3.2.1	Absorption Calculation	49
3.2.2	Scattering Calculation	52
3.2.3	Choice of Statistical Sample	52
3.2.4	Computational Consideration	53
3.3	Results	56
3.3.1	Sticky and Non-Sticky Particles	56
3.3.2	Lossy Particles	62
3.4	Conclusions	66

Chapter 4:	Scattering Properties from Monte Carlo Simulations with Application to Remote Sensing of Snow	68
4.1	Radiative Transfer Equation	69
4.1.1	Classical Radiative Transfer	72
4.1.2	DMRT	73
4.1.3	Simulation	74
4.2	Monte Carlo Simulations	75
4.2.1	Calculation of the Phase Matrix	75
4.2.2	Configuration for Monte Carlo Simulations for Spherical Scatterers	79
4.3	Coherent Wave Calculations	80
4.3.1	Dipole Orientation	80
4.3.2	Effective Permittivity	83
4.4	Results	84
4.4.1	Phase Matrix from Monte Carlo Simulations	84

4.4.2	New De-polarization vs. Classical	86
4.4.3	Effective Media Calculations	93
4.4.4	Active Remote Sensing from a Layer of Snow	96
4.5	Discussion and Conclusions	102
Chapter 5:	Pair Function Retrieval from Planar Snow Sections	104
5.1	Introduction	104
5.2	Volume Pair Distribution Function from Section Data	106
5.2.1	Calculation of g_A	108
5.2.2	Solution of Hanisch's Equation	109
5.2.3	Results from Simulation	110
5.3	g_v and g_{ij}	112
5.3.1	Nonlinear Model Fit to get g_{ij} from g_v	112
5.3.2	Snow Subsections	115
5.3.3	Recovery of g_v	117
5.4	Scattering from a Distribution of Spheres	119
5.4.1	Independent Scattering and Correction Terms	121
5.4.2	Representative Particle Diameters	122
5.5	Results with Monte Carlo Data	124
5.5.1	Pair Functions and Scattering Calculations	125
5.5.2	Pair Function Retrieval	129
5.6	Scattering Calculations Based on Snow Section Data	136
5.6.1	Model Fit for g_v	136
5.7	Discussion and Conclusions	137
Chapter 6:	Conclusions and Recommendations	142
6.1	Summary of Research	143

6.1.1	Sticky Hard Sphere Pair Distribution Function	143
6.1.2	Monte Carlo Simulations	143
6.1.3	Radiative Transfer Equation Applied to Remote Sensing of Snow	145
6.1.4	Pair Function Retrieval from Planar Snow Sections	146
6.2	Recommendations for Future Research	147
6.2.1	Specific Recommendations	148
Bibliography		150

LIST OF FIGURES

1.1	Illustration of snow grain size vs. microwave wavelength	9
2.1	Percus Yevick Pair distribution function for sticky spheres with $\tau = 0.2$ and $\tau = 0.5$, and for non-sticky spheres and $f=0.3$	17
2.2	Percus Yevick Pair distribution function for sticky spheres with $f = 0.2$ and $f = 0.4$ and stickiness $\tau = 0.2$	18
2.3	Turbidity vs. Fractional Volume calculated with parameters in Table using QCA-CP-SHS	25
2.4	QCA-CP curves of Turbidity vs. Fractional Volume for non-sticky SE2 particles of radii 20, 30, 37.2, 40, 42, and 45 nm.(bottom to top curves), and a sticky SE2 particle of radius 37.2 nm.(shown by arrow)	27
2.5	QCA-CP curves of Turbidity vs. Fractional Volume for non-sticky SE2 particles of radii between 37.2 and 65 nm., and sticky SE2 particles of radius 37.2 nm. with $\tau = 0.2$ and $\tau = 0.4$	28
2.6	a) Gamma distribution with $b=30$ and $c=0.6$ b) Attenuation from : the gamma distribution (dashed), sticky $\tau = 0.2$ particles with radius 37.2 nm. (solid), and sticky $\tau = 0.4$ particles with radius 37.2 nm (dot-dash)	31
2.7	a) Bi-modal gamma distribution with 99% $b=15$, $c=0.5$ and 1% $b=40$, $c=0.6$ b) Attenuation from : the gamma distribution (dashed), sticky $\tau = 0.2$ particles with radius 37.2 nm. (solid), and sticky $\tau = 0.4$ particles with radius 37.2 nm (dot-dash)	33

2.8	a) Bi-modal gamma distribution with 95% $b=15$, $c=0.5$ and 5% $b=40$, $c=0.6$ b) Attenuation from : the gamma distribution (dashed), sticky $\tau = 0.2$ particles with radius 37.2 nm. (solid), and sticky $\tau = 0.4$ particles with radius 37.2 nm (dot-dash)	34
3.1	The pair distribution function calculated from Monte Carlo simulations and Percus-Yevick SHS with $\tau = 0.2$. Top plot is with $f_v = 0.1$ and bottom plot is with $f_v = .2$. The x-axis is $r/(2a)$ and the y-axis is normalized probability.	41
3.2	Three-dimensional computer generated view of aggregation of spheres with $f_v = 0.35$ and $\tau = 0.2$	42
3.3	The pair distribution function calculated from Monte Carlo simulations with a shuffling algorithm for a fractional volume of 40%. The y-axis is normalized probability.	45
3.4	The number of iterations vs. realizations for 3500 spheres that are 40% by volume with $ka = 0.2$. The initial realization has some periodicity which is destroyed by shuffling in later realizations, and thus randomness increases from left to right.	54
3.5	Extinction rate as a function of fractional volume; calculations based on independent assumption, QCA, QCA-CP, and Monte Carlo simulations for $ka = 0.2$	57
3.6	Extinction rate as a function of fractional volume; calculations based on independent assumption, QCA, QCA-CP, and Monte Carlo simulations for $ka = 0.1$	58

3.7	Extinction rate as a function of fractional volume for non-sticky spheres and sticky spheres with $\tau = 0.2$ and $\tau = 1.0$ and $ka = 0.2$; calculations based on independent assumption, QCA-CP and Monte Carlo simulations.	61
3.8	Normalized absorption, scattering and extinction from Monte Carlo simulations and independent Mie assumption for spheres with $\epsilon_s = (3.2 + i0.01)\epsilon_o$ and $ka = 0.2$. Monte Carlo results shown as (+) for absorption, (*) for scattering, and (o) for extinction. Independent absorption shown as dotted line, scattering as solid, and extinction as dash-dot.	63
3.9	Absorption rate as a function of size ka from Monte Carlo simulations of spheres with $f_v = .2$ for electric dipole and magnetic dipole.	64
4.1	Geometry of the radiative transfer problem for a planar layer of spherical scatters in region 1 covering a homogeneous half-space in region 2 where Z is normal to the planar interfaces. Elemental volume for calculation of radiative transfer parameters shown.	70
4.2	Monte Carlo Test Volume shown with incident electric field traveling in the $\hat{k}_i = \hat{z}$ direction and polarized in the $\hat{v}_i = \hat{y}$ direction. The cubic test volume has a side of length s and volume $v = s^3$. The scattered fields are in the direction θ_s and ϕ_s where Θ is the angle between \hat{k}_i and \hat{k}_s	77
4.3	Cartoon showing the internal dipole orientation due to incident excitation and scattered fields of surrounding particles	82

4.4	Elements of the phase matrix for an incident wave polarized perpendicular to the plane of incidence as a function of Θ . Results for spheres with $\epsilon_s = 3.2\epsilon_0$, 35% fractional volume and $a = 0.6$ mm. at 16 GHz. Monte Carlo results shown for non-sticky spheres (solid line) and sticky spheres with $\tau = 0.05$ (dash-dot line). Independent scattering shown as open circles.	87
4.5	Elements of the phase matrix for an incident wave polarized parallel to the plane of incidence as a function of Θ ; parameter values the same as the previous figure. Monte Carlo results shown for non-sticky spheres (solid line) and sticky spheres with $\tau = 0.05$ (dash-dot line). Independent scattering shown as open circles and spheroids with $c/a = 1.70$ shown as plus signs.	88
4.6	Depolarization level σ_{21}/σ_{11} (asterisk) and σ_{12}/σ_{22} (plus) as a function of the spheres' relative permittivity ϵ_s/ϵ_0	89
4.7	Depolarization level σ_{21}/σ_{11} (asterisk) and σ_{12}/σ_{22} (plus) as a function of fractional volume.	90
4.8	Magnitude of the x (dot-dash line) and z (dashed line) components of the internal dipole normalized to $ p_y $ and computed as specified in equation 4.25. Results shown for 20% fractional volume with 2500 spheres for $\epsilon_s = 3.2\epsilon_0$ (top) and $\epsilon_s = 2.2\epsilon_0$ (bottom). The x axis is the radius α_l/λ_0 of the spherical volume over which the sum is computed.	91
4.9	Real part of the effective permittivity ϵ_{eff} vs. fractional volume calculated from Monte Carlo simulations (shown as asterisk) and compared with Clausius Mossotti (dashed line) and QCA-CP (dotted line). . . .	94

4.10	$Re(p_y)$ vs. z/λ_0 where p_y is the averaged over constant z planes. Monte Carlo results (asterisk) shown for 20% fractional volume with 5000 spheres with $\epsilon_s = 3.2\epsilon_0$ in a cubic test volume. Also shown is $\cos(K_r z)$ for $K_r = k_0\sqrt{1.27}$ (dotted line) and $K_r = k_0$ (dashed line).	95
4.11	Backscattering as a function of snow depth for 16 GHz at $\theta_i = 19.31^\circ$ from a layer of snow with $a = 0.6$ mm., $\epsilon_s = 3.2\epsilon_0$ and 35% fractional volume. The dashed line is σ_{vv} and solid line is σ_{hv} . The four plots show results of the radiative transfer theory for the classical model (top left), DMRT model (top right), Monte Carlo simulations (bottom row) and sticky particles with $\tau = 0.01$ (bottom right).	97
4.12	Bistatic cross sections for the same parameters as in the previous plot except $\theta_s = 59^\circ$ and $\tau = 0.20$. The first order copolarized return is shown as a dotted line, the first order depolarization is shown as a dashed line, and the second order depolarization is shown as a dash-dot line.	100
4.13	Backscattering cross section for 17 GHz compared with data for a 47.5 cm. deep snow cover with grain radius $a = 0.56$ mm and fractional volume $fv = 0.2$. Data shown as circles (co-pol) and asertisks (de-pol); RT model with sticky spheres $\tau = 0.1$ shown as a dotted line (co-pol) and solid line (de-pol).	101
5.1	Left hand plot shows volume pair distribution function g_v normalized to r_0 recovered from computer simulation (solid line), calculated from Percus-Yevick (dotted line) and calculated from Monte Carlo volume (dashed line). Right-hand plot shows area pair distribution function g_A calculated from sections of computer simulation.	111
5.2	Snow section from March 3, 1993.	116

5.3	a) Recovered volume pair function g_v for particles in fig. 5.2 (solid line), g_v calculated from PY with five sizes (dotted line) and g_v calculated from PY with 100 sizes (dashed line). b) area pair function g_A from snow sections.	118
5.4	Calculations plotted versus particle diameters based on system of log-normally distributed spheres with $D_g = 0.52$ and $\sigma_d = 1.8$. a) Normalized densities for 200 sizes (dashed line) and discrete diameters 0.3, 0.5, 0.8, 1.0, 1.5, 3.0 and 4.0 mm (asterisks) b) Extinction $\Gamma(a_{st})$ for continuous sizes c) Extinction $\Gamma(a_{st})$ for discrete sizes d) Independent scattering (solid line) and derivative with respect to diameter (dotted line) for plot in b.	123
5.5	Pair functions calculated from Percus-Yevick (solid line) and Monte Carlo simulations (dotted line) for sizes $r_1 = 0.25$, $r_2 = 1.5r_1$, and $r_3 = 2.5r_1$ mm. and number densities $n_1 = 2964$, $n_2 = 956$, $n_3 = 29$. .	126
5.6	Pair functions and extinction rates for particles in fig. 5.5.	127
5.7	Recovered pair function for particles in fig. 5.5. The left hand plots show the total volume pair distribution function g_v and the right hand plots show the area pair function g_A . a) g_v is computed from Monte Carlo data b) g_A is obtained by solution of (5.3), c) g_v is obtained by solution of (5.3), d) g_A is computed from Monte Carlo data.	130
5.8	Examples of measured g_A and recovered g_v for the values in table 5.1.	133
5.9	Recovered pair functions for particles in fig. 5.5. Left panel shows the six basis functions with adjusted parameters. Right panel shows the total pair function computed Percus Yevick (solid line) and the modeled g_v (dotted line) as in (5.14).	135

5.10	Decay parameter μ_{ij} determined from Percus-Yevick for a three size system and shown as a function of $r_i + r_j$	138
5.11	Non-linear model fit for snow section in fig. 5.2 and five diameters 0.30, 0.50, 0.80, 1.00, 1.50 mm. Each pair function $X_k(r) = g_{ij}(r)$ is described by the parametric form in (5.16).	139
5.12	Non-linear model fit for snow section in fig. 5.2. The left panel shows the 15 pair functions g_{ij} and the right panel shows the total pair function g_v where the dotted line is the fit and the solid line is from the snow section.	140

LIST OF TABLES

2.1	Parameter Values	26
3.1	Numerical Results for lossless spheres with $ka = 0.2$ and $\epsilon_s = 3.2\epsilon_0$. .	59
3.2	Numerical Results for lossless spheres with $ka = 0.1$ and $\epsilon_s = 3.2\epsilon_0$. .	59
4.1	Scattering Coefficient for spheres with $a = 0.56$ mm. at 35% fractional volume and $\epsilon_s = 3.2\epsilon_0$	85
5.1	Parameter values for investigation of sampling dependencies.	131

ACKNOWLEDGMENTS

I would like to thank Professor Tsang for his assistance and patience when teaching me the fundamentals of wave propagation and scattering. I would also like to thank Professor Dale Winebrenner for his unflagging support and many discussions on the nature and practice of science. I am grateful for the opportunity to work in the Applied Physics Laboratory - the people and resources I found there were invaluable. I would like to acknowledge the assistance of Dr. Ding who collaborated with me on the sticky particle research and has been extremely helpful over the years. I would also like to acknowledge Dr. Shi and Dr. Robert Davis for their assistance on the snow section work, and Dr. Richard West for the use of his dense media code. I'd like to thank Professor Kuga and Professor Ishimaru for serving on my reading committee.

I would like to acknowledge the unwavering support I have received from my family and friends. They have provided me with the encouragement and confidence necessary to meet the challenges of the doctoral program. In particular I wish to express my gratitude to my husband Michel for his steadfast faith in me and his generous support during the last four years.

Chapter 1

INTRODUCTION

This dissertation investigates the correlated scattering in densely packed, discrete random scatterers using Monte Carlo simulations and analytic dense media theory. Simulation results are compared with those obtained under classic methods and with dense media theory such as quasi-crystalline approximation (QCA) and quasi-crystalline approximation with coherent potential (QCA-CP). For the application of active microwave remote sensing of snow covered regions, the Monte Carlo results are used to determine the scattering coefficient, absorption coefficient, effective permittivity and phase matrix for use in the dense media radiative transfer equations.

To investigate the effect of the scatterer placement on the electromagnetic wave a sticky-particle pair distribution function is introduced which includes the adhesive character of the particles that causes them to clump together. This adhesive character may provide a more accurate depiction of particles that exist in clusters (for example snow grains). The effect of the sticky-particles on the electromagnetic wave is calculated analytically using QCA and numerically with Monte Carlo simulations. To generate a more realistic description of snow, snow sections prepared for stereological analysis are used to determine a family of pair distribution functions that contribute to the scattering.

This chapter contains a brief review of the pertinent formulations in dense media theory followed by a description of snow as a random media. The last section of the chapter provides an overview of the remaining sections of the thesis.

1.1 *Electromagnetic Wave scattering in Dense, Discrete Media*

In general, a random medium can be described as either a collection of scatters distributed within a background medium, or as a continuous random medium with a large dielectric variation. The latter case is called the “random-medium” model where the material has dielectric properties that vary smoothly and randomly in space. Scattering of the electromagnetic wave is due to the randomly fluctuating part of the permittivity, and the spatial variability is described statistically. Strong fluctuation theory is an example of a random media model which has been applied to remote sensing problems [73, 74, 77].

This research will utilize the “discrete scattering” model where the randomly located dielectric variations are treated as discrete scatterers and the geometric organization of the particles is introduced into the model. A *dense* discrete random medium is one in which the randomly distributed scatterers occupy a significant portion of the volume (more than a few percent by volume). Dry snow is an example of a dense media in which the fractional volume of the scatterers (ice grains) is between 10% and 40%. The discrete scatterer model has been used to compute scattering from a half-space of scatterers [80] and to determine thermal emission from snow [29].

To calculate scattering from an ensemble of particles the classic assumption is that of independent scattering, which states that the extinction rate is $n_0\sigma_e$, where n_0 is the number of particles per unit volume and σ_e is the extinction cross section of an individual particle [38]. An important feature of a discrete random medium with densely packed scatterers is that the correlation of the particles’ positions affects the scattering physics and invalidates the independent scattering assumption. This has been shown both experimentally [39, 44, 47] and theoretically [89, 92]. Likewise, Foldy’s approximation [31], which has been successful in propagation problems through tenuous medium, is not applicable. This is because the dense scatterer packing gives rise to correlated scattering between the particles and dense medium theory

that includes these effects must be used for accurate results.

Calculations made with the dense media quasi-crystalline approximation (QCA) and quasi-crystalline approximation with coherent potential (QCA-CP) [81] take into account the interaction of the electromagnetic waves between correlated particles. The formulation uses bivariate particle statistics, or a pair distribution function, to provide a rigorous mathematical description of particle placement. (Some details of QCA and QCA-CP are given in section 1.1.2.) The pair distribution function expresses the non-penetrable nature of the particles and the constraints on their position in a densely packed system. The Percus Yevick approximation [60] has been used extensively in the past for both single and multi-size systems [22] to model non-penetrable particle systems. Careful experiments [39] and numerical simulations [85],[50] show that QCA and QCA-CP gives good agreement in dense media where the independent scattering approximation no longer holds true. There are other formulations of multiple scattering such as the Effective Medium Approximation [66] which was developed for the description of electronic states in amorphous metals.

1.1.1 Monte Carlo Simulations

Extensive work on scattering from a single object prompted investigation into the more complicated consideration of random distributions of scatterers. Early work by Foldy [31] introduced the concept of “configurational” averaging for random scatterers and Lax [49] generalized the idea using a quantum mechanical formulation. The formulation of multiple scattering equations for random scatterers was further advanced by work of Waterman [96, 30, 97] and Twersky [87, 88], among others. The resultant multiple scattering equations express the scattered field from an arbitrary number of particles in terms of the incident excitation by applying the extended boundary condition technique with T-matrix formalism. For spherical scatterers, it is convenient to represent the fields with spherical vector waves as basis functions [55] which can be manipulated through the aid of spherical wave transformations.

The multiple scattering equations express Maxwell's equations in a numerically exact form appropriate for computation. Monte Carlo simulations can utilize this formulation to calculate the extinction coefficients of a system of randomly distributed densely packed spheres. The formulation is numerically exact and contains no approximations, but can be computationally expensive - especially for large numbers of spheres. Chew et. al. has solved these equations for a few hundred spheres using a recursive aggregate T-matrix algorithm method (RATMA) [95]-[12]. Tsang et. al. used an iterative formulation to compute extinction rates for fractional volumes up to 25% [85]. In this dissertation we present results calculated from systems of up to 5000 spheres and fractional volumes up to 40% for both clustered and non-clustered geometries. In addition, we use the results of the simulations to determine additional characteristics of the random media such as the absorption coefficient, phase matrix and effective permittivity. Chapter 3 presents the multiple scattering equations and details of the Monte Carlo simulations.

1.1.2 QCA and QCA-CP

Throughout this thesis scattering calculations based on QCA and QCA-CP are presented. This section contains a brief overview of the pertinent equations.

The QCA expression for the average Green's function can be put into the form [81]:

$$\overline{\overline{G}}(\overline{p}) = \left\{ \overline{\overline{G}}_0^{-1}(\overline{p}) - n_0 \overline{\overline{C}}_p(\overline{p}, \overline{p}) \right\}^{-1} \quad (1.1)$$

where $\overline{\overline{G}}_0$ is the dyadic Green's operator of the background medium with propagation constant $k = \omega\sqrt{\mu\epsilon}$, and

$$\overline{\overline{C}}_j = \overline{\overline{T}}_j + n_0 \int d\overline{r}_l h(\overline{r}_l - \overline{r}_j) \overline{\overline{T}}_j \overline{\overline{G}}_0 \overline{\overline{C}}_l \quad (1.2)$$

with the operator $\overline{\overline{T}}_l$ as the single particle transition operator associated with particle l , $h(\overline{r}) = g(\overline{r}) - 1$ is the correlation function, ($g(\overline{r})$ is the pair distribution

function), and n_0 is the density of the particles. The effective propagation constant can be calculated by solving the equation :

$$\det \left[\overline{\overline{G}}_0^{-1}(\overline{p}) - n_0 \overline{\overline{C}}_p(\overline{p}, \overline{p}) \right] = 0 \quad (1.3)$$

When particle concentrations are large, the coherent wave will propagate with an effective wavenumber K , and the scattering potential will result from the difference in wavenumber from K to k . In the coherent potential (CP) approach, the idea is to introduce a Green's operator with wavenumber K instead of using the dyadic Green's operator of the background medium. In the CP formulation, the mean Green's operator can be expressed as [81]

$$E(\overline{\overline{G}}) = \overline{\overline{G}}_c = \overline{\overline{G}}_0 + n_0 \overline{\overline{G}}_0 \int \overline{\overline{r}}_j \overline{\overline{C}}_j E(\overline{\overline{G}}) \quad (1.4)$$

where $E()$ denotes the expectation operator, and with the coherent operator $\overline{\overline{C}}_j$ and the modified transition operator $\overline{\overline{t}}$ given in operator form by

$$\overline{\overline{C}}_j = \overline{\overline{t}}_l + n_0 \int d\overline{\overline{r}}_l \overline{\overline{t}}_j \overline{\overline{G}}_c h(\overline{\overline{r}}_l - \overline{\overline{r}}_j) \overline{\overline{C}}_l \quad (1.5)$$

$$\overline{\overline{t}}_j = \overline{\overline{U}}_j + \overline{\overline{U}}_j \overline{\overline{G}}_c \overline{\overline{t}}_j \quad (1.6)$$

In (1.5), $h(\overline{\overline{r}}_l - \overline{\overline{r}}_j)$ once again denotes the correlation function. The dispersion relation for QCA-CP is

$$\det \left[\overline{\overline{G}}_0^{-1}(\overline{p}) - n_0 \overline{\overline{C}}_p(\overline{p}, \overline{p}) \right] = 0 \quad (1.7)$$

Computation of the effective propagation constant using QCA-CP requires solution of (1.7), which involves solving (1.5) for $\overline{\overline{C}}_p(\overline{p}, \overline{p})$ and (1.6) for $\overline{\overline{t}}$. In the low frequency approximation, the solution for $\overline{\overline{t}}$ is [81],[23]

$$\bar{\hat{t}}_p(\bar{p}, \bar{p}) = \hat{t}_m v \bar{I} \quad (1.8)$$

where

$$\hat{t}_m = 3K \hat{y} \left[1 + i \frac{2}{3} K^3 a^3 \hat{y} \right] \quad (1.9)$$

$$\hat{y} = \frac{k_j^2 - k^2}{3K^2 + (k_j^2 - k^2)} \quad (1.10)$$

Solving (1.5) and (1.7) gives a nonlinear equation for the effective propagation constant :

$$\bar{\hat{C}}_j(\bar{p}, \bar{p}') = \hat{c} \bar{I} \quad (1.11)$$

$$\hat{c} = v_0 \hat{t}_m + f \hat{t}_m \hat{c} \left[\frac{1}{3K^2} + \frac{2}{3} i K \int_0^\infty dr r^2 [g(r) - 1] \right] \quad (1.12)$$

Using the expression for \hat{t}_m given in 1.10, an expression for \hat{c} can be computed, in which only the leading term of the real part and the leading term of the imaginary part need to be retained. This gives a nonlinear dispersion relationship of

$$K^2 = k^2 + n_0 \hat{c} \quad (1.13)$$

which can be solved iteratively.

Transport theory, also called radiative transfer (RT) theory, describes the transfer of radiant energy through a medium containing particles [8]. In transport theory it is assumed that there is no correlation between the field and that the addition of intensities is valid. For dense media the particle densities introduce correlated scattering that must be taken into account. The radiative transfer equations for dense media can be derived from analytic wave theory [86], [83] and are called radiative

wave equations to distinguish them from the classical case. The derivations are based on QCA-CP for the first moment of the field and a modified ladder approximation on the second moment of the field. The reason for choosing QCA-CP over QCA is that the former is energetically consistent with the modified ladder approximation, and the integrated optical relation is satisfied. The radiative wave equations resemble the classical transfer equations in form, but the albedo and extinction rates incorporate the effects of dense media. In [82] the low frequency solution to QCA-CP is used to calculate the extinction coefficient of spherical particles (fractional volume of 30%) and compute passive microwave signatures. The dense media radiative wave equations predict a much smaller albedo, and thus larger brightness temperature than the conventional transfer theory.

1.2 Application to Remote Sensing of Snow Covered Regions

Remote sensing is a valuable tool in obtaining information on snow covered regions. Knowledge of the depth, nature and water content of snow is important for applications of hydrology, snow mechanics, and global climate monitoring. This information is difficult to obtain by direct measurement since travel and transport of instruments to many regions of interest is laborious and costly. The use of satellite data provides measurements from many otherwise inaccessible areas, and gives repeated coverage over time. In addition, microwave sensors are not affected by cloud covers and can penetrate snow packs to recover information on the internal snow properties.

To utilize the information provided by microwave remote sensing, the electromagnetic properties of snow needs to be well understood requiring an understanding of the dielectric properties of snow and a model of the ice and air that comprise the snow. The following section provides a brief overview of some of the physical and electromagnetic properties of snow necessary for the consideration of snow as a dense media.

1.2.1 *The Snow Medium Model*

In this dissertation, only dry snow, or snow in which the liquid water content is negligible, is considered. This simplifies the description of snow to that of ice grains in an air background. Snow is a non-tenuous random medium since the relative dielectric constant of ice differs significantly from that of free space. At the microwave frequencies, the real part of the permittivity of ice is about 3.2, and the imaginary part ranges between 10^{-4} and 0.05 depending on temperature and frequency.

The appropriate electromagnetic model for snow depends on the relationship between the wavelength λ and the size of the ice grains that form the snow. For low frequencies, when the ice grains are very small relative to λ and scattering can be ignored, the snow can be regarded as a mixture whose macroscopic dielectric constant $\epsilon = \epsilon' + i\epsilon''$ can be computed through use of mixing formulae. These formulae define ϵ in terms of the permittivity of the ice particles and that of the air, and the fractional volumes (or densities) occupied by each.

Many mixing formulas have been devised, including the theory for spheres by Maxwell-Garnet [54], the extension to ellipsoids proposed by Bohren and Battan [7], and the equation of Polder and van Santen [62]. The applicability of these formulae to snow is examined in detail by Mätzler [53] who finds the accuracy of the theories depends on the nature of the snow (i.e., new snow, depth hoar, refrozen crusts, etc.) and on the ability to determine the parameters of the mixing formulae such as shape factors.

For higher frequencies, scattering from the ice grains plays an important role in the microwave characteristics of snow, and the mixing formulae may not be applicable. In this regime, the microstructure of the snow must be considered. According to [13], the grain size for snow crystals varies between 0.2 mm. (very fine) and 5 mm. (very coarse), with the average grain on the order of a millimeter. For the microwave regime, this can correspond to scatterers whose sizes range from a fraction of a wavelength

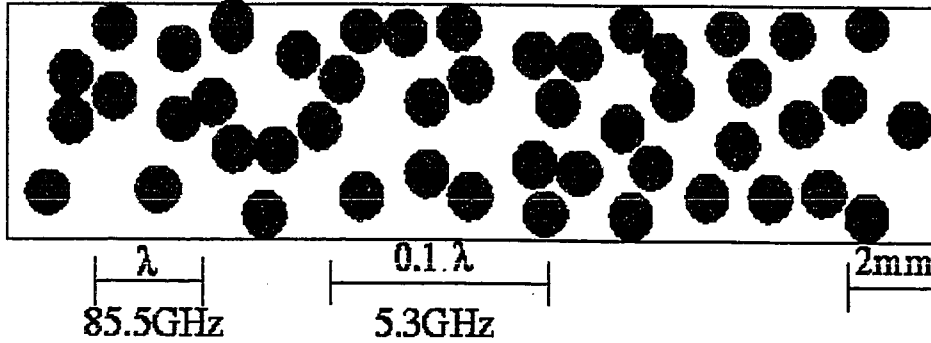


Figure 1.1: Illustration of snow grain size vs. microwave wavelength

to comparable to λ , as illustrated in figure 1.1.

Snow that has metamorphosed has very different characteristics than fresh or “new” snow. The ice crystals lose their original dendritic structure and facies, and become more rounded in shape. Deposited snow increases in density as the grains grow and form “necks” with neighboring particles. Much research has been done to understand the sintering process ([43, 37, 46, 33, 16]). The result of these destructive processes is the presence of clusters or aggregations of ice grains that can have a pronounced effect on the nature of the electromagnetic scattering.

1.3 Overview of this dissertation

Following the short introduction given in this chapter, Chapter 2 describes the sticky particle pair distribution function which can be used to model clustered spheres. A closed form solution is derived and used in QCA and QCA-CP to calculate the extinction from systems of clustered particles. The higher levels of scattering from sticky particles are used to explain experimental results of light scattering from silica particles. The chapter concludes with a comparison of scattering from sticky particles

and scattering from a size distribution of spheres.

In chapter 3 we calculate the scattering from sticky and non-sticky spheres using Monte Carlo simulations in which the spherical scatterers are deposited with an adhesive potential that results in clustering. The simulations use a numerically exact formulation of the multiple scattering equations that is solved exactly for a large number of spheres and up to 40% by volume. The convergence of the iterative solution gives physical insight into the importance of the higher orders of multiple scattering and results from higher fractional volumes are compared with QCA-CP. In addition to the scattering coefficient, the absorption coefficient is calculated from the incoherent electromagnetic field. As the fractional volume of the scatterers increases, the phenomenon of absorption enhancement occurs where the absorption coefficient is greater than that predicted by the classical assumption of independent absorption.

Chapter 4 continues to utilize Monte Carlo simulations to calculate the properties of the dense media. In addition to the extinction coefficient, the phase matrix and the effective permittivity are derived from the electromagnetic field within the test volume. These quantities are needed for the solution of the radiative transfer (RT) equation which is used to describe the transfer of radiant energy from a half-sphere of spherical scatterers. The RT equation can be applied to microwave remote sensing of snow covered terrain and the results compared with data. The level of the co-polarized and de-polarized bistatic scattering predicted by the RT equation depends strongly on the assumptions used to derive the scattering properties. The second order iterative solution of the RT equation with quantities obtained from Monte Carlo simulation can explain the level of microwave backscatter observed experimentally.

The last chapter of this dissertation is concerned with the stereological analysis of snow cross sections with the objective of recovering the pair distribution function. A log-normal distribution describes the ice grain diameters and the parameters of the distribution are obtained from section data. The sections are used to obtain an area pair distribution function (2-D) which allows for retrieval of the total volume

pair distribution function from inversion of an integral equation. The recovered pair distribution function can be decomposed into a family of functions related to particle radii by a least squares model fit. This process is controlled by a set of physically meaningful set of rules which govern the function selection. The scattering is calculated from the family of pair functions and from a hole correction approximation for the larger sizes.

Chapter 2

STICKY PARTICLES

In this chapter we consider scattering from systems of densely distributed, non-tenuous spheres that exhibit surface adhesion. These particles are not randomly organized but have a tendency to form clusters and bonds with each other. This seems appropriate for geophysical media such as snow where the ice grains form bridges as metamorphosism occurs. The clustering potential is modeled using the Percus-Yevick pair distribution formulation with spheres displaying surface adhesion. The adhesive force is parameterized in a variable τ which governs the degree of clustering. The pair distribution function has a closed form analytical solution and is used in the quasi-crystalline approximation (QCA) and the quasi-crystalline approximation with coherent potential (QCA-CP) to derive a low frequency solution to the dense media scattering problem.

Scattering calculations using QCA-CP with sticky hard spheres are compared with experimental results in section 2.3. The experiment involved light scattering from colloidal silica particles suspended in a solvent background. The comparison with theory shows that the experimental data can be explained by assuming the silica particles have some adhesion, but cannot be explained without this assumption. In essence, the clustering of the particles effectively produces larger particle sizes and increases scattering in the low frequency regime. The sticky particle pair function has been used by other researchers to explain x-ray scattering from aggregated gold colloids [21].

We investigate the concept of an equivalent particle size for the clusters in section 2.4. In this section, we show attempts to reproduce the scattering nature of the

sticky particles by larger non-sticky particles and distributions of non-sticky particle sizes. The result of these attempts is the inability to match the scattering behavior of the very sticky particles. The particle clusters are irregular in geometry and cannot be matched by larger non-sticky spheres. In view of this conclusion it seems essential to consider the organization and clustering of adhesive particles in scattering calculations.

2.1 *Pair Distribution Function of the Sticky Sphere in the PY Approximation*

We shall consider a system consisting of non-penetrable, spherical particles of diameter d with a non-zero surface adhesive force, *i.e.* sticky hard spheres (SHS). In this model, the interaction between two particles is of very short range, with the nature of surface adhesion, and it is strong enough to bind the two particles when they contact each other. The SHS model is characterized by an interparticle potential, $u(r)$, given by [4] :

$$u(r) = \begin{cases} \infty & \text{for } 0 < r < s \\ \ln \frac{12\tau(d-s)}{d} & \text{for } s < r < d \\ 0 & \text{for } r > d \end{cases} \quad (2.1)$$

provided that a limit is taken in which the range of interaction becomes infinitesimal and, simultaneously, its well depth infinite, in such a way that

$$\lim_{s \rightarrow d} (d-s)e^{-u(r)} = \frac{d}{12\tau} < \infty \quad (2.2)$$

with d and τ being held fixed. The parameter τ in (1) is dimensionless, and its inverse is a measure of the attraction or stickiness between particles. The case of $\tau^{-1} = \infty$ corresponds to infinite stickiness and $\tau^{-1} = 0$ corresponds to non-sticky particles.

The pair distribution function $g(r)$ measures the probability of finding a particle at a point r given a particle at $r=0$. The total correlation function $h(r)$ between a

pair of particles is defined as

$$h(r) = g(r) - 1 \quad (2.3)$$

The direct correlation function $c(r)$ between a pair of particles, which is short-ranged, is related to $h(r)$ by means of the Ornstein-Zernike relation [5],[6],[35]:

$$h(r) = c(r) + n \int d\bar{r}' c(r') h(|\bar{r} - \bar{r}'|) \quad (2.4)$$

where n is the number of particles per unit volume. Equation (2.4) indicates that the total influence of a particle on another particle in the presence of remaining particles can be decomposed into a sum of the direct effect and the indirect effect through other particles.

Under the Percus-Yevick (PY) approximation [35],[60], when the potential $u(r)$ vanishes, so does $c(r)$, thus :

$$c(r) = 0 \quad \text{for } r > d \quad (2.5)$$

Also, since the particles are non-penetrable, the pair distribution function $g(r)$ is zero when $r < s$. Hence, $h(r) = -1$ as $r < s$ (see equation 2.3). The behavior of function $h(r)$ is more complicated in the region $s < r < d$. It can be seen from (1) that $h(r)$ will have a delta-function singularity when $s \rightarrow d$. In this limit, we have

$$h(r) = -1 + \frac{td}{12\tau} \delta(r - d) \quad \text{for } 0 < r < d \quad (2.6)$$

where t is a dimensionless parameter to be determined later. The parameter t tends to zero in the limit $\tau^{-1} = 0$. The PY approximation of the pair distribution function $g(r)$ for the sticky spherical particles as described by (2.1) can be solved analytically using the factorization method of Baxter [5],[6].

The Ornstein-Zernike relationship (2.4) can be Fourier transformed to obtain a convenient algebraic equation:

$$1 - n\tilde{C}(p) = \{1 + n\tilde{H}(p)\}^{-1} \quad (2.7)$$

where $\tilde{H}(\bar{p})$ and $\tilde{C}(\bar{p})$ are the three dimensional Fourier transform of $h(\bar{r})$ and $c(\bar{r})$, *i.e.*,

$$\tilde{H}(\bar{p}) = \int d\bar{r} e^{i\bar{p}\cdot\bar{r}} h(\bar{r}) \quad (2.8)$$

$$\tilde{C}(\bar{p}) = \int d\bar{r} e^{i\bar{p}\cdot\bar{r}} c(\bar{r}) \quad (2.9)$$

Because of the spherical particle assumption, the transform only depends on $p = |\bar{p}|$. According to the Wiener-Hopf technique due to Baxter [5],[6], the left-hand side of (7) can be factorized into the form

$$1 - n\tilde{C}(p) = \tilde{Q}(p)\tilde{Q}(-p) \quad (2.10)$$

where $\tilde{Q}(p)$ is defined by

$$\tilde{Q}(p) = 1 - 2\pi n \int_0^d dr e^{ipr} Q(r) \quad (2.11)$$

and $Q(r)$ is a real function, $Q(r) = 0$ for $r > d$. Explicit relations between $Q(r)$ and $c(r)$ and $h(r)$ can be obtained by substituting (2.8)–(2.9) and (2.11) into (2.7) and (2.10), and taking the inverse Fourier transforms [5],[6]. It is found that

$$rc(r) = -Q'(r) + 2\pi n \int_r^d dx Q(x)Q(x-r) \quad (2.12)$$

for $0 < r < d$, and

$$rh(r) = -Q'(r) + 2\pi n \int_0^d dx (r-x)h(|r-x|)Q(x) \quad (2.13)$$

for $r > 0$, where $Q'(r)$ is the derivative of $Q(r)$. For sticky particles, equations (2.6) and (2.13), in the range $0 < r < d$, give rise to a closed-form expression for $Q(r)$:

$$Q(r) = A \frac{r^2}{2} + Br + D \quad (2.14)$$

where

$$A = \frac{1 + 2f - \mu}{(1 - f)^2} \quad (2.15)$$

$$B = \frac{(-3f + \mu)d}{2(1 - f)^2} \quad (2.16)$$

$$D = -A\frac{d^2}{2} - Bd + \frac{td^2}{12} \quad (2.17)$$

$$f = \frac{\pi}{6}nd^3 \quad (2.18)$$

$$\mu = tf(1 - f) \quad (2.19)$$

The direct correlation function $c(r)$ can be evaluated from (2.12) by using (2.14).

For a given volume fraction f and stickiness parameter τ , the parameter t is determined by the quadratic equation [4],[3]

$$\frac{f}{12}t^2 - \left(\tau + \frac{f}{1-f}\right)t + \frac{1+f/2}{(1-f)^2} = 0 \quad (2.20)$$

When τ is greater than a value

$$\tau_c = \frac{2 - \sqrt{2}}{6} \quad (2.21)$$

there are two real solutions for t throughout the permissible fractional volume range $0 < f < 1$. Below this value there exists an intermediate range of volume fractions within which there are no real solutions for t . Moreover, a further condition to determine the solution of t is that $\tilde{Q}(0)$ must be positive, or [4],[3]

$$\mu < 1 + 2f \quad (2.22)$$

The procedure for calculating the pair function is as follows. Given the particle diameter d , particle concentration f , and particle stickiness τ , the parameter t is first determined from (20)–(22). By using the parameter t and equations (14)–(19), $Q(r)$ for $0 < r < d$ can be computed. Then the Fourier transform $\tilde{Q}(p)$ is calculated by using (11), and $\tilde{C}(\bar{p})$ is evaluated by using (10). Next, $\tilde{H}(p)$ is computed by solving equation (7). Then $h(r)$ is obtained by taking an inverse Fourier transform of $\tilde{H}(p)$ according to (8). Finally, the pair distribution function $g(r)$ can be calculated from (3).

In Fig. 2.1, the pair distribution functions are shown for systems with sticky particles of identical size, $\tau=0.2$ and $\tau=0.5$, and compared with the non-sticky case for $f=0.3$. The major features for the pair distribution functions of sticky particles

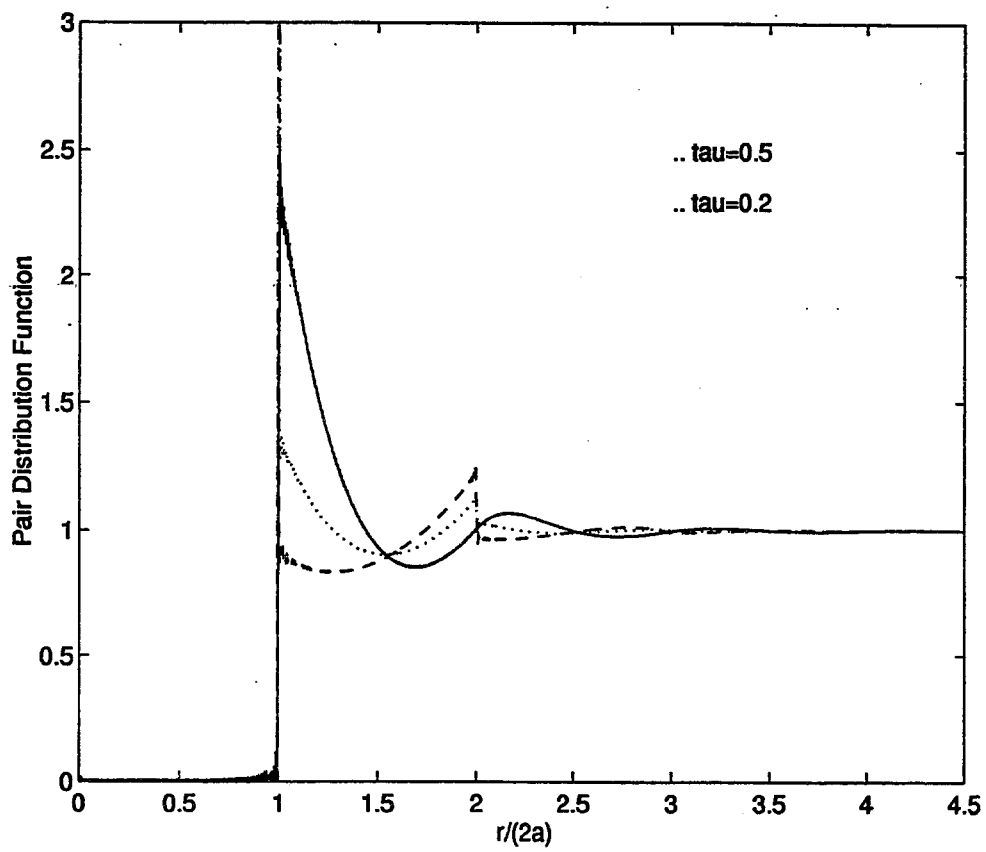


Figure 2.1: Percus Yevick Pair distribution function for sticky spheres with $\tau = 0.2$ and $\tau = 0.5$, and for non-sticky spheres and $f=0.3$.

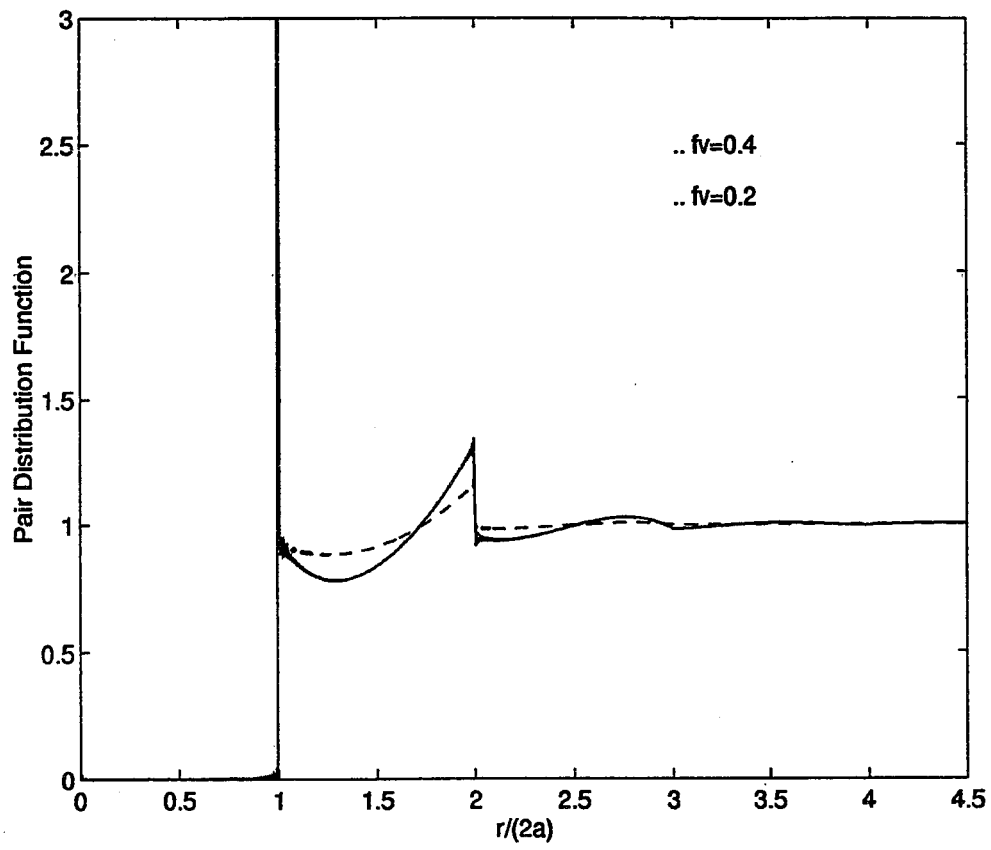


Figure 2.2: Percus Yevick Pair distribution function for sticky spheres with $f = 0.2$ and $f = 0.4$ and stickiness $\tau = 0.2$.

are the occurrence of discontinuities at the particle separation equals one and two diameters. The discontinuity at $r=d$ is because the particles can not penetrate each other. The height of the peak at $r=d$ grows rapidly with the increasing of particle stickiness while the width of this peak reduces, which shows a stronger connectedness between particles as particles getting more sticky, and other particles are more likely to be excluded from the region $d < r < 2d$. Therefore, in a dense medium with sticky particles, the sticky particles tend to aggregate together. The discontinuity at $r=2d$ arises from the fact that for $r > 2d$, the integrand in the integral of (2.13) does not include the contribution of the delta function of (2.6), while for $r < 2d$, the delta function is included. Physically, when the separation between two particles is larger than twice the diameter, the probability of these two particles bound or connect to a third particle drops to zero. In Fig. 2.2, the pair distribution functions are plotted for $f = 0.2$ and $f = 0.4$, with stickiness $\tau = 0.2$. For higher concentration of sticky particles, the pair distribution function displays more fluctuations just as the case of non-sticky particles.

2.2 QCA-CP Calculations with Sticky Particle Pair Function

A dense medium is comprised of an appreciable fraction of scatterers. It has been shown that the assumption that particles scatter independently is invalid for dense media. The quasicrystalline approximation with coherent potential (QCA-CP) takes into account the coherent scattering between particles. In this section, the dispersion relationship for QCA-CP is given, and the solution with the sticky particle pair function described in section 2.1 is illustrated.

The dispersion relationship for (QCA-CP) is [76],[81] :

$$\det \left[\overline{\overline{G}}_0^{-1}(\overline{p}) - n_0 \overline{\overline{\hat{C}}}_p(\overline{p}, \overline{p}) \right] = 0 \quad (2.23)$$

where the coherent operator $\bar{\bar{C}}_j$ and the modified transition operator $\bar{\bar{t}}$ are given in operator form by

$$\bar{\bar{C}}_j = \bar{\bar{t}}_j + n_0 \int d\bar{r}_l \bar{\bar{t}}_j \bar{\bar{G}}_c h(\bar{r}_l - \bar{r}_j) \bar{\bar{C}}_l \quad (2.24)$$

$$\bar{\bar{t}}_j = \bar{\bar{U}}_j + \bar{\bar{U}}_j \bar{\bar{G}}_c \bar{\bar{t}}_j \quad (2.25)$$

with n_0 the number density of the particles, $\bar{\bar{G}}_c$ the coherent Green's operator, and $\bar{\bar{U}}_j$ the scattering potential operator associated with the j th scatterer. In (2.24), $h(\bar{r}_l - \bar{r}_j)$ denotes the correlation function and is given by (2.3) for the Percus Yevick approximation.

Computation of the effective propagation constant using QCA-CP requires solution of (2.23), which involves solving (2.24) for $\bar{\bar{C}}_p(\bar{p}, \bar{p})$ and (2.25) for $\bar{\bar{t}}$. In the low frequency approximation, the solution for $\bar{\bar{t}}$ is [81],[23]

$$\bar{\bar{t}}_p(\bar{p}, \bar{p}) = \hat{t}_m v \bar{\bar{I}} \quad (2.26)$$

where v is the particle volume and

$$\hat{t}_m = 3K \hat{y} \left[1 + i \frac{2}{3} K^3 a^3 \hat{y} \right] \quad (2.27)$$

$$\hat{y} = \frac{k_j^2 - k^2}{3K^2 + (k_j^2 - k^2)} \quad (2.28)$$

with k_j is the wavenumber of the j th scatterer, a is the particle radius, and K is the effective wavenumber of the random media.

Solving (2.24) and (2.23) gives a nonlinear equation for the effective propagation constant :

$$\bar{\bar{C}}_j(\bar{p}, \bar{p}') = \hat{c} \bar{\bar{I}} \quad (2.29)$$

$$\hat{c} = v_0 \hat{t}_m + f \hat{t}_m \hat{c} \left[\frac{1}{3K^2} + \frac{2}{3} i K \int_0^\infty dr r^2 [g(r) - 1] \right] \quad (2.30)$$

where f is the fractional volume of the scatterers and $g(r)$ is the pair distribution function.

Using the expression for \hat{t}_m given in (2.28), an expression for \hat{c} can be computed, in which only the leading term of the real part and the leading term of the imaginary part need to be retained. This gives a nonlinear dispersion relationship of

$$K^2 = k^2 + n_0 \hat{c} \quad (2.31)$$

which can be solved iteratively.

The dispersion relationship depends on \hat{c} which depends on the integral of $[g(r) - 1]$. This can be expressed as

$$\int_{-\infty}^{\infty} d\bar{r} [g(\bar{r}) - 1] = \tilde{H}(\bar{p} = 0) \quad (2.32)$$

with \tilde{H} as given in equation 2.8. Using the relationship between $\tilde{C}(\bar{p})$ and $\tilde{H}(\bar{p})$ given in (2.7), equations (2.14)-(2.19) can be used with (2.12) and (2.9) to give an expression for the integrand when the particles have surface adhesion.

2.3 Comparison with Results from Turbidity Studies

The concept of sticky particles has been explored by Penders and Vrij [58] in a interpretation of turbidity studies on colloidal silica particles. In these experiments, results from light scattering off of high concentrations of silica particles is explained with the sticky particle pair function described in section 2.1. Jansen et. al. [41] performed the experiment using three samples of stearylsilica particles with different polydisperse radii. Penders and Vrij compared the measured turbidity (attenuation of a light beam by scattering when passing through a sample) to results obtained by calculation.

2.3.1 Description of the Turbidity Study

Details of the experimental procedure are given in [41]. The synthesis entailed measurement of turbidity from three different silica particles at varying volume concentrations. Penders and Vrij [58] interpreted the turbidity data using theory based on the adhesive hard spheres model outlined in section 2.1. Turbidity (τ_s) is defined by the Lambert-Beer relation :

$$\tau_s = l^{-1} \ln(I_0/I_t) \quad (2.33)$$

where I_0 is the incident intensity, I_t is the transmitted intensity, and l is the light path in the samples. For a monodispersive case where the reduction of transmitted intensity is caused solely by scattering the following conservation law relates turbidity and scattering :

$$\tau_s = 2\pi \int_0^\pi R(K) \sin(\theta) d\theta \quad (2.34)$$

where

$$K = (4\pi n/\lambda_0) \sin(\theta/2) \quad (2.35)$$

and $R(K)$ is the Rayleigh ratio for unpolarized light, K is the scattering wave vector, θ is the scattering angle, n is the refractive index of the sample, and λ_0 is the free space wavelength. From the Rayleigh-Gans-Debye (RGD) theory of light scattering for unpolarized light :

$$R(K) = K^* c M P(K) S(K) (1 + \cos(\theta)^2) \quad (2.36)$$

where

$$K^* = 2\pi^2 n^2 (dn/dc)^2 / N_a \lambda_0^4 \quad (2.37)$$

and N_a is Avogadro's number, c is the weight concentration, and M is the molar mass of the particles. The form factor $P(K)$ accounts for the interference of light scattered from different parts within one particle. For not too large particles (radius $< 50\text{nm}$ for visible light) the form factor can be expressed as :

$$P(K) = 1 - K^2 R_g^2 / 3 \quad (2.38)$$

where R_g is the optical radius of the particles.

The structure factor $S(K)$ accounts for the interference of light scattered from different particles. It is given by :

$$S(K) = 1 + 4\pi\rho \int_0^\infty [g(r) - 1] \frac{\sin(Kr)}{Kr} r^2 dr \quad (2.39)$$

where ρ is the number density, r is the distance between two sphere centers, and $g(r)$ is the radial distribution function defined by equation (2.3). Thus the structure factor includes the interaction between colloidal stearylsilica particles in the form of a hard-sphere potential with surface adhesion.

Equation 2.39 can be expanded in terms of K^2 , and terms linear to particle concentration retained. Substituting this result into equation 2.34 and carrying out the integration gives :

$$\tau_s = HcM \left[1 - \frac{8}{3} \left(\frac{\pi n R_g}{\lambda_0} \right)^2 \right] \quad (2.40)$$

$$\times \left\{ 1 - \phi \left[8 - \frac{2}{\tau} - \frac{8}{5} \left(4 - \frac{5}{3\tau} \right) \left(\frac{\pi n d}{\lambda_0} \right)^2 \right] \right\} \quad (2.41)$$

Penders and Vrij approximated this equation to obtain an equation useful for a first measure of τ (stickiness) in their analysis. This equation for τ_s was used to fit turbidity data from experiment :

$$\tau_s = HcM \left[1 - \frac{8}{3} \left(\frac{\pi n R_g}{\lambda_0} \right)^2 \right] \quad (2.42)$$

$$\times \exp \left\{ -\phi \left[8 - \frac{2}{\tau} - \frac{8}{5} \left(4 - \frac{5}{3\tau} \right) \left(\frac{\pi n d}{\lambda_0} \right)^2 \right] \right\} \quad (2.43)$$

From the above equation, it follows that the slope of $\ln(\tau_s/c)$ vs ϕ gives the stickiness parameter τ . Using this value and the assumption that the particles were polydisperse hard spheres with mutual attraction, particle radii matching measured values were obtained. In contrast, if the stearylsilica systems were modeled without interparticle attractions, unrealistic radii for the particles resulted.

2.3.2 QCA-CP with the Adhesive Particles applied to the Turbidity Study

The three stearylsilica particle dispersions used by Jansen et. al. in his turbidity study were modeled using the QCA-CP multiple scattering theory with adhesive hard spheres (see Section 2.2). The parameters are given in Table 2.1, where the values for τ are those for best agreement with QCA-CP. The He-Ne laser had a free space wavelength λ_0 of 632 nm, and the fractional volume of the silica scatterers was varied from 0-40 %.

Figure 2.3 shows the turbidity as a function of fractional volume for the three particle species, with the stickiness given by the values of τ in table 2.1. As expected, the scattering increases as the particle radius increases. It reaches a maximum around 15 % fractional volume. This agrees qualitatively with the simulations of Penders and Vrij, although for the larger size particles they predict greater scattering as a function of τ than that obtained using QCA-CP. This might be due to their use of the Rayleigh-Gans-Debye (RGD) approximation. Under the RGD (also

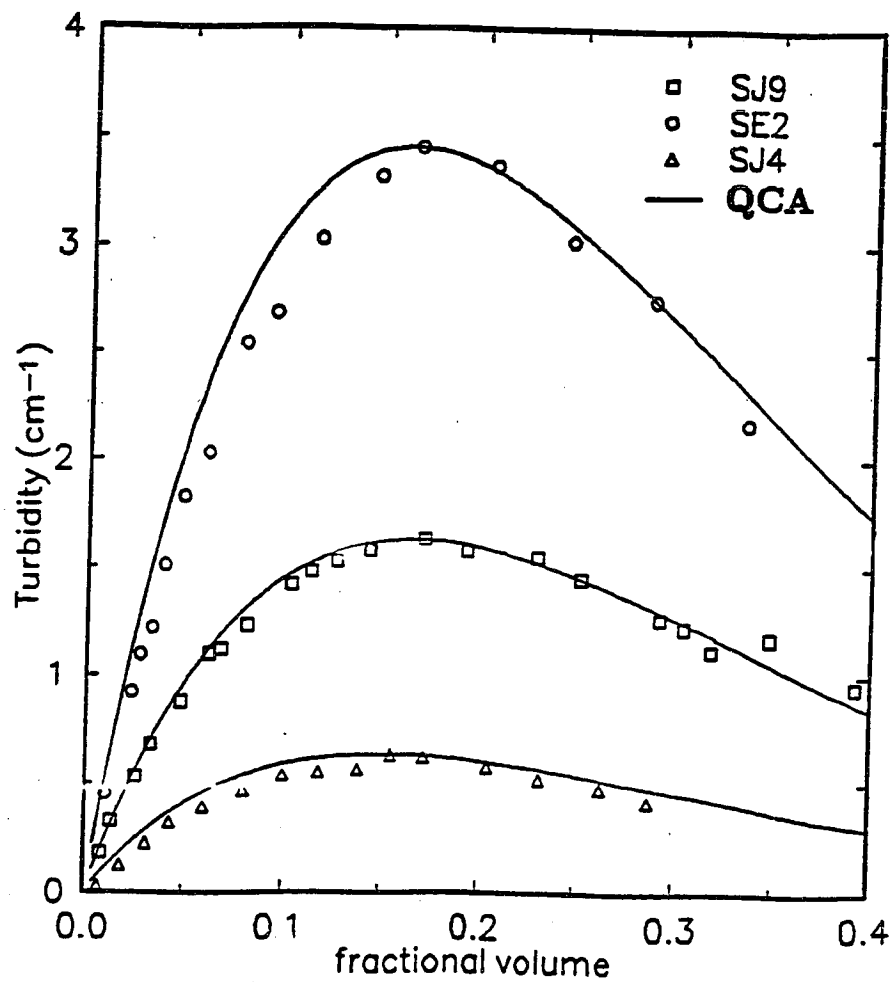


Figure 2.3: Turbidity vs. Fractional Volume calculated with parameters in Table using QCA-CP-SHS

Table 2.1: Parameter Values

QCA-CP-SHS Calculation Parameters			
Particles	SE2	SJ9	SJ4
η	1.437	1.433	1.425
ϵ_r	2.065	2.053	2.031
Radius (nm)	37.2	30.9	18.4
ka	0.711	0.563	0.386
τ	1.0	0.9	1.5
Solvent	toluene	toluene	benzene
η_s	1.49	1.49	1.494
ϵ_s	2.220	2.220	2.320

called the Born approximation) the internal field is approximated by the incident field. The validity of the approximation depends on the diameter of the scatterer, incident wavelength, and the dielectric constant of the material. However, if there is a tendency of the particles to form large, connected and complex chains, it is not clear if this approximation will hold.

Penders and Vrij estimated the stickiness for the SE2 particle to be $\tau = 2.5$. The amount of turbidity seen from sticky particles such as these is more than would be seen from the same particles with no intermolecular attraction. Figure 2.4 illustrates this point. It shows six turbidity curves calculated using QCA-CP for non-sticky hard spheres (QCA-CP-HS) over a range of radius from 20 nm. to 45 nm. Also shown is the curve using a sticky sphere model (QCA-CP-SHS) for a particle of radius of 37 nm and $\tau = 2.5$. It can be seen that the sticky sphere model predicts larger attenuation for all fractional volumes than the non-sticky model. In fact, the amount of turbidity is closer to a non-sticky particle of 40 nm. at the lower concentrations, and one of radius 42 nm. at the higher.

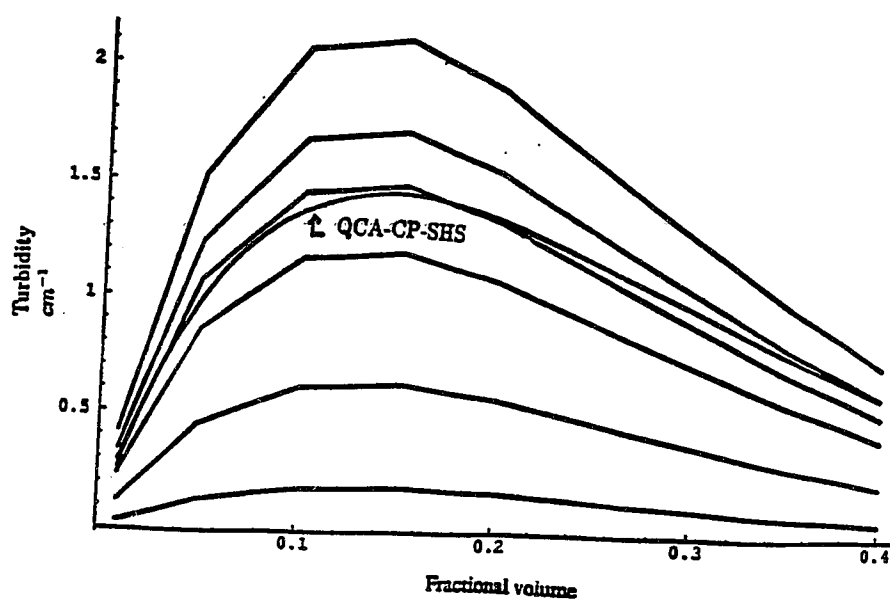


Figure 2.4: QCA-CP curves of Turbidity vs. Fractional Volume for non-sticky SE2 particles of radii 20, 30, 37.2, 40, 42, and 45 nm.(bottom to top curves), and a sticky SE2 particle of radius 37.2 nm.(shown by arrow)

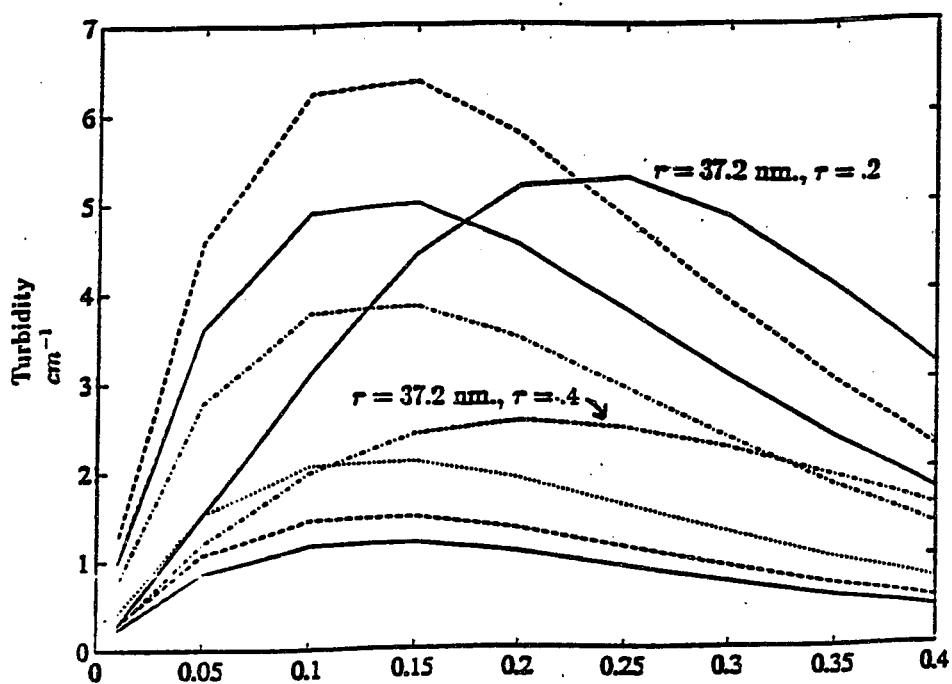


Figure 2.5: QCA-CP curves of Turbidity vs. Fractional Volume for non-sticky SE2 particles of radii between 37.2 and 65 nm., and sticky SE2 particles of radius 37.2 nm. with $\tau = 0.2$ and $\tau = 0.4$

A value of $\tau = 2.5$ does not represent a very sticky particle. Decreasing the value of τ (which *increases* stickiness), increases the amount of scattering. Simplistically, this can be viewed as increasing the particle size (i.e., a cluster of particles is larger than a single particle), which gives greater scattering - as was seen in figure 2.3. In figure 2.5 curves for non-sticky (QCA-CP-HS) particles with radii between 37.2 nm. and 65 nm. are shown along with curves (QCA-CP-SHS) for an adhesive 37 nm. particle with $\tau = 0.4$ and $\tau = 0.2$. The turbidity for these strongly attractive particles are noticeably much larger. In addition, the fractional volume at which the turbidity curve peaks has shifted to about 20 % for the less sticky case ($\tau = 0.4$), and to 25 % for the more sticky case ($\tau = 0.2$). For example, note that the maximum turbidity value of 5cm^{-1} occurs at 15% fractional volume for the non-sticky particle with a radius of 60 nm. In contrast, a very sticky ($\tau = 0.2$) particle with only a third of the volume (radius of 37.2 nm.) has a comparable turbidity of 5.3cm^{-1} attained at 25% fractional volume. The shift in the peak location is indicative of scattering by the effectively larger particle formed by the clustering, which has moved into the Mie scattering regime (see for example, [23]).

2.4 Equivalent Size Distributions

As observed in the last section, the shift to the Mie scattering is indicative of a larger particle size. In this section we investigate the possibility of producing the scattering curve of clusters of sticky particles by appropriate concentrations of particles of larger sizes that are not sticky. From figure 2.5 it is apparent that simply using one species of a larger particle is not sufficient, and that particles of more than one size are necessary.

To investigate this premise, curves of attenuation ($2\text{Im}ag(K)$) vs. fractional volume were generated for a sticky particle of radius 37.2 nm. with adhesion coefficients of $\tau = 0.2$ (very sticky) and $\tau = 0.4$ (moderately sticky). These curves were compared

with the attenuation rate for a gamma distribution of particle sizes. The attenuation for the multi-species cases was calculated using QCA-CP-SHS. For an aggregation of particles of L different sizes but the same permittivity, the dispersion relationship (2.31) can be written [23]:

$$\begin{aligned}
K^2 &= k^2 + \sum_{s_j=1}^L n_{s_j} \hat{c}_{s_j} \\
&= k^2 + \frac{3K^2}{\hat{D}} \sum_{s_j=1}^L f_{s_l} \hat{y} \times \left\{ 1 + i \frac{2K^3}{3\hat{D}} \left[a_{s_l}^3 \hat{y} + \sum_{s_j=1}^L a_{s_l}^3 8\pi^3 n_{s_j} \hat{y} H_{s_j s_l}(\bar{p}=0) \right] \right\} \\
\hat{D} &= 1 - \sum_{s_j=1}^L f_{s_l} \hat{y}
\end{aligned} \tag{2.44}$$

in which the different species are denoted by $s_j = 1, 2, \dots, L$. The radius, number density, and fractional volume of the s_j th species is a_{s_j} , n_{s_j} , and f_{s_j} respectively. Also, $H_{s_j s_l}$ is related to the Fourier transform of the correlation function between two spheres of species s_j, s_l :

$$\begin{aligned}
H_{s_j s_l}(\bar{p}) &= \frac{\tilde{H}_{s_i s_j}(-\bar{p})}{(2\pi)^3 (n_{s_i} n_{s_j})^{1/2}} \\
\tilde{H}_{s_i s_j} &= (n_{s_i} n_{s_j})^{1/2} \int d\bar{r} e^{i\bar{p} \cdot \bar{r}} h_{s_i s_j}(\bar{r})
\end{aligned} \tag{2.45}$$

A gamma distribution has the form [57]:

$$f(x) = Ax^b e^{-cx} U(x) \tag{2.46}$$

where A is such that

$$\int_0^\infty Ax^b e^{-cx} dx = 1 \tag{2.47}$$

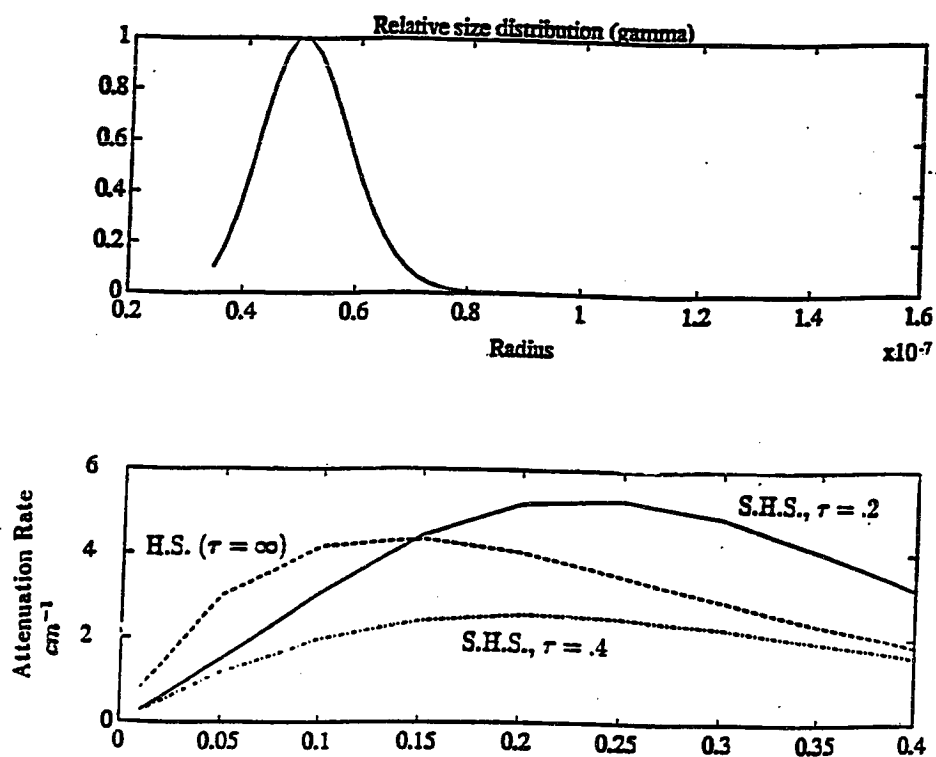


Figure 2.6: a) Gamma distribution with $b=30$ and $c=0.6$ b) Attenuation from : the gamma distribution (dashed), sticky $\tau = 0.2$ particles with radius 37.2 nm. (solid), and sticky $\tau = 0.4$ particles with radius 37.2 nm (dot-dash)

where b and c are positive. Using the gamma distribution to determine the range of particle radius' and the fractional volume of each size particle, (2.44) can be used to calculate the attenuation. Several such cases were examined.

Figure 2.6.a shows the size distribution for $b = 30$ and $c = 0.6$, which is centered around 56 nm. (with volume approximately twice that of the 37.2 nm. particle). The attenuation from this distribution is shown in 2.6.b as a dashed line. The solid line in the figure is for a 37.2 nm. particle with $\tau = 0.2$, and the dot-dashed line is for $\tau = 0.4$. As in the previous case, the position of the maximum do not agree between the sticky and non-sticky cases, even though the value of the attenuation at the maximum are comparable. One possible explanation is that the clusters of particles can form a very small number of extremely large particles. These would serve to skew the scattering statistics disproportionately.

To test this, bi-modal distributions were generated by adding two separate gamma distributions centered around different particle sizes. The first distribution centered around 37.2 nm. contained the majority of the particles, while the second distribution around 70 nm. had a much smaller number. The resulting disposition is shown in figure 2.7.a when 1% of the particles are larger, and in figure 2.8.a when 5% are. The amount of attenuation is very sensitive to these larger particles. In figure 2.7.b the dashed line representing the multi-size aggregation is very close to that of the dot-dashed line denoting the moderately sticky particles. The greatest lack of agreement is in the lower fractional volumes where the non-sticky particle curve attains its maximum earlier than the sticky. In figure 2.8.b the attenuation has risen greatly as a result of an additional 4% of the particles of a larger size. The lack of agreement between the multi-size aggregate and the very sticky particle is much more evident than it was for the moderately sticky case. In fact, there is agreement only in a very limited range of fractional volumes (25-30%).

Various distributions of particles over a range of sizes have been attempted in order to match the behavior demonstrated by the sticky particles. It appears to be

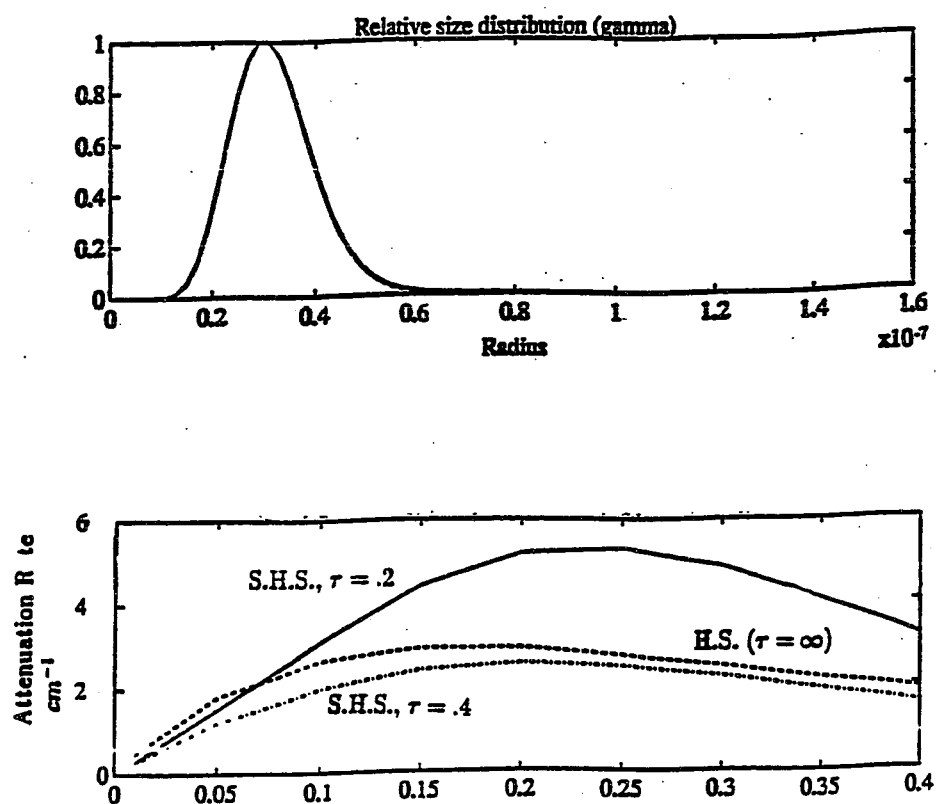


Figure 2.7: a) Bi-modal gamma distribution with 99% $b=15$, $c=0.5$ and 1% $b=40$, $c=0.6$ b) Attenuation from : the gamma distribution (dashed), sticky $\tau = 0.2$ particles with radius 37.2 nm. (solid), and sticky $\tau = 0.4$ particles with radius 37.2 nm (dot-dash)

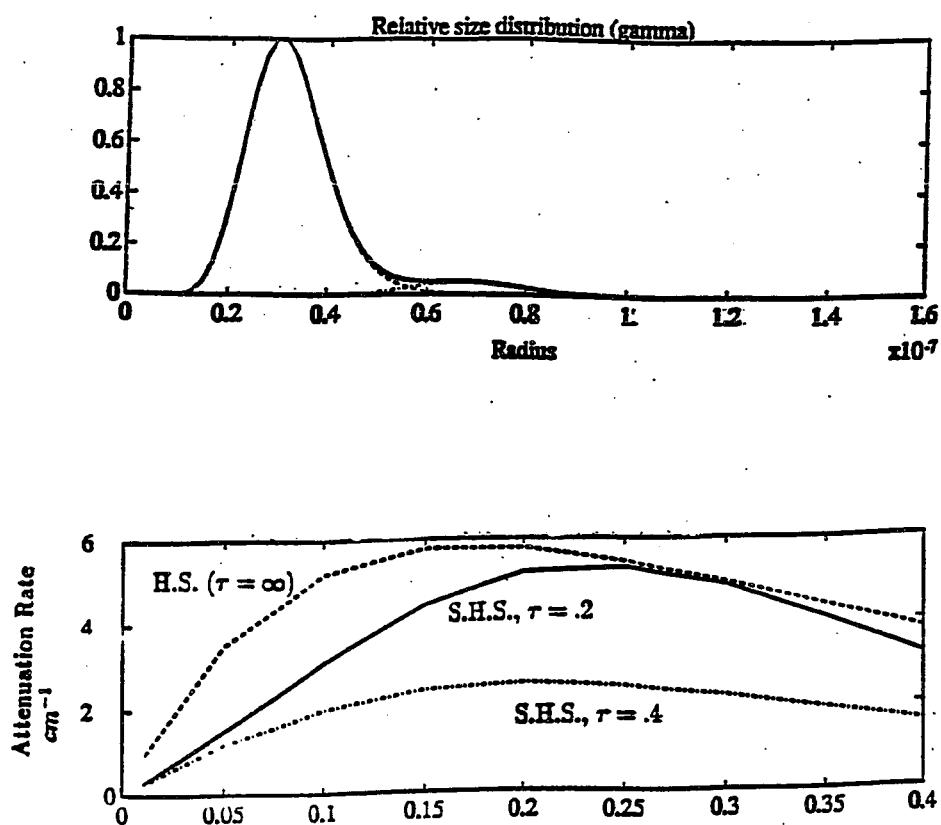


Figure 2.8: a) Bi-modal gamma distribution with 95% $b=15$, $c=0.5$ and 5% $b=40$, $c=0.6$ b) Attenuation from : the gamma distribution (dashed), sticky $\tau = 0.2$ particles with radius 37.2 nm. (solid), and sticky $\tau = 0.4$ particles with radius 37.2 nm (dot-dash)

increasing difficult to attain agreement as the particles become stickier. A reason for this can be found in consideration of the cluster shape. As the particles bind, they form complex geometrical shapes that are not spherical in nature, even though the constituent particles are spheres. Thus, it is difficult to simulate the scattering behavior of these clusters with equivalent spheres. If a medium is composed of spherical entities that have a predefined tendency to cluster, the use of a pair function to describe this geometry is necessary to attain the correct scattering physics.

2.5 Conclusion

In this chapter we have shown that it is possible to describe adhesive particles statistically with the Percus-Yevick sticky particle pair distribution function. It is also possible to use this pair function in dense media scattering theory when the medium in consideration contains particles with a tendency to cluster. The experimental data we considered from one such medium could only be explained by considering this stickiness.

The effect on the scattering behavior when the particles bond has been investigated. The primary effect is the increased attenuation due to the large cluster size, which show characteristics of scattering from a larger particle. However, when we attempted to reproduce the scattering using only non-sticky particles, we were unable to do so. We offer the explanation that the cluster geometry is so irregular, that it can not be approximated by equivalent spheres. If this is true, it implies that the inclusion of the clustering potential is necessary to accurately determine the scattering nature of bonded particle systems.

Further investigation into the nature of the particle clusters is necessary to fully understand their effect on scattering physics. Also, if the clustered particle model is to be used to model a geophysical medium - such as snow - there needs to be a method to test the applicability of the pair function and to determine the stickiness

parameter τ .

Chapter 3

MONTE CARLO SIMULATIONS FOR STICKY AND NON-STICKY SPHERES

Because of the advent of modern computers and efficient computational methods, Monte Carlo simulations by direct solution of Maxwell's equations are receiving necessary attention. In Monte Carlo simulations, aggregations of densely distributed spheres are randomly placed within N_r test volumes in a manner corresponding to a specified pair distribution function $g(r)$. The scattered fields are calculated using a numerically exact formulation of Maxwell's scattering equations and averaged over the N_r realizations. The numerical procedure is based on the multiple scattering equations of Foldy-Lax and using vector spherical waves as a basis [85]-[50]. The results include coherent wave interaction among the spheres and the averaged field can be decomposed into a coherent and incoherent part, where the extinction rate arises from the incoherent scattered field. The extinction rates calculated for fractional volumes up to 25% [85] are in excellent agreement with QCA-CP and carefully controlled laboratory experiments of dense media [52] but differ significantly from those obtained under the independent scattering assumption.

The number of spheres N that can be considered in these Monte Carlo simulations depends only on the available computer memory. For the iterative formulation there is an $O(N^2)$ memory dependence. Thus the Monte Carlo simulations provide a method of exact calculation of wave properties for large numbers of spheres. In this dissertation we present results calculated from systems of up to 5000 spheres and fractional volumes up to 40%, for both clustered and non-clustered geometries.

An exact formulation of Maxwell's equations in multiple scattering form has been solved iteratively by Tsang et al. [85] and used in Monte Carlo simulations to compute extinction rates for fractional volumes up to 25%. This formulation is a rigorous, numerically exact treatment of multiple scattering of electromagnetic waves in a system of densely packed spheres, and it agrees with results from carefully controlled laboratory experiments of dense media [52].

In the previous chapter we presented analytically derived scattering results that indicated the microstructure of a system of densely packed particles strongly effects the strength and nature of the scattering. In this chapter we calculate the scattering and absorption coefficients using Monte Carlo simulations in which the particles up to 40% fractional volume are modeled both with and without a surface adhesion. The extinction rates agree well with analytic dense medium theory. Results also show that the system absorption is different from that predicted using an independent absorption assumption due to local fields experienced by the particles. Scattering is increased when the spheres are deposited with surface adhesion that causes them to cluster and to form effectively larger particles.

3.1 *Sticky-Particle Placement*

To perform Monte Carlo simulations of systems of clustered particles described by the SHS pair distribution function $g(r)$, deposition of the particles must be influenced by the attractive square-well potential. Algorithms for shuffling until the spheres achieve a distribution given by $g(r)$ appear in Seaton and Glandt [67] and Kranendonk and Frenkel [45]. However, because the amount of shuffling required to achieve random placement of the particles while still satisfying the SHS model is very high, we have adapted the algorithms so that the particles can be directly deposited into the test volume with the SHS potential. The deposition algorithm can be stated as follows :

1. Calculate an effective subvolume for each particle energy state (PES) for the particle to be deposited;
2. Determine a position for the particle that satisfies the PES;
3. Accept or reject the position based on particle overlap;
4. Register the new bond configuration of the system.

In molecular systems, the PES of a particle corresponds to its coordination number (or number of bonds with other particles). In three-dimensional systems, the highest PES attainable is 12, which corresponds to the closest packing of neighbors. Following Seaton and Glandt [67], we have allowed moves up to PES 3, which has been shown to be a good approximation. The calculation of subvolumes for the PESs involves integrating over the sites available for each PES, neglecting overlap. For example, the subvolume associated with zero bonds (PES 0) is just the test volume. To calculate the subvolume available for one bond, we begin by considering each sphere already deposited in the test volume. Since a single bond can occur by placing the test particle anywhere along the surface of these spheres, the available subvolume is found by integrating over the surface of the spheres. Likewise, the subvolume for two bonds (PES 2) is found by integrating along the circle that lies a distance d from two other sphere centers. The calculation of the subvolumes involves registering the new particle configuration in the test volume after each deposition. The normalized subvolumes for the three PESs can be expressed as [67, 45]:

$$V^0 = V \tag{3.1}$$

$$V^1 = N \frac{4\pi d^3}{12\tau} \tag{3.2}$$

$$V^2 = \sum_{i,j} \frac{\pi d^2}{72\tau^2} r_{cir}, r_{ij} < 2d, \tag{3.3}$$

where V is the test volume, N is the number of particles, r_{ij} is the distance between the i th and j th particle, and r_{cir} is the radius of the circle such that

$$r_{\text{cir}} = d \left(1 - \left(\frac{r_{ij}}{2d} \right)^2 \right)^{1/2}. \quad (3.4)$$

The calculation of PESs requires ongoing maintenance of a catalog of the system configuration so that the number of deposited particles N , and the number of particle pairs able to bond with a third (the summation in 3.3), is known. This catalog also contains information on the positions available in each PES. Once a PES is calculated, a position in which that PES is achieved is randomly chosen from the available sites, and the check for particle overlap is done. As expected, the number of particle collisions increases as more particles are deposited in the test volume. For higher fractional volumes (i.e., $> 35\%$) deposition becomes impractical, and a shuffling algorithm is necessary instead.

The pair distribution function $g(r)$ from systems of $N = 2000$ particles, and averaged over 30 realizations is shown in Fig. 3.1. Fractional volumes of $f_v = 0.1$ and $f_v = 0.2$, with a stickiness of $\tau = 0.2$, are shown. The vertical axis represents the normalized probability, and the horizontal axis is the particle separation normalized to the particle diameter. Also shown in the figure as a solid line is the Percus-Yevick SHS calculated as in [25], which agrees with the simulation results (agreement improves as N and number of realizations N_r increase). For separations $r/d < 1.0$, $g(r)$ is zero, since there is zero probability that impenetrable particles can be separated by a distance of less than their diameter. Notice the discontinuity at $r/d = 2.0$, which corresponds to the inequality in equation 3.3. Physically, this represents the geometrical effect that two particles separated by a distance greater than their diameter cannot both bond with a third particle. The presence of this discontinuity is unique to the SHS pair distribution function and is representative of the clustering of the system.

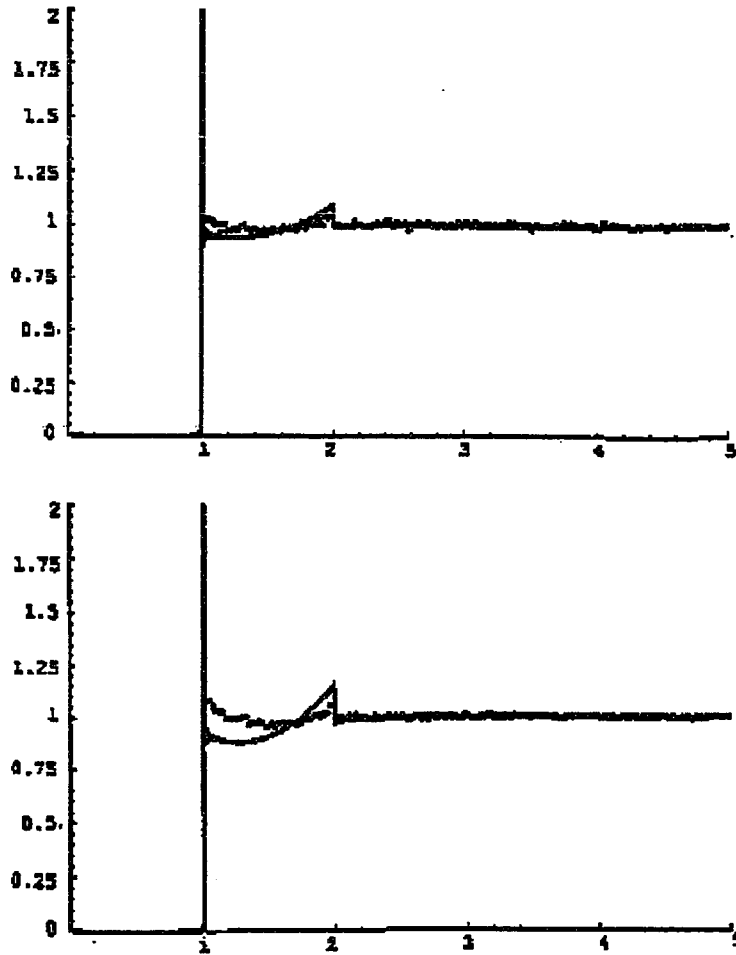


Figure 3.1: The pair distribution function calculated from Monte Carlo simulations and Percus-Yevick SHS with $\tau = 0.2$. Top plot is with $f_v = 0.1$ and bottom plot is with $f_v = .2$. The x-axis is $r/(2a)$ and the y-axis is normalized probability.

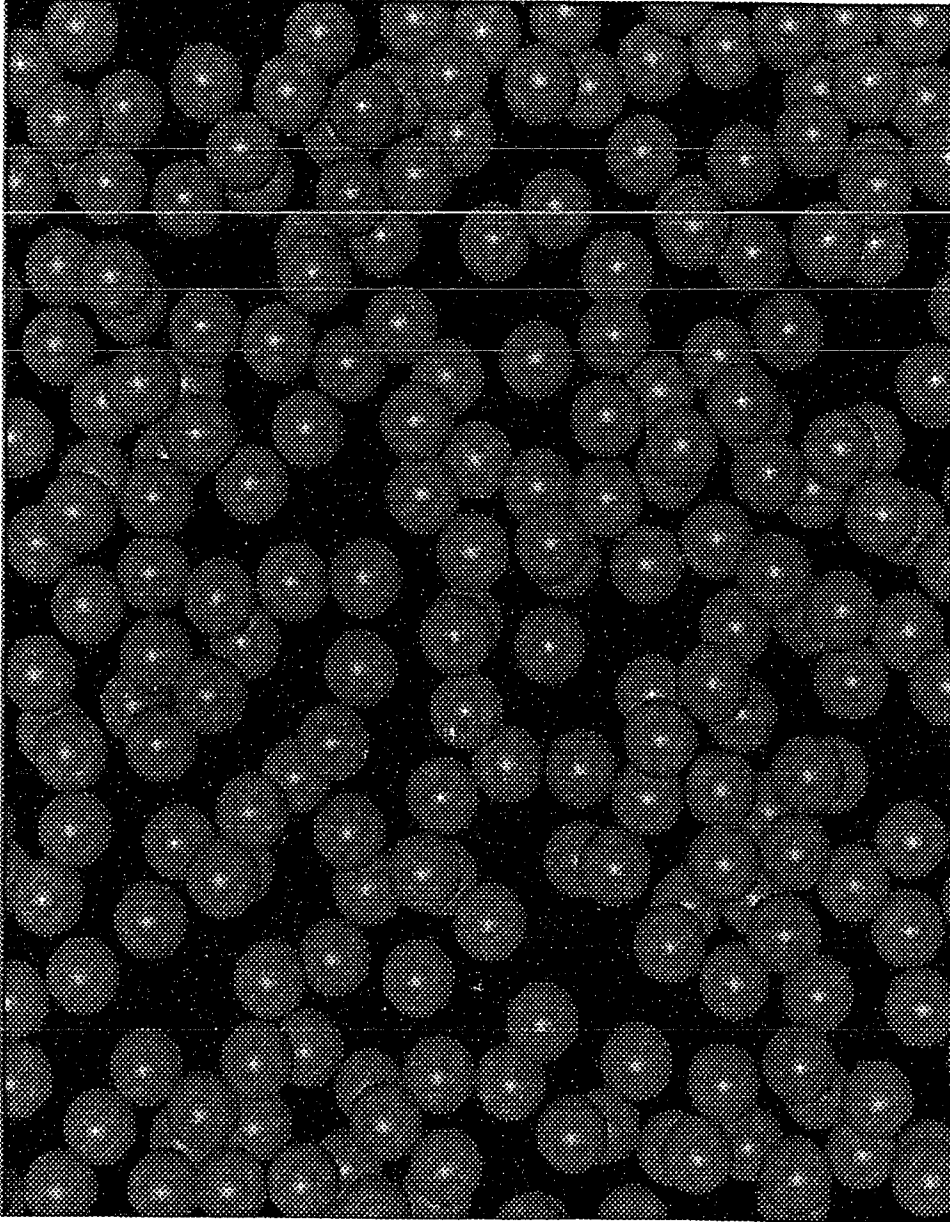


Figure 3.2: Three-dimensional computer generated view of aggregation of spheres with $f_v = 0.35$ and $\tau = 0.2$.

A computer generated view of a subvolume of sticky-particles with $\tau = 0.2$ and $f_v = 0.35$ is shown in Fig. 3.2. Among the more striking features of the clusters are their irregular and chainlike structures. In citekn:sticl, we demonstrated the inability to model the scattering behavior of these clusters with spheres of a single effective size. A description of the clusters resulting from SHS deposit can be obtained by considering the fractal nature of the resulting particle groups. For a given cluster of particles we can define the radius of gyration R_g [94] as

$$R_g = \sqrt{\frac{1}{N_c} \sum_{i=1}^{N_c} r_i^2}, \quad (3.5)$$

where N_c is the number of particles in a cluster and r_i is the distance of the i th cluster particle from the center of mass. Then there exists a logarithmic relationship between R_g and N_c , or

$$N_c = c(R_g/a)^{D_f}, \quad (3.6)$$

where c is a constant and D_f is the fractal or Hausdorff dimension [51] of the system. The fractal nature of the sticky-particle clusters provides another quantitative method in which to characterize the random media. Investigations have been made on scattering from a single fractal cluster [10, 69], and have shown that there is an increase in the scattering and absorption cross section due to the high local fields. In this chapter we investigate whether or not this local enhancement alters the overall scattering properties when a large number of randomly placed sticky-particle clusters are considered.

3.1.1 Placement for Higher Fractional Volumes

For fractional volumes over 35%, it is impossible to create an aggregation of spheres with the deposition method. This is because the loss of freedom due to the higher

sphere packing increases the chances of sphere collision during deposit. For high fractional volumes, it is necessary to instead deposit the spheres in a uniform lattice into the test volume, and then shuffle them in some fashion until a random ensemble results.

For the non-sticky spheres, shuffling occurs over N_p passes in which an attempt is made to move each sphere from its initial location to a new random location. For each sphere α , the new location r'_α is determined from its initial location r_α by

$$x'_\alpha = x_\alpha + \delta_x \quad (3.7)$$

$$y'_\alpha = y_\alpha + \delta_y \quad (3.8)$$

$$z'_\alpha = z_\alpha + \delta_z, \quad (3.9)$$

where δ_x , δ_y , and δ_z are random numbers with a magnitude between zero and some chosen ϵ . If the position at r'_α results in sphere overlap, the sphere is left in its initial position and movement is attempted with the next sphere. The randomness of the final configuration depends on the number of shuffling passes N_p and on the movement distance ϵ . If ϵ is too large, new positions will frequently collide with other spheres and few successful moves will result. On the other hand, a very small ϵ will cause such small shifts in the sphere position that the final position will not be substantially different from the original. The optimal value of ϵ depends on the sphere packing and can be determined by trial and error. We have found that the pair distribution function of an insufficiently shuffled organization of spheres is indistinguishable from an adequately shuffled organization, and thus is not an ideal indicator of randomness. Instead, the univariate particle statistics (i.e., the probability of finding a particle in a given location) can be used. For a truly random organization, the particle position should be uniformly distributed.

Once a random organization has been achieved, subsequent realizations are constructed by shuffling with $N_p = 200$ and $\epsilon = 0.1\Delta$, where Δ is the original lattice

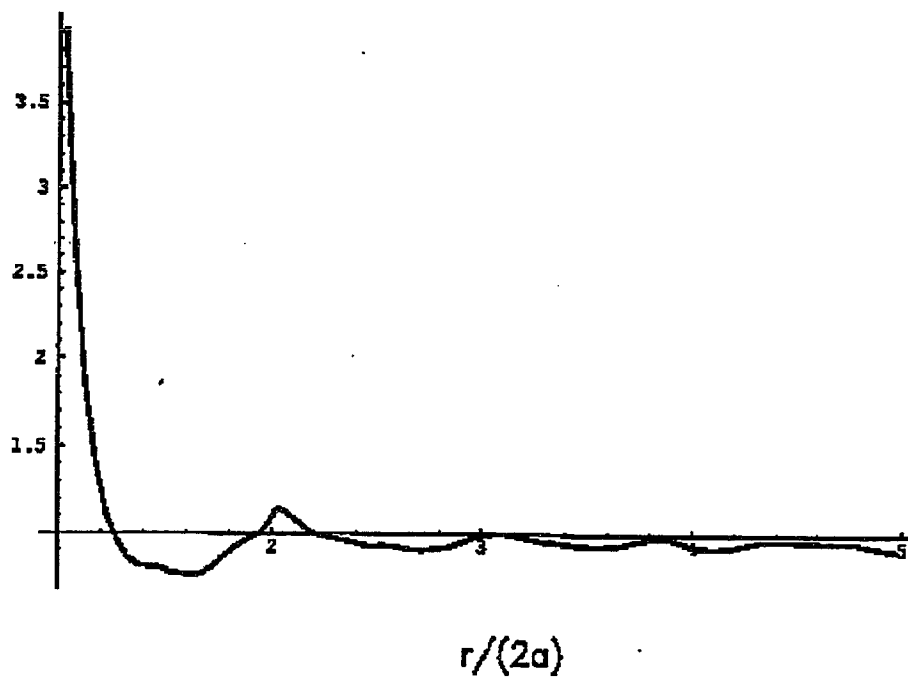


Figure 3.3: The pair distribution function calculated from Monte Carlo simulations with a shuffling algorithm for a fractional volume of 40%. The y-axis is normalized probability.

spacing. Figure 3.3 shows the pair distribution function for 3500 spheres and a fractional volume of 40%, averaged over 15 realizations. The form of $g(r)$ in Fig. 3.3 agrees well with the Percus-Yevick hard sphere pair distribution function.

3.2 Solution of Multiple Scattering Equations

To calculate the extinction and absorption coefficients of a system of densely packed spheres, we iteratively solve Maxwell's equations that are cast in multiple scattering form. The formulation is numerically exact and contains no approximations. For each realization of N spheres, the positions are generated randomly in the manner described in section 3.1. We then solve the multiple scattering equations exactly.

Maxwell's equations cast into the Foldy-Lax multiple scattering equations can be expressed in matrix notation as [81]

$$\begin{aligned} \bar{a}^{s(\alpha)} = & \sum_{\substack{\beta=1 \\ \beta \neq \alpha}}^N \bar{T}^{\alpha} \bar{\sigma}(k \bar{r}_{\alpha} \bar{r}_{\beta}) \bar{a}^{s(\beta)} + \exp(i \bar{k}_i \cdot \bar{r}_{\alpha}) \bar{T}^{\alpha} \bar{a}_{inc}, \end{aligned} \quad (3.10)$$

where :

- $\bar{a}^{s(\alpha)}$ is the vector of coefficients for spherical wave harmonics of the multiple scattered field for particle α
- \bar{a}_{inc} is the coefficient of the incident wave
- k is the wavenumber of the background media
- \bar{k}_i is the wavenumber of the incident wave
- N is the number of spheres in the containing volume

- $\bar{\sigma}(k\bar{r}_\alpha\bar{r}_\beta)$ is the vector spherical wave transformation matrix
- \bar{T}^α is the T matrix for scatterer α which depends on the permittivity and radius of α , as well as the background permittivity
- \bar{r}_α and \bar{r}_β are the centers of particles α and β , respectively.

Equation 3.10 can be interpreted physically as follows. The final scattered field coefficients for a particle α depend on the excitation experienced by that particle. This excitation is due to both the original incident field \bar{a}_{inc} as well as the radiated field from surrounding particles $\bar{a}^{(\beta)}$. The scattered field from other particles can be translated from those particles to particle α using Huygen's equivalency principle through use of the vector spherical wave transformation matrix $\bar{\sigma}(k\bar{r}_\alpha\bar{r}_\beta)$. Finally, the response of α to the excitation it experiences is specified by its T-matrix \bar{T}^α .

For plane wave excitation of a single sphere, Mie theory and the T-matrix method yield the same results. However in a dense collection of spheres the field experienced (called the exciting field) by any particle is due to both the incident field and the scattered field from neighboring particles. When this exact exciting field - which is in general not a plane wave - is known in the near, intermediate, and far field it is necessary to use the T-matrix method. This allows for decomposition of the exciting field into vector spherical waves. The T-matrix then specifies the scatterer's response to any type of excitation. The correspondence between the T-matrix and the Mie coefficients can be seen by examining the T-matrix for a spherical scatterer :

$$\bar{T} = \begin{bmatrix} \bar{T}^{(11)} & \bar{0} \\ \bar{0} & \bar{T}^{(22)} \end{bmatrix} \quad (3.11)$$

$$T_{mnm'n'}^{(11)} = \delta_{mm'nn'} T_n^{(M)} \quad (3.12)$$

$$T_{mnm'n'}^{(22)} = \delta_{mm'nn'} T_n^{(N)} \quad (3.13)$$

$$T_n^{(M)} = \frac{j_n(k_s a) [ka j_n(ka)]' - j_n(ka) [k_s a j_n(k_s a)]'}{j_n(k_s a) [ka h_n(ka)]' - h_n(ka) [k_s a j_n(k_s a)]'} \quad (3.14)$$

$$T_n^{(M)} = \frac{[k_s^2 a^2 j_n(k_s a) [k a j_n(k a)]'] - [k^2 a^2 j_n(k a) [k_s a j_n(k_s a)]']}{[k_s^2 a^2 j_n(k_s a) [k a h_n(k a)]'] - [k^2 a^2 h_n(k a) [k_s a j_n(k_s a)]']} \quad (3.15)$$

Thus $T_n^{(M)}$ and $T_n^{(N)}$ are equivalent to the Mie coefficients b_n and a_n [91], respectively for a plane wave excitation.

The final scattered field \bar{E}_s from N spheres at an observation point r is

$$\bar{E}_s(r) = \sum_{mn} [a_{mn}^{s(M)} \bar{M}_{mn}(kr, \theta, \phi) + a_{mn}^{s(N)} \bar{N}_{mn}(kr, \theta, \phi)] \quad (3.16)$$

where \bar{M}_{mn} and \bar{N}_{mn} are outgoing vector spherical wave functions.

Equation 3.10 can be derived directly from Maxwell's equations for the case of discrete scatterers in a homogeneous background. Unlike continuous random media, discrete scatterers have well-defined boundaries. Since the space occupied by the random scatterers and the space occupied by the background are distinguishable, with each region having its own permittivity, the fields in each region can be expressed in a complete spherical wave expansion and equated at the scatterer boundaries. A derivation utilizing dyadic Green's functions is given by Peterson and Ström [61]. For an N particle system occupying volumes V_1, V_2, \dots, V_N where the j th particle has the wavenumber $k_j = \sqrt{\mu\epsilon_j}$, the N particle dyadic Green's function can be written as :

$$\bar{\bar{G}}(\bar{r}, \bar{r}') = \bar{\bar{G}}_0(\bar{r}, \bar{r}') + \sum_{l=1}^N \int_{V_l} d\bar{r}'' \bar{\bar{G}}_0(\bar{r}, \bar{r}'') (k_l^2 - k^2) \bar{\bar{G}}(\bar{r}'', \bar{r}') \quad (3.17)$$

where $\bar{\bar{G}}_0$ is the free space Green's function and the above equation is valid for all \bar{r} and \bar{r}' . To put the scattering equation in more compact form, Dirac's operator notation will be used. Equation 3.17 in coordinate operator notation is

$$\bar{\bar{G}} = \bar{\bar{G}}_0 + \bar{\bar{G}}_0 \sum_{j=1}^N \bar{U}_j \bar{\bar{G}} \quad (3.18)$$

where $\bar{\bar{U}}_j = U_j \bar{\bar{I}} = U(\bar{r} - \bar{r}_j) \bar{\bar{I}}$ and

$$U(\bar{r} - \bar{r}_j) = \begin{cases} 0 & \text{for } \bar{r} \text{ not in } V_j \\ k_j^2 - k^2 & \text{for } \bar{r} \text{ in } V_j \end{cases} \quad (3.19)$$

Equation 3.18 expresses the N-particle Green's function in terms of the potential operator $\bar{\bar{U}}_j$. Using the transition operator $\bar{\bar{T}}_j = (\bar{\bar{I}} - \bar{\bar{U}}_j \bar{\bar{G}}_0)^{-1} \bar{\bar{U}}_j$ for particle j , eq. 3.18 can be written as

$$\bar{\bar{G}}_j = \bar{\bar{G}}_0 + \bar{\bar{G}}_0 \sum_{l=1, l \neq j}^N \bar{\bar{T}}_l \bar{\bar{G}}_l \quad (3.20)$$

$$\bar{\bar{G}} = \bar{\bar{G}}_0 + \bar{\bar{G}}_0 \sum_{j=1}^N \bar{\bar{T}}_j \bar{\bar{G}}_j \quad (3.21)$$

which gives the N-particle Green's function in terms of the $\bar{\bar{T}}_j$ operator and the j th particle Green's function $\bar{\bar{G}}_j$. Equation 3.10 is the result when the dyadic Green's function in the background and within the particles are expanded in vector spherical wave functions, which constitute a complete basis.

An alternate method is to write the operator equation of (3.20) and (3.21) in momentum representation for random distributions of scatterers. This has been discussed in citekn:tsang1. In the Appendix A of that paper, it is shown that for discrete scatterers in a homogeneous background the momentum representation of the operator equations of (3.20) and (3.21) is equivalent to the T-matrix approach.

3.2.1 Absorption Calculation

The internal electric field \bar{E}_{int} in each sphere can likewise be represented as

$$\bar{E}_{int}(r) = \sum_{mn} \left[c_{mn}^{(M)} Rg \bar{M}_{mn}(kr, \theta, \phi) + c_{mn}^{(N)} Rg \bar{N}_{mn}(kr, \theta, \phi) \right] \quad (3.22)$$

where $Rg\overline{M}_{mn}$ and $Rg\overline{N}_{mn}$ are the regular vector spherical wave functions. (Regular vector spherical wave functions are labeled with the prefix Rg to denote replacement in the wave function of the spherical Hankel function h_n by the spherical Bessel function j_n [81].) The relationship between the scattered field coefficients a_{mn}^s and the internal field coefficients c_{mn} is given by [81]

$$\bar{c} = (-Rg\overline{Q}^t)^{-1}\bar{a}^s. \quad (3.23)$$

The matrix $Rg\overline{Q}^t$ can be determined by equating the tangential fields at the particle's surface and is diagonal for spheres

$$Rg\overline{Q}^t = \begin{bmatrix} Rg\overline{P} & \overline{0} \\ \overline{0} & Rg\overline{U} \end{bmatrix} \quad (3.24)$$

with

$$RgP_{mnm'n'} = -ikk_s J_{mnm'n'}^{(21)} - ik^2 J_{mnm'n'}^{(12)} \quad (3.25)$$

$$RgU_{mnm'n'} = -ikk_s J_{mnm'n'}^{(12)} - ik^2 J_{mnm'n'}^{(21)} \quad (3.26)$$

$$J_{mnm'n'}^{(12)} = a^2 \delta_{mm'} \delta_{nn'} j_n(k_s a) \frac{[ka j_n(ka)]'}{ka} \quad (3.27)$$

$$J_{mnm'n'}^{(21)} = -a^2 \delta_{mm'} \delta_{nn'} j_n(ka) \frac{[k_s a j_n(k_s a)]'}{k_s a} \quad (3.28)$$

where j_n is the spherical Bessel function and k_s is the wavenumber in the scatterers. Substituting the expression for $Rg\overline{Q}^t$ into (3.23) gives

$$c_{mn}^M = \{ika(j_n(ka)[k_s a j_n(k_s a)]' - j_n(k_s a)[ka j_n(ka)]')\}^{-1} a_{mn}^M \quad (3.29)$$

$$c_{mn}^N = \left\{ ia \left(\frac{k^2}{k_s} j_n(ka)[k_s a j_n(k_s a)]' - k_s j_n(k_s a)[ka j_n(ka)]' \right) \right\}^{-1} a_{mn}^N, \quad (3.30)$$

where the prime indicates differentiation with respect to the Bessel function argument. The internal field in (3.22), together with (3.29) and (3.30), can then be used to calculate the system absorption cross section given by

$$\sigma_{aN} = \sum_{\beta=1}^N \int_V k_s \epsilon_r'' |\bar{E}_{int}^\beta(r')|^2 dV', \quad (3.31)$$

where the integration is over the sphere volume V and ϵ_r'' is the imaginary part of the relative permittivity for the spheres. Due to orthogonality of the spherical wave functions, the expression for σ_{aN} involves no coupling between the electric and magnetic dipole contributions (i.e., with coefficients c_{mn}^M and c_{mn}^N for $n = 1$), and contributions from these two fields can be considered separately. The absorption rate κ_a for a volume V is given by $\kappa_a = \sigma_{aN}/V$.

The absorption under the independent assumption can be expressed in terms of the Mie absorption cross section σ_a , where $\sigma_a = \sigma_t - \sigma_s$ and

$$\sigma_t = \frac{2\pi}{k^2} \sum_{n=1}^{\infty} (2n+1) \{ \text{Re}(a_n + b_n) \} \quad (3.32)$$

$$\sigma_s = \frac{2\pi}{k^2} \sum_{n=1}^{\infty} (2n+1) (|a_n|^2 + |b_n|^2), \quad (3.33)$$

where σ_t and σ_s are the Mie total and scattering cross sections, respectively, and a_n and b_n are the Mie field coefficients. The absorption coefficient for N spheres in a volume V is given by $\kappa_a = N\sigma_a/V$.

In dense media, the scattered field from a particle is a result of both the incident field and the fields from surrounding particles, as expressed in (3.10). The Mie absorption cross section in (3.10) assumes that the absorption is due to the incident plane wave. Thus at higher fractional volumes, where the close sphere packing greatly influences the local exciting field that a given particle experiences, the internal field can be quite different from that predicted by independent Mie calculation.

3.2.2 Scattering Calculation

In the Monte Carlo simulations, aggregations of spheres are randomly placed within N_r test volumes in a manner corresponding to either a sticky or a non-sticky pair distribution function $g(r)$. The scattered fields are calculated using (3.10) and (3.16) and averaged over N_r realizations. The scattering and absorption of radiant energy from the incident wave represents transfer of energy from the coherent beam into incoherent power due to the presence of the scatterers. To separate the coherent and incoherent components, the scattered field is averaged to give the coherent scattered field. The coherent scattered field $\langle E_s \rangle$ is calculated by

$$\langle \overline{E}_s \rangle = \frac{1}{N_r} \sum_{\sigma=1}^{N_r} \overline{E}_s^{\sigma} \quad (3.34)$$

where σ is the realization index with $\sigma = 1, 2, \dots, N_r$ realizations. \overline{E}_s^{σ} is the final scattered field from the elemental volume of many scatterers and includes their coherent near and intermediate range interactions. The incoherent field is the difference between the total field and the coherent field $\overline{\mathcal{E}}_s^{\sigma} = \overline{E}_s^{\sigma} - \langle \overline{E}_s \rangle$. Calculation of the scattering coefficient κ_s from the incoherent scattered field $\overline{\mathcal{E}}_s$ can be expressed as

$$\kappa_s = \frac{1}{V} \int_0^{\pi} d\theta_s \sin(\theta_s) \int_0^{2\pi} d\phi_s \frac{R^2}{N_r} \sum_{\sigma=1}^{N_r} |\overline{\mathcal{E}}_s|^2 \quad (3.35)$$

3.2.3 Choice of Statistical Sample

The Monte Carlo volume must satisfy three criteria. One, the test volume must be small enough such that $V \ll (\frac{1}{\kappa_e})^3$, then the attenuation of the original incident wave traveling through the volume is negligible. The volume is not, however, infinitesimally small, but is large in comparison to the wavelength ($V \gg \lambda^3$) so that, two, the phase of the wave varies appreciably across the volume to create random phase situations. Lastly, the number of enclosed spheres in the volume must be large enough

to represent a random sampling of scatterers ($N \gg 1$). When the scattered fields are calculated within such a volume, the randomness of the wave's phase and of the particle's position destroys some of the phase coherence in the system and serves to speed the convergence of the iteration.

3.2.4 Computational Consideration

Unlike continuous random media, discrete scatterers have well-defined boundaries. Since the space occupied by the random scatterers and the space occupied by the background are distinguishable, with each region having its own permittivity, the fields in each region can be expressed in a complete vector spherical wave expansion and equated at the scatterer boundaries using Maxwell's equations. For the case of discrete scatterers in a homogeneous background, Maxwell's equations can be cast into the Foldy-Lax multiple scattering equations in matrix notation as [81] and the solution to (3.10) can be obtained through iteration. The result for the $(\nu + 1)$ iteration is

$$\begin{aligned} \bar{a}^{s(\alpha)(\nu+1)} = & \sum_{\substack{\beta=1 \\ \beta \neq \alpha}}^N \bar{T}^{\alpha} \bar{\sigma}(k \bar{r}_{\alpha} \bar{r}_{\beta}) \bar{a}^{s(\beta)(\nu)} + \exp(i \bar{k}_i \cdot \bar{r}_{\alpha}) \bar{T}^{\alpha} \bar{a}_{inc} \end{aligned} \quad (3.36)$$

where the superscript ν denotes the ν th-iterated solution, and the initial solution is just the incident field coefficients. To obtain the final solution for $\bar{a}^{s(\alpha)(\nu+1)}$, the system of equations in (3.36) is iterated until the maximum change in the field coefficients from one iteration to the next is less than 5%, at which point the solution is considered to have converged.

As stated in Section 3.2.3, the random sphere distribution increases the speed of convergence. This effect was observed in our initial attempts to solve (3.36) for a system with random, non-sticky scatterers occupying 40% by volume. As described in

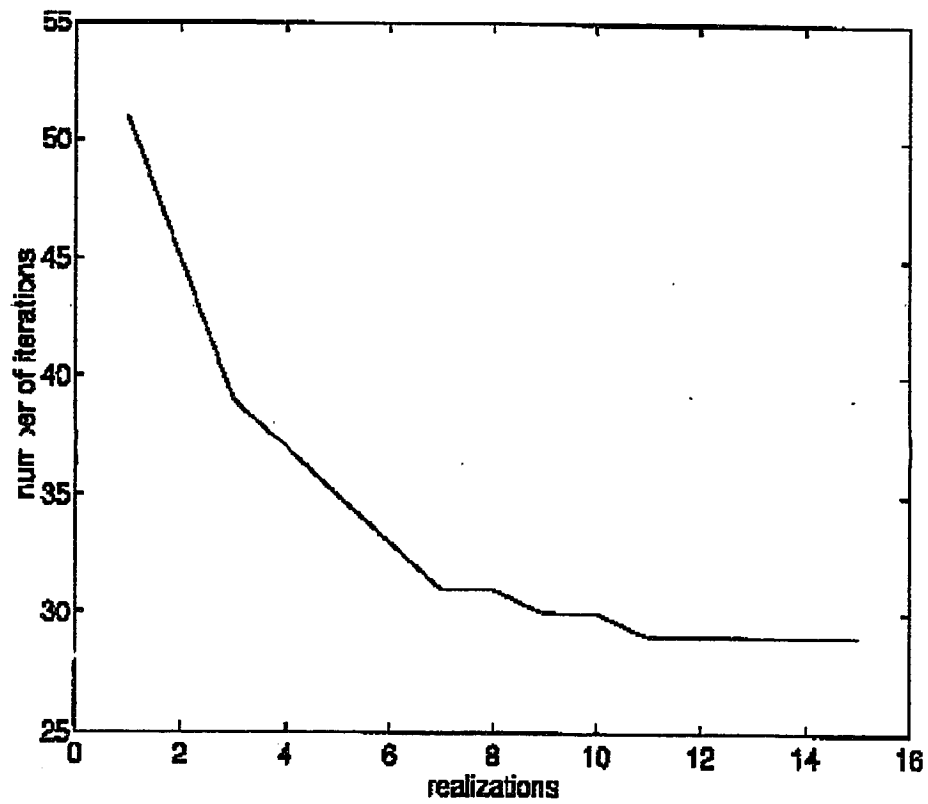


Figure 3.4: The number of iterations vs. realizations for 3500 spheres that are 40% by volume with $ka = 0.2$. The initial realization has some periodicity which is destroyed by shuffling in later realizations, and thus randomness increases from left to right.

Section 3.1.1, a system this dense requires initial periodic particle placement and then sufficient shuffling, so that the resulting positions are random. In Fig. 3.4 we show the number of iterations necessary for convergence of (3.36) when inadequate shuffling causes some remaining periodicity in the sphere placement. Figure 3.4 shows the number of realizations along the horizontal axis (where each realization results from shuffling the previous one, and thus randomness increases from left to right). The effect of even a slight amount of periodicity is an increase in the number of iterations necessary for convergence, because of the destruction of the system's random nature. Thus the first few realizations in this attempt required over 50 iterations, compared with ~ 30 when the periodicity was decreased by additional shuffles. For $f_v = 40\%$ and $ka = 0.2$, a truly random configuration required 23 iterations for the results to converge.

The number of iterations necessary for convergence depends on the fractional volume of the spheres, the dielectric contrast, and the sphere radius. In this chapter we present results for spheres with permittivity $\epsilon_s = 3.2\epsilon_0$ and with size parameter $k_s a = 0.2$. Thus the number of iterations depends on the fractional volume and particle position. For the lower density case of $f_v = 15\%$, approximately 7 iterations were necessary for the solution to converge in contrast to the 23 iterations for $f_v = 40\%$. This makes sense physically as it indicates that multiple scattering effects become more important for highly dense systems. When the sphere size is small, the T-matrix becomes small and the number of iterations decreases. For the case of $ka = 0.1$, the number of iterations needed for convergence remains fixed at six for all fractional volumes.

The dimension of $\bar{a}^{s(\alpha)}$ is determined by the number of spherical harmonics that are considered. For sparse systems with small scatterers, it is sufficient to consider only the electric dipole term. Once the particles become more closely packed, the near-field effects become important and higher order multipoles need to be considered. In this chapter, we calculate the field due to both the electric and the magnetic dipole. In this

formulation, $\bar{a}^{s(\alpha)}$ is a 6x1 column vector, and $\bar{\bar{\sigma}}(k\bar{r}_\alpha\bar{r}_\beta)$ is a 6x6 translation matrix. Thus the matrix in equation (3.10) has rank $6N$ (e.g., 18,000 for a volume containing 3000 spheres). Because this exceeds the available memory capacity, we calculate each matrix element and the spherical translation matrix as they are needed and discard them after each use. The computation time for a single iteration is thus $O((MN)^2)$, where M is the number of spherical harmonics considered, which is $M = 6$ in the dipole case. As stated above, the number of iterations needed for even the most dense aggregation is small compared to N , and the overall computational time is $O((MN)^2)$ for the iterative solution. Of course, Monte Carlo simulations require averaging over N_r realizations.

3.3 Results

In this section we present results from the Monte Carlo simulations of aggregations of spheres. We consider sticky and non-sticky-particles and particles with a non-zero loss tangent. All Monte Carlo calculations include both the electric and magnetic dipole contributions unless specified otherwise.

3.3.1 Sticky and Non-Sticky Particles

We performed Monte Carlo simulations of non-sticky, lossless particles with a size factor of $ka = 0.2$ and $ka = 0.1$, permittivity of $\epsilon_s = 3.2\epsilon_0$, and random organization for fractional volumes of 15%, 25%, 35%, and 40%. At 40% fractional volume, the sphere packing made sequential deposition impossible and we used the shuffle algorithm outlined in Section 3.1.1. Tables 3.1 and 3.2 give the simulation parameters and computed extinction rates, which are also shown graphically along with extinction rates calculated using the independent scattering assumption, QCA, and QCA-CP in Fig. 3.5 and 3.6. The figure shows the overestimation of the extinction rates when the independent scattering assumption is made. The curves for QCA and

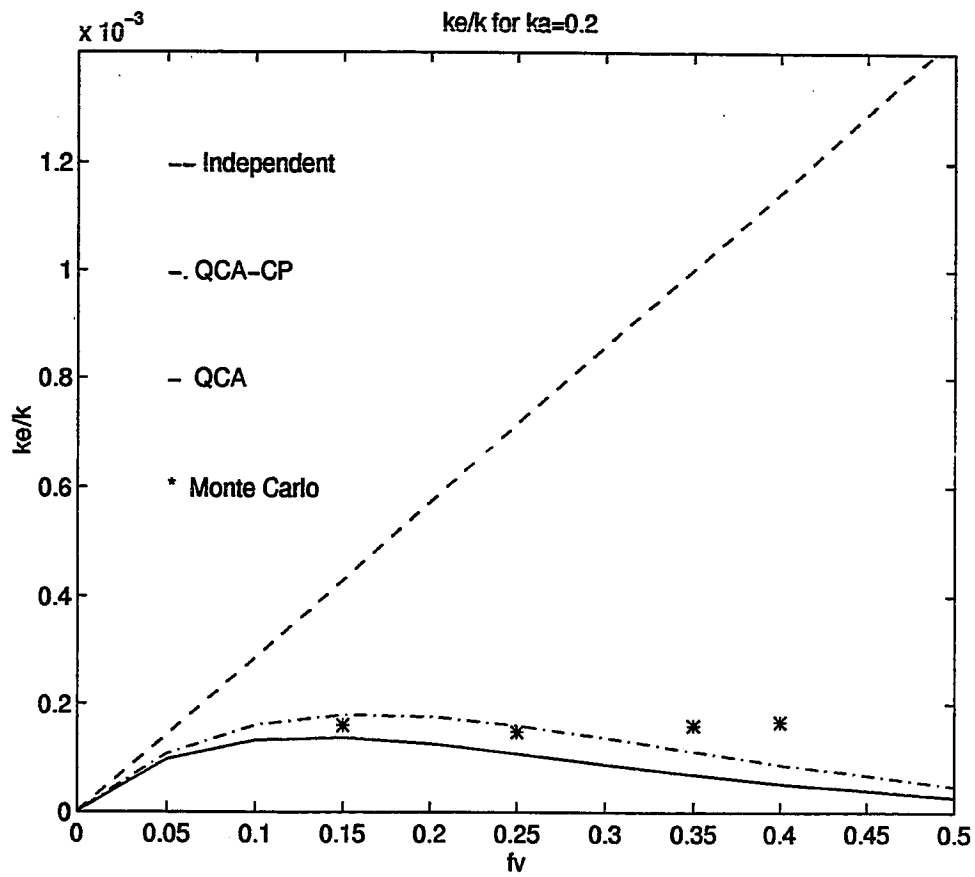


Figure 3.5: Extinction rate as a function of fractional volume; calculations based on independent assumption, QCA, QCA-CP, and Monte Carlo simulations for $ka = 0.2$.

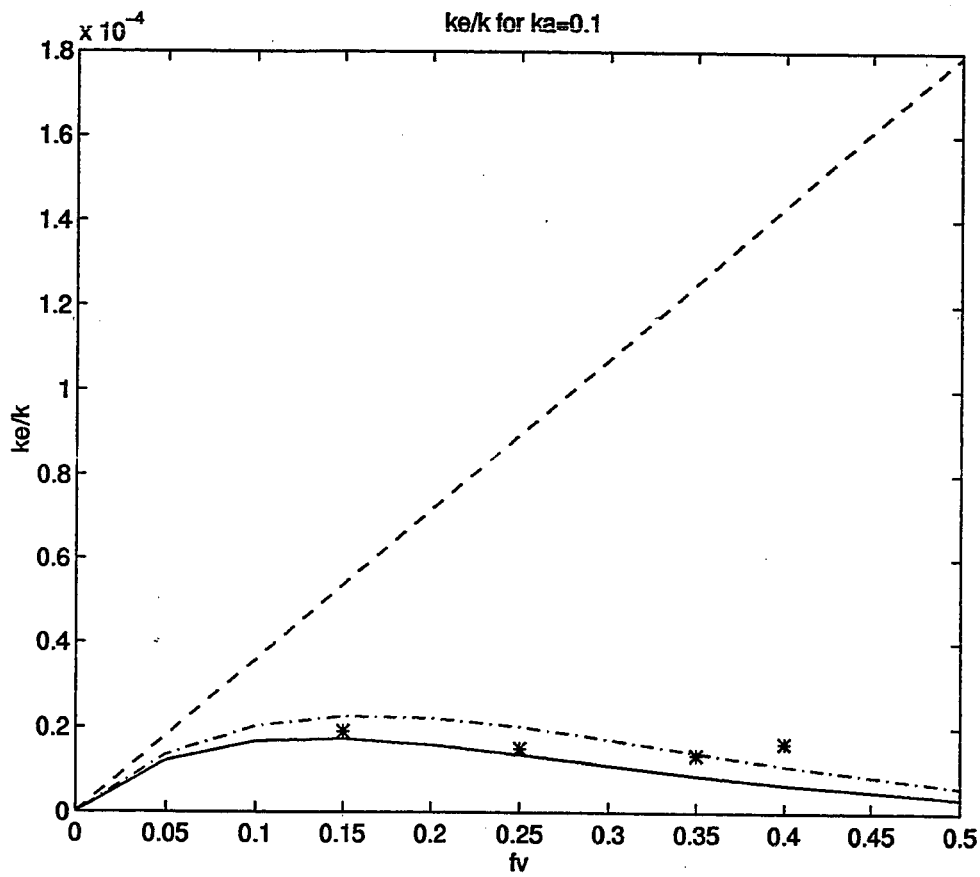


Figure 3.6: Extinction rate as a function of fractional volume; calculations based on independent assumption, QCA, QCA-CP, and Monte Carlo simulations for $ka = 0.1$.

Table 3.1: Numerical Results for lossless spheres with $ka = 0.2$ and $\epsilon_s = 3.2\epsilon_0$

Normalized Extinction Rate κ_e/k ($\times 10^{-4}$)	Fractional Volume			
	15%	25 %	35 %	40 %
Independent	4.28	7.15	10.0	11.45
QCA	1.38	1.08	0.69	0.52
QCA-CP	1.80	1.60	1.12	0.88
Monte Carlo	1.61	1.48	1.60	1.67
# Spheres, N	3000	3000	3000	3500
# Iterations, N_I	7	9	15	23
# Realizations, N_r	15	15	15	20

Table 3.2: Numerical Results for lossless spheres with $ka = 0.1$ and $\epsilon_s = 3.2\epsilon_0$

Normalized Extinction Rate κ_e/k ($\times 10^{-5}$)	Fractional Volume			
	15%	25 %	35 %	40 %
Independent	5.37	8.95	12.53	14.32
QCA	1.72	1.35	0.86	0.65
QCA-CP	2.25	2.00	1.40	1.10
Monte Carlo	1.90	1.50	1.35	1.63
# Spheres, N	3000	3000	3000	3500
# Iterations, N_I	6	6	6	6
# Realizations, N_r	15	15	15	20

QCA-CP increase as a function of fractional volume to a maximum of approximately 15%, then begin again to decrease, with QCA underpredicting the scattering. The fractional volume at which maximal attenuation occurs depends on the size parameter of the particles. The Monte Carlo results (shown as asterisks) agree fairly well with those obtained using QCA-CP, until the higher fractional volumes are reached, at which point the Monte Carlo simulations predict greater attenuation than does QCA-CP. Initially we thought that this difference could be due to the effect of the magnetic dipole, which is included in the Monte Carlo scattering calculations but is not present in the QCA-CP solution. However, Monte Carlo simulations containing only the electric dipole produced attenuations that were only slightly lower than those from simulations with both the electric and magnetic dipoles. It seems that as the sphere packing becomes closer in the higher fractional volumes, the near fields generated by neighboring particles produce effects on the spheres that are not included in the low frequency approximations used in QCA-CP. *The validity of the low-frequency approximation thus appears to be dependent on the density of the scatterers.*

This can be seen by comparing the results in Fig. 3.5 which are for a $ka = 0.2$ with those in Fig. 3.6 which are for particles with $ka = 0.1$. At 35% fractional volume there is a difference between the attenuation predicted by QCA-CP and by the Monte Carlo simulations for the case of $ka = 0.2$, but not for $ka = 0.1$. At 40% fractional volume results from particles of both sizes show a difference between the Monte Carlo simulations and QCA-CP, but it is less pronounced for the smaller spheres. As the density of the system is increased, the particle size must be decreased to satisfy the low-frequency solution to QCA-CP.

In Fig. 3.7, the Monte Carlo results are shown for spheres with $ka = 0.2$ and $\epsilon_s = 3.2\epsilon_0$ for spheres both with and without an adhesive potential. The spheres with an adhesive potential were deposited as discussed in Section 3.1 with a “stickiness” of $\tau = 0.2$, and a pair distribution function $g(r)$ as shown in Fig. 3.1. In Fig. 3.7 it can be clearly seen that the sticky-particles (asterisk) show a greater extinction

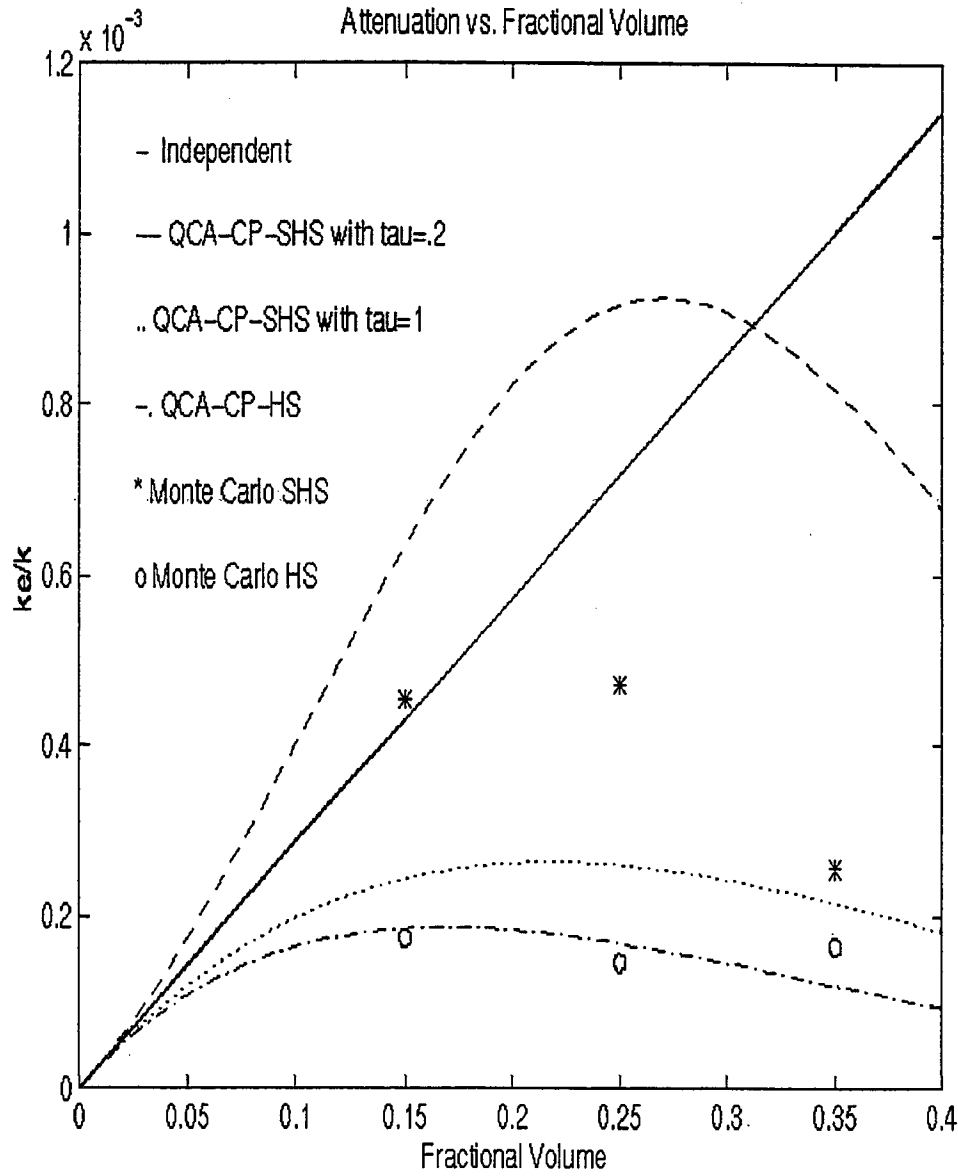


Figure 3.7: Extinction rate as a function of fractional volume for non-sticky spheres and sticky spheres with $\tau = 0.2$ and $\tau = 1.0$ and $ka = 0.2$; calculations based on independent assumption, QCA-CP and Monte Carlo simulations.

rate than do the non-sticky particles (open circles). Since *the only difference* between the two simulations is the pair distribution function, we can draw the important conclusion that the particle placement is a crucial factor in estimating the extinction properties. This is intuitive when the placement is influenced by a clustering nature, and the particles clump to effectively form “larger particles”. As one would expect, these “larger particles” exhibit a greater amount of attenuation because of their size. However, as we showed in [25], modeling the irregular clusters as large spheres produces incorrect results. Again, intuitively, one would expect different scattering characteristics from a chain-like structure with a high axial ratio than from a sphere of comparable size. In particular, the local polarization of the clusters will differ greatly. Even though the orientation of the clusters of spheres is random, the behavior of the wave does respond to the irregularities of these structures.

In chapter 1 we presented extinction rates for sticky spheres calculated with QCA and QCA-CP. Also shown in Fig. 3.7 with the results from Monte Carlo simulations are results calculated using QCA-CP. Both calculation methods yield extinction rates that are greater than those calculated from non-sticky spheres. However, the QCA-CP results are higher for a given τ than for the Monte Carlo.

3.3.2 Lossy Particles

As discussed in Section 3.2.1, the absorption rate of densely packed spheres can differ from that given by the independent assumption. This effect of “enhanced absorption” is shown in Fig. 3.8. The figure shows the absorption, scattering, and extinction coefficients of $N = 2000$ spheres with a permittivity of $\epsilon_s = (3.2 + i0.01)\epsilon_0$ and a size factor of $ka = 0.2$ as a function of fractional volume. The absorption rates were calculated from Monte Carlo simulations of randomly deposited spheres (plus signs), and from the independent Mie absorption assumption for a system of N spheres (dotted line). The absorption rate when the internal field is calculated explicitly in the Monte Carlo simulations is higher than predicted from the independent assumption

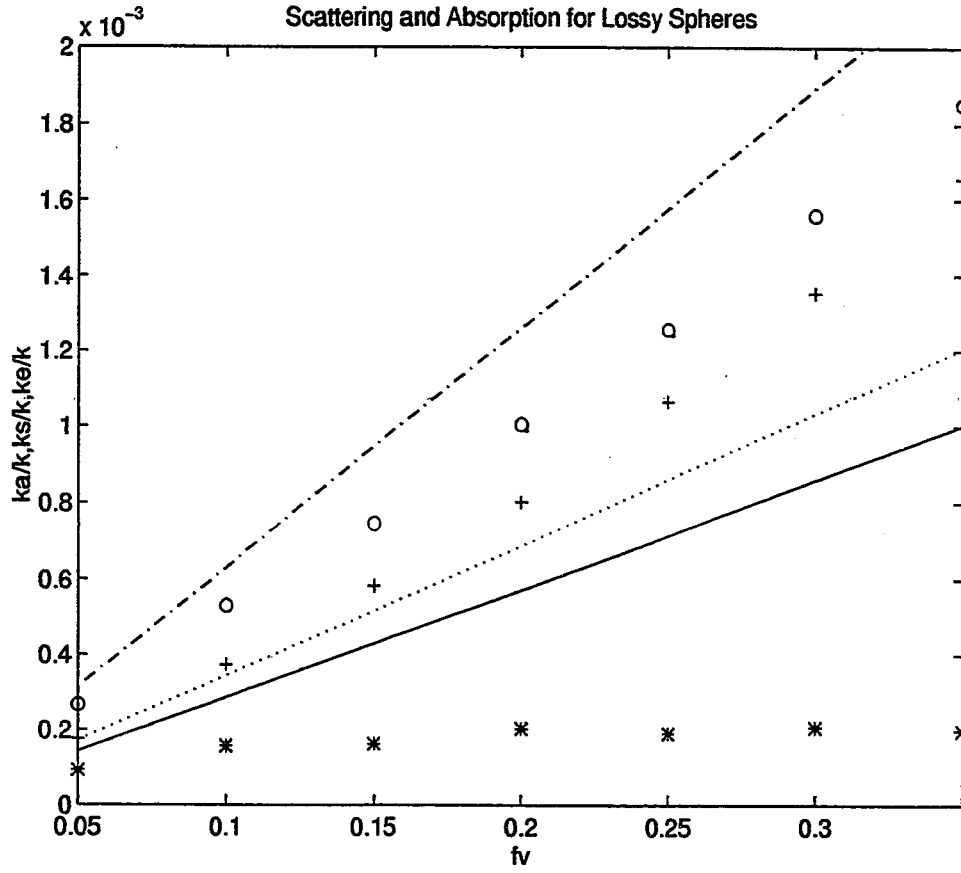


Figure 3.8: Normalized absorption, scattering and extinction from Monte Carlo simulations and independent Mie assumption for spheres with $\epsilon_s = (3.2 + i0.01)\epsilon_o$ and $ka = 0.2$. Monte Carlo results shown as (+) for absorption, (*) for scattering, and (o) for extinction. Independent absorption shown as dotted line, scattering as solid, and extinction as dash-dot.

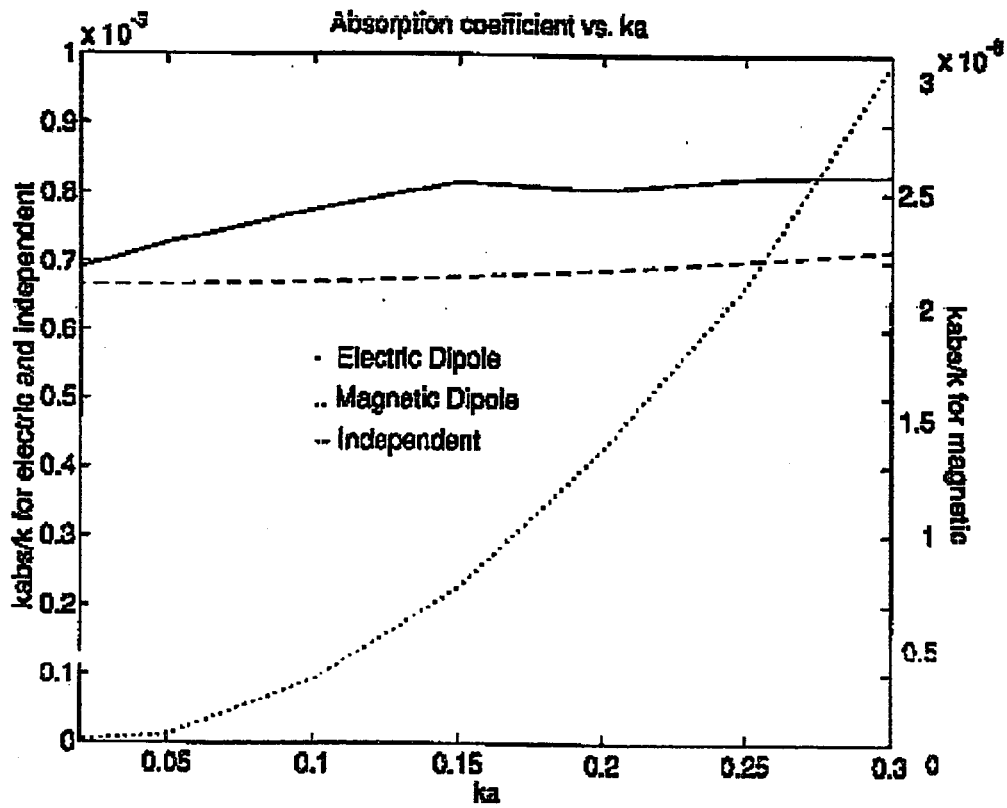


Figure 3.9: Absorption rate as a function of size ka from Monte Carlo simulations of spheres with $f_v = .2$ for electric dipole and magnetic dipole.

(about 25% greater at 30% fractional volume).

The calculated absorption rate for the higher fractional volumes is also greater than that predicted using the Maxwell-Garnet mixing formula (MG) [54]

$$\kappa_a/k = \epsilon''_{eff}/\sqrt{\epsilon'_{eff}\epsilon} \quad (3.37)$$

$$\epsilon_{eff} = \epsilon'_{eff} + i\epsilon''_{eff} = \epsilon \frac{1 + 2fy}{1 - fy}$$

$$y = \frac{\epsilon_s - \epsilon}{\epsilon_s + 2\epsilon}. \quad (3.38)$$

This discrepancy may seem surprising since MG takes into account the influence of nearby particles. However, MG uses a low-frequency approximation and does not vary as a function of frequency. We found that as the fractional volume *increases*, we needed to *decrease* ka to produce absorption rates that agree with MG. For example, at 20% fractional volume MG predicts an absorption coefficient of $k_a/k = 0.7 \times 10^{-3}$. For a $ka = 0.2$, Monte Carlo simulations give an absorption rate of $k_a/k = 0.8 \times 10^{-3}$. If ka is decreased to $ka = 0.02$ (i.e., lower frequency), our calculated values agree with MG. These results suggest that, for densely packed particles, the threshold for low-frequency approximations depends on fractional volume.

Monte Carlo simulations were also run for spheres with a stickiness of $\tau = 0.2$ and $\epsilon_s = (3.2 + i0.01)\epsilon_o$. The resulting absorption rates showed the effect of absorption enhancement, but did not differ significantly from the non-sticky case. This indicates that the absorption is not affected by clustering or sphere placement.

The absorption rates in Fig. 3.8 were calculated from the electric dipole only. We also calculated the absorption resulting from the magnetic field contribution and found that it was several orders of magnitude smaller than that appearing due to the electric dipole. In Fig. 3.9 the absorption rates due to the electric and magnetic dipoles are shown as a function of ka . The contribution of the magnetic dipole increases more rapidly as a function of ka than does the contribution of the electric dipole, but its magnitude is still negligible in comparison with the small ka considered

(notice different scales). However, the rapid growth of this term indicates that the effect of the magnetic field increases in higher-frequency regimes.

3.4 Conclusions

In this chapter we have presented scattering and absorption coefficients from Monte Carlo simulations of densely packed dielectric, absorbing spheres. The spheres were deposited into a test volume in a random fashion, both with and without surface adhesion. Scattering and absorption were calculated using a numerically exact iterative formulation of Maxwell's multiple scattering equations, in which the contributions of the electric and magnetic dipoles were considered.

Results of these simulations show a clear dependence on the initial placement of the spheres. When interparticle adhesive forces cause clustering of the spheres, the scattering increases because of the effectively larger particle the clusters represent. This is in agreement with previous research on single fractal aggregations, which also found an increase in scattering. Both QCA-CP and the Monte Carlo simulations predict this increase in scattering for sticky spheres relative to the non-sticky case, but the magnitude of the increase is overestimated by QCA-CP. The increase is less pronounced at higher fractional volumes since the declining freedom of sphere placement curtails the clustering behavior.

For non-sticky-particles, the scattering predicted by QCA and QCA-CP agrees well with the results of the Monte Carlo simulations. At higher fractional volumes, QCA and QCA-CP predict slightly lower extinction rates than the Monte Carlo simulations, perhaps due the low-frequency approximations used in the solution for QCA and QCA-CP. The validity of the low-frequency approximation depends on ka and on the fractional volume. For a given ka , there is a threshold fractional volume above which the low-frequency assumption no longer holds. The value of the threshold decreases as ka increases.

For both sticky and non-sticky spheres, the absorption coefficient for an ensemble of absorbing spheres was larger than that predicted by assuming independent absorption. This is due to a modulation of each sphere's local exciting field as a result of the neighboring particles. In essence, the high local fields aid the ability of each sphere to absorb incident energy. The validity of the independent absorption assumption again depends on ka and the fractional volume, as observed for the validity of the low-frequency approximations used in QCA-CP. Results from a low-frequency approximation begin to disagree with the Monte Carlo results when fractional volumes greater than a threshold value are considered. The value of the threshold decreases with increasing ka .

Chapter 4

SCATTERING PROPERTIES FROM MONTE CARLO SIMULATIONS WITH APPLICATION TO REMOTE SENSING OF SNOW

In this Chapter, we employ Monte Carlo simulations to calculate the phase matrix, effective permittivity, and scattering coefficient for a random medium consisting of densely packed spheres up to 5000 in number. These quantities are then used in radiative transfer theory to calculate the bistatic scattering properties of the dense media.

Conventionally, analytic theory has been applied for the second moment of the field leading to the Bethe-Salpeter equation. A correlated ladder approximation has been applied to Bethe-Salpeter equation to calculate intensities. It has been shown that QCA-CP together with the correlated ladder approximation obeys energy conservation. The two approximations together also lead to dense media radiative transfer equation (DMRT). In the long wavelength limit, the phase matrix of the dense media radiative transfer equation is of the form of the Rayleigh phase matrix but with different extinction coefficients and albedos from conventional radiative transfer theory of independent scattering.

Numerical results indicate that the co-polarized part of the phase matrix is in good agreement with that DMRT under QCA-CP and the correlated ladder approximation. However, the Monte Carlo simulations show that the depolarization can be substantially larger than conventional theory. The strong depolarized return is due to coherent wave interaction among the spheres leading to electrical dipole moments of

spheres that are not parallel to the incident electric field. The level of depolarization is still substantially lower than that of the co-polarized component. Thus it has little effect in energy conservation that QCA-CP and correlated ladder approximation obey.

In section 4.4.4 we apply the numerical results to microwave remote sensing of snow covered regions [84],[48]. The scattering coefficient and the phase matrix derived from the Monte Carlo simulations are used in a second order radiative transfer model [71] to determine the amount of scattering from a snow layer overlying a homogeneous half space of soil. These results are compared to those obtained using DMRT and the independent scattering assumption. The characteristics of a snow layer can also change due to metamorphic forces [14] and affect the microwave response. We also show that the sticky particle model introduced in previous chapters can be used in a radiative transfer model to match simultaneously the co-polarized and depolarized microwave scatter return of snow.

Another attribute of a discrete random medium is its effective permittivity. In this chapter we compare the response of the coherent wave within the Monte Carlo volume to that of a homogeneous volume to determine the effective permittivity. We directly obtain the real part of the permittivity by tracking the amplitude and phase of the average internal electric dipole as the coherent wave travels through the medium. The results of the effective permittivity are in good agreement with Clausius-Mossotti.

4.1 Radiative Transfer Equation

The transport of radiant energy through a space of randomly distributed spherical particles as shown in Fig. 4.1 can be expressed by the vector radiative transfer (RT) equation for the specific intensity \bar{I} :

$$\cos(\theta) \frac{d\bar{I}(\theta, \phi, z)}{dz} = -\kappa_e \bar{I}(\theta, \phi, z) + \int_0^{2\pi} d\phi' \int_0^\pi \pi d\theta' \sin(\theta') \bar{P}(\theta, \phi, \theta', \phi') \cdot \bar{I}(\theta, \phi, z) \quad (4.1)$$

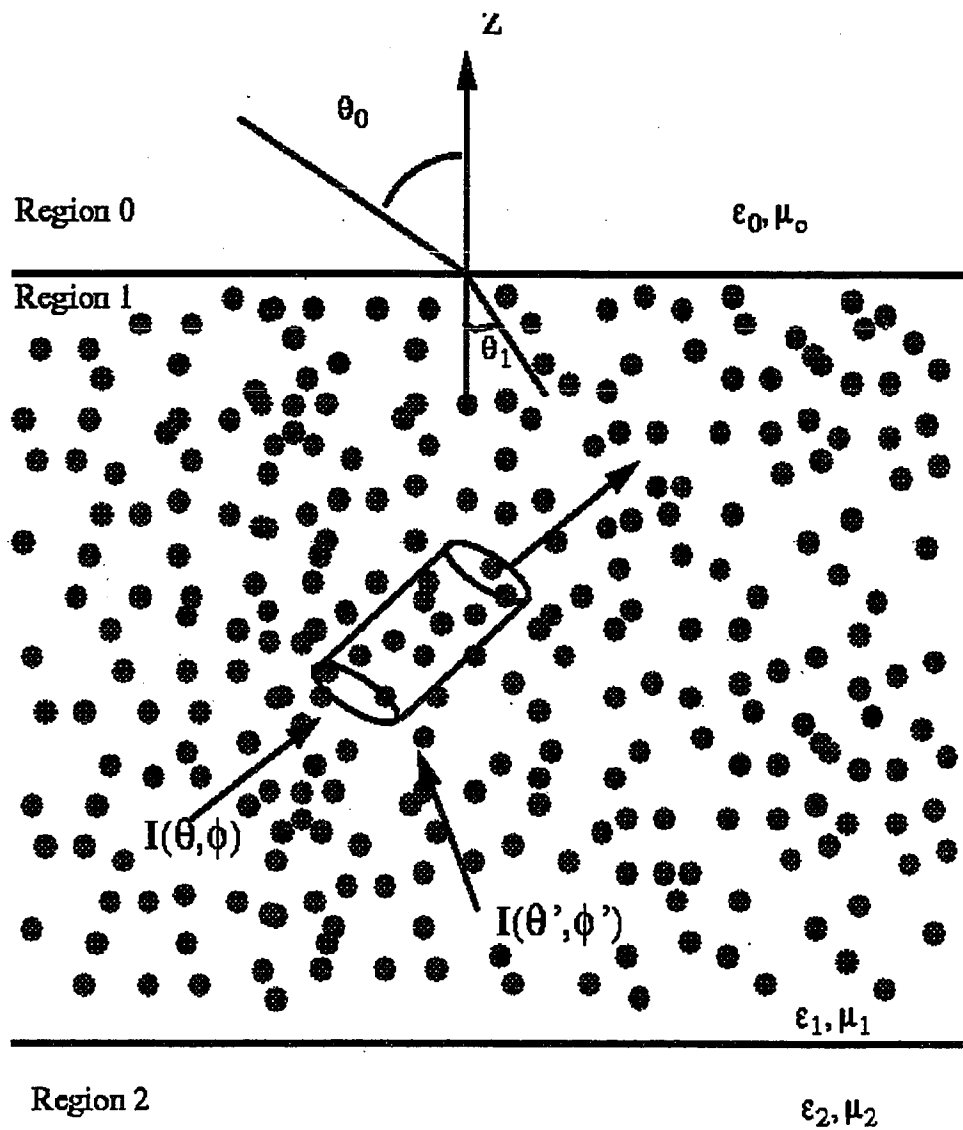


Figure 4.1: Geometry of the radiative transfer problem for a planar layer of spherical scatters in region 1 covering a homogeneous half-space in region 2 where Z is normal to the planar interfaces. Elemental volume for calculation of radiative transfer parameters shown.

where κ_e is the extinction coefficient with $\kappa_e = \kappa_s + \kappa_a$, κ_s and κ_a are the scattering and absorption coefficients, respectively, and $\bar{P}(\theta, \phi, \theta', \phi')$ is the phase matrix describing redistribution of scattered energy from direction θ, ϕ into direction θ', ϕ' . Application of boundary conditions at the planar interfaces $z = 0, z = -d$ requires knowledge of the effective permittivity ϵ_{eff} in region 1. Thus solution of equation 4.1 requires specification of κ_e , $\bar{P}(\theta, \phi, \theta', \phi')$, and ϵ_{eff} and will be influenced by the method with which they are obtained.

The second order iterative solution for active remote sensing of a layer of spherical scatterers overlying a homogeneous half space has been presented in the past [71] with results obtained using the classical assumption of independent scattering. The radiative transfer (RT) solution for the geometry shown in Fig. 4.1 can be obtained iteratively from the integral form of the RT equations. The expression for the upwelling intensity in region 1 is :

$$\begin{aligned}
 \bar{I}(\theta, \phi, z) = & e^{-\kappa_e z \sec(\theta)} \bar{F}(\theta) \cdot \bar{R}_{12}(\theta) \cdot \bar{T}_{01}(\theta_0) \cdot \bar{I}_{0i}(\pi - \theta_0, \phi_0) e^{-\kappa_e d \sec(\theta)} + e^{-\kappa_e z \sec(\theta)} \sec(\theta) \\
 & \times \int_{-d}^z dz' e^{K e z' \sec(\theta)} \int_0^{\pi/2} d\theta' \sin \theta' \int_0^{2\pi} d\phi' [\bar{P}(\theta, \phi, \theta', \phi') \cdot \bar{I}(\theta', \phi', z') \\
 & + \bar{P}(\theta, \phi, \pi - \theta', \phi') \cdot \bar{I}(\pi - \theta', \phi', z')] + e^{-K e z \sec(\theta)} \sec(\theta) \bar{F}(\theta) \cdot \bar{R}_{12}(\theta) e^{-2K e d \sec(\theta)} \\
 & \times \int_{-d}^0 dz' e^{-K e z' \sec(\theta)} \int_0^{\pi/2} d\theta' \sin \theta' \int_0^{2\pi} d\phi' [\bar{P}(\pi - \theta, \phi, \theta', \phi') \cdot \bar{I}(\theta', \phi', z') \\
 & + \bar{P}(\pi - \theta, \phi, \pi - \theta', \phi') \cdot \bar{I}(\pi - \theta', \phi', z')] \\
 & + e^{-K e z \sec(\theta)} \sec(\theta) \bar{F}(\theta) \cdot \bar{R}_{12}(\theta) \cdot \bar{R}_{10}(\theta) e^{-2K e d \sec(\theta)} \int_{-d}^0 dz' e^{K e z' \sec(\theta)} \\
 & \int_0^{\pi/2} d\theta' \sin \theta' \int_0^{2\pi} d\phi' [\bar{P}(\theta, \phi, \theta', \phi') \cdot \bar{I}(\theta', \phi', z') + \bar{P}(\theta, \phi, \pi - \theta', \phi') \cdot \bar{I}(\pi - \theta', \phi', z')] \quad (4.2)
 \end{aligned}$$

where $\bar{F}(\theta)$, \bar{R}_{12} , $\bar{T}_{01}(\theta_0)$ and \bar{R}_{10} are coupling matrices that depend on the Fresnel reflection coefficients at the material boundaries. A similar integral equation exists for the downwelling intensity $\bar{I}(\pi - \theta, \phi, z)$; details can be found in [71]. The first order solution to eq. 4.2 is obtained by substituting in the zeroth order solution for

the upwelling and downwelling intensities, and solving the integral equation. The first order backscattering coefficients for a wave incident in the direction θ_{0i}, ϕ_{0i} are then given in terms of the first order solution $\bar{I}^{(1)}(\theta, \phi, z)$ by :

$$\sigma_{\beta\alpha}^{(1)}(\theta_{0i}) = 4\pi \cos(\theta_{0i}) \frac{\bar{\bar{T}}_{10}(\theta_{1i}) \cdot \bar{I}^{(1)}(\theta_{1i}, \pi + \phi_{0i}, z = 0)}{I_{0\alpha i}} \quad (4.3)$$

where θ_{1i} is the refracted incidence angle in region 1 (see Fig. 4.1) and $I_{0\alpha i}$ is the intensity of the incident wave. The second order solution $\bar{I}^{(2)}(\theta, \phi, z)$ is obtained by substituting the first order solution into eq. 4.1. The second order backscattering cross section $\sigma_{\beta\alpha}^{(2)}$ is given by eq. 4.3 with $\bar{I}^{(1)}(\theta_{1i}, \pi + \phi_{0i}, z = 0)$ replaced by $\bar{I}^{(2)}(\theta_{1i}, \pi + \phi_{0i}, z = 0)$.

To calculate the radiative transfer parameters, we consider an elemental volume which contains many particles as shown in Fig. 4.1. The derivation of the transfer equation is based on radiative energy in and out of the volume element. Note that there is not just one particle in the elemental volume but rather, there are many particles.

In the following sections we discuss three different methods of calculating the extinction coefficients and the phase matrix. The methods are 1) classical scattering assumption, 2) DMRT, and 3) Monte Carlo simulation.

4.1.1 Classical Radiative Transfer

The classical assumption for scattering in a collection of randomly distributed spherical scatterers is that of independent scattering. Under this assumption, the particles in the elemental volume scatter and absorb independently. Thus if there are N particles in the elemental volume, the extinction cross section of all the particles is

$$\sigma_e^N = N\sigma_e, \quad (4.4)$$

where σ_e is the extinction cross section of one particle. The extinction coefficient is defined as the extinction cross section per unit volume. Thus if V is the volume of the elemental volume, then

$$\kappa_e^{ind} = \frac{N}{V} \sigma_e = n_0 \sigma_e, \quad (4.5)$$

where n_0 is the number of particles per unit volume.

Similarly, for a single particle the distribution of scattered energy is given by the Stokes matrix $\bar{\sigma}$. Under the independent scattering assumption the phase matrix is the average of the Stokes matrix over the distribution of particles, and for identical particles

$$\bar{P}(\theta, \phi, \theta', \phi') = n_0 \bar{\sigma}(\theta, \phi, \theta', \phi'). \quad (4.6)$$

For small scatterers this reduces to the Rayleigh phase matrix [81].

4.1.2 DMRT

The assumption of independent scattering ignores correlated wave interaction when the scatterers are densely packed. For dense random media the effective wavenumber K can be calculated using the quasi-crystalline approximation with coherent potential (QCA-CP) [81]. In the low frequency limit the dispersion relation is :

$$K^2 = k^2 + f_v(k_s^2 - k^2)/\gamma \times \quad (4.7)$$

$$\left\{ 1 + i \frac{2}{9} K a^3 (k_s^2 - k^2)/\gamma \left[1 + 4\pi n_0 \int_0^\infty dr r^2 [g(r) - 1] \right] \right\} \quad (4.8)$$

$$\gamma = 1 + (k_s^2 - k^2)(1 - f_v)/(3K^2)$$

where k_s is the wavenumber of the scatterers, k is the wavenumber of the background, a is the radius of the spheres, f_v is the fractional volume of the scatterers,

and $g(r)$ is the pair-distribution function. The albedo $\tilde{\omega} = \kappa_s/\kappa_e$ can be derived from the second moment as

$$\tilde{\omega} = \frac{1}{2K''} \frac{f_v a^3}{3} |k_s^2 - k^2|^2 n_0 \left(1 + 4\pi n_0 \int_0^\infty dr r^2 [g(r) - 1] \right) \quad (4.9)$$

where K'' is the imaginary part of the effective wavenumber and $\kappa_e = 2K''$. As noted previously, DMRT follows from QCA-CP and the correlated ladder approximation. In the long wavelength limit the phase matrix of the dense media radiative transfer equation is of the form of the Rayleigh phase matrix but with the scattering coefficient calculated by the above relationships.

4.1.3 Simulation

As an alternative to either the classical model or DMRT, Monte Carlo simulations can be used to directly determine the extinction coefficient, the phase matrix, and the effective permittivity. These are calculated by using a large number of scatterers in the elemental volume and taking into account their coherent wave interactions to determine the collective scattering and interaction of the N particles in the elemental volume. Of course N has to be a large number and convergence with respect to N has to be tested. For example, the extinction coefficient can be calculated by considering the transfer of energy within this volume from the coherent wave into the incoherent wave. The elemental volume must satisfy three criteria. First, the volume must be small enough that the attenuation of energy in the incident wave as it travels through cube is small compared to the incident energy. Secondly, the volume must be large enough relative to the wavelength so that the phase of the wave varies across the volume and creates random phase situations. Finally, the number of scatterers enclosed within the volume must be large enough to represent a random sampling of scatterers.

Calculation of the radiative transfer parameters from Monte Carlo simulation differs from the previous approaches in that the N-particle collective behavior is considered [99]. The extinction coefficient from this volume is derived from the N-particle cross section per unit volume. The phase matrix is obtained from the N-particle bistatic cross section per unit volume. The effective permittivity is determined from calculation of the coherent scattered field. The phase and amplitude from the elemental volume is compared with a homogeneous volume to ascertain the effective permittivity. The details of these calculations are described in the following two sections.

4.2 Monte Carlo Simulations

The wave propagation and scattering through a large number of scatterers is computed using an exact formulation based on Maxwell's equations. The advantage of this method is that exact values for the extinction coefficient and phase matrix can be obtained and then compared with those obtained from dense media theory. In chapter 3 the formulation for the Monte Carlo simulations and the calculation of the extinction coefficient was described. In this section we discuss how the phase matrix can be computed from the scattered incoherent fields.

4.2.1 Calculation of the Phase Matrix

An N-particle collective scattering amplitude $\mathcal{F}_{\alpha\beta}$ can be defined for a volume element where N is a large number. The subscripts $\alpha = 1, 2$ and $\beta = 1, 2$ designate the polarization of the incident and scattered waves, respectively, such that $\alpha, \beta = 1$ describes a wave polarized perpendicular to the plane of incidence and $\alpha, \beta = 2$ is a wave polarized parallel to the plane of incidence. To determine an expression for $\mathcal{F}_{\alpha\beta}$ we can use the definition of the incoherent electric field $\bar{\mathcal{E}}_s^\sigma = \bar{E}_s^\sigma - \langle \bar{E}_s \rangle$ to write

$$\mathcal{E}_{\alpha\beta} = \frac{e^{ikr}}{r} \underbrace{[F_{\alpha\beta} - \langle F_{\alpha\beta} \rangle]}_{\equiv \mathcal{F}_{\alpha\beta}}. \quad (4.10)$$

where $F_{\alpha\beta}$ is the scattering amplitude of the total scattered electric field \overline{E}_s . Multiplying by a complex conjugate and taking the ensemble average then gives

$$\langle \mathcal{E}_{\alpha\beta} \mathcal{E}_{\alpha'\beta'}^* \rangle = \frac{1}{r^2} \langle \mathcal{F}_{\alpha\beta} \mathcal{F}_{\alpha'\beta'}^* \rangle \quad (4.11)$$

where for $\alpha = \alpha'$ and $\beta = \beta'$

$$\langle |\mathcal{F}_{\alpha\beta}|^2 \rangle = \langle |F_{\alpha\beta}|^2 \rangle - |\langle F_{\alpha\beta} \rangle|^2. \quad (4.12)$$

In the Monte Carlo simulations the incident wave travels in the \hat{z} direction and is polarized in the \hat{y} direction (Fig. 4.2). Thus \mathcal{F}_{11} and \mathcal{F}_{21} can be determined by considering the two components of the scattered field that travels in the xz plane or with $\phi_s = 0$. Likewise, \mathcal{F}_{22} and \mathcal{F}_{12} represent scattering from an incident wave with parallel polarization and can be determined by consideration of the scattered wave traveling in the yz plane with $\phi_s = \pi/2$. For example,

$$\begin{aligned} \langle |\mathcal{F}_{11}|^2 \rangle &= \frac{R^2}{N_r} \sum_{\sigma=1}^{N_r} |\mathcal{E}_{hs}^\sigma(\phi_s = 0, \theta_s)|^2 \\ \langle (\mathcal{F}_{11} \mathcal{F}_{12}^*) \rangle &= \frac{R^2}{N_r} \sum_{\sigma=1}^{N_r} \mathcal{E}_{hs}^\sigma(\phi_s = 0, \theta_s) \mathcal{E}_{hs}^{\sigma*}(\phi_s = \pi/2, \theta_s). \end{aligned} \quad (4.13)$$

where $\mathcal{E}_{hs}(\phi_s = 0, \theta_s)^\sigma$ is the horizontal component of the incoherent scattered field of the σ th realization evaluated at $\phi_s = 0$ and for $0 \leq \theta_s \leq 2\pi$. The phase matrix in the plane of incidence can be written as :

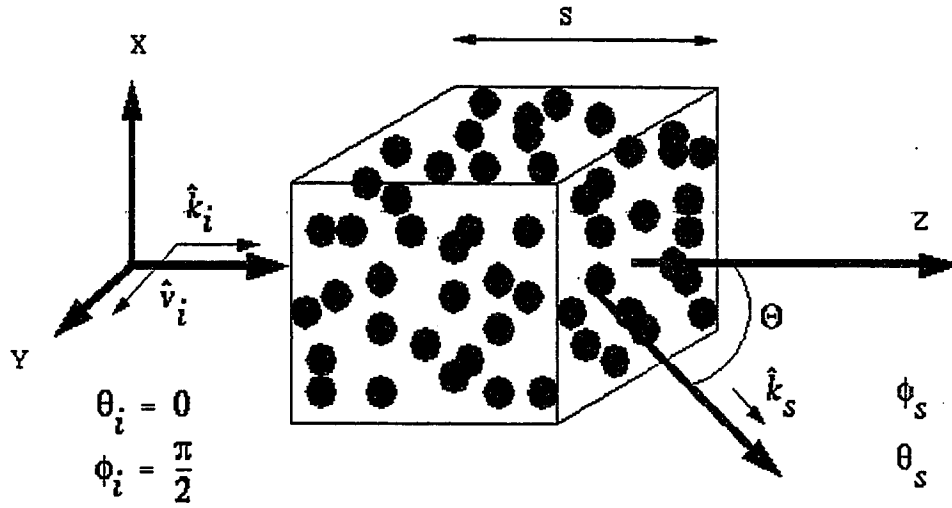


Figure 4.2: Monte Carlo Test Volume shown with incident electric field traveling in the $\hat{k}_i = \hat{z}$ direction and polarized in the $\hat{v}_i = \hat{y}$ direction. The cubic test volume has a side of length s and volume $v = s^3$. The scattered fields are in the direction θ_s and ϕ_s , where Θ is the angle between \hat{k}_i and \hat{k}_s .

$$\overline{\overline{P}}_{poi} = \begin{bmatrix} \langle |\mathcal{F}_{11}|^2 \rangle & \langle |\mathcal{F}_{12}|^2 \rangle \\ \langle |\mathcal{F}_{21}|^2 \rangle & \langle |\mathcal{F}_{22}|^2 \rangle \\ \langle 2\text{Re}(\mathcal{F}_{11}\mathcal{F}_{21}^*) \rangle & \langle 2\text{Re}(\mathcal{F}_{12}\mathcal{F}_{22}^*) \rangle \\ \langle 2\text{Im}(\mathcal{F}_{11}\mathcal{F}_{21}^*) \rangle & \langle 2\text{Im}(\mathcal{F}_{12}\mathcal{F}_{22}^*) \rangle \end{bmatrix} \quad (4.14)$$

$$\begin{bmatrix} \langle \text{Re}(\mathcal{F}_{11}\mathcal{F}_{12}^*) \rangle & \langle -\text{Im}(\mathcal{F}_{11}\mathcal{F}_{12}^*) \rangle \\ \langle \text{Re}(\mathcal{F}_{21}\mathcal{F}_{22}^*) \rangle & \langle -\text{Im}(\mathcal{F}_{21}\mathcal{F}_{22}^*) \rangle \\ \langle \text{Re}(\mathcal{F}_{11}\mathcal{F}_{22}^* + \mathcal{F}_{12}\mathcal{F}_{21}^*) \rangle & \langle -\text{Im}(\mathcal{F}_{11}\mathcal{F}_{22}^* - \mathcal{F}_{12}\mathcal{F}_{21}^*) \rangle \\ \langle \text{Im}(\mathcal{F}_{11}\mathcal{F}_{22}^* + \mathcal{F}_{12}\mathcal{F}_{21}^*) \rangle & \langle \text{Re}(\mathcal{F}_{11}\mathcal{F}_{22}^* - \mathcal{F}_{12}\mathcal{F}_{21}^*) \rangle \end{bmatrix} \quad (4.15)$$

where $\mathcal{F}_{\alpha\beta}$ depends on the angle between the incident and scattered wave Θ .

The full electromagnetic phase matrix over all input and output angles can be obtained by transformation of $\overline{\overline{P}}_{poi}$ through rotation angles ϕ_1 and ϕ_2 . The rotation angles are determined by the direction of the vertically polarized wave vector with respect to the normal \hat{n} to the plane of incidence. In terms of the incident and scattered angles they are :

$$\begin{aligned} \sin \phi_1 &= (\hat{v}_i \times \hat{n}) \cdot \hat{k}_i = (\hat{v}_i \times (\hat{k}_i \times \hat{k}_s) / \sin \Theta) \cdot \hat{k}_i = \hat{v}_i \cdot \hat{k}_s \\ \sin \phi_2 &= (\hat{v}_s \times \hat{n}) \cdot \hat{k}_s = (\hat{v}_s \times (\hat{k}_i \times \hat{k}_s) / \sin \Theta) \cdot \hat{k}_s = \hat{v}_s \cdot \hat{k}_i \end{aligned} \quad (4.16)$$

The phase matrix $\overline{\overline{P}}$ is then given by

$$\overline{\overline{P}}(\theta, \phi, \theta', \phi') = \overline{\overline{L}}(-\phi_2) \overline{\overline{P}}_{poi} \overline{\overline{L}}(\phi_1) \quad (4.17)$$

where $\overline{\overline{L}}$ is a the rotation matrix given by [38]

$$\bar{\bar{L}}(\phi) = \begin{bmatrix} \cos^2 \phi & \sin^2 \phi & \frac{1}{2} \sin 2\phi & 0 \\ \sin^2 \phi & \cos^2 \phi & -\frac{1}{2} \sin 2\phi & 0 \\ -\sin 2\phi & \sin 2\phi & \cos 2\phi & 0 \\ 0 & 0 & 0 & 1 \end{bmatrix} \quad (4.18)$$

4.2.2 Configuration for Monte Carlo Simulations for Spherical Scatterers

The configuration for the Monte Carlo simulations is shown in Fig. 4.2. The behavior of the incoherent wave in the Monte Carlo simulations is considered on a per unit volume basis using an elemental volume of Fig. 4.2 and is independent of the shape of the volume. In each realization, N spheres with permittivity ϵ_s and radius a are randomly deposited [100] into the elemental box of volume $V = s^3$ or sphere with $V = \frac{4\pi}{3}s^3$.

Quantities that are appropriate for use in the solution of the radiative transfer (RT) equation represent statistical averages with respect to the scatterer placement. They are obtained from Monte Carlo simulations by averaging over realizations where each realization consists of a different sphere distribution within the test volume V . The statistics of the sphere locations can be depicted with the bivariate probability measure called the pair distribution function. For random deposition of non-overlapping spheres the pair distribution function corresponds to the Percus-Yevick pair distribution function. An alternate deposition method for sticky hard spheres (SHS) [25, 100] utilizes a parameter τ which governs the potential of spheres to cluster together. Smaller values of τ result in more clustering or "sticking" of the spheres, and can cause a pronounced increase in scattering.

For all of the simulation results presented in this paper a single orientation of the incident wave was used and is shown in Fig. 4.2. The relationship between the incident field vectors and the angles θ_i and ϕ_i is

$$\hat{k}_i = \hat{x} \sin \theta_i \cos \phi_i + \hat{y} \sin \theta_i \sin \phi_i + \hat{z} \cos \theta_i \quad (4.19)$$

$$\hat{v}_i = \hat{x} \cos \theta_i \cos \phi_i + \hat{y} \sin \theta_i \sin \phi_i - \hat{z} \sin \theta_i \quad (4.20)$$

$$\hat{h}_i = -\hat{x} \sin \phi_i + \hat{y} \cos \phi_i. \quad (4.21)$$

The incident wave in Fig. 4.2 is an electric field traveling in the $\hat{k}_i = \hat{z}$ direction and polarized in the $\hat{v}_i = \hat{y}$ direction, with $\theta_i = 0$ and $\phi_i = \pi/2$. The scattered field has components as given above with θ_i replaced by θ_s , and ϕ_i by ϕ_s .

4.3 Coherent Wave Calculations

In the following sections we present calculations based on the behavior of the coherent wave within the Monte Carlo volume. These calculations are used to determine 1) the behavior of internal dipole moments within the scatterers and 2) the real part of the effective permittivity for the random medium.

4.3.1 Dipole Orientation

The electric dipole for the j th sphere as calculated in Monte Carlo simulations can be written as:

$$\vec{p}_{int}^j = \int_V (\epsilon_s - \epsilon_0) \vec{E}_{int}(\vec{r}) dV \quad (4.22)$$

where $\vec{E}_{int}(\vec{r})$ is given by equation 3.22 in terms of the vector spherical wave functions. The wave functions can be converted to Cartesian coordinates and the integration performed analytically.

Under the QCA approximation the dipole moment can be written :

$$\vec{p}_{int}^{QCA} = \frac{3v_0\epsilon_0\gamma}{1 - f_v\gamma} E_0 e^{i\vec{K}_r \cdot \vec{r}} \hat{e} \quad (4.23)$$

with

$$y = \frac{\epsilon_s - \epsilon_0}{\epsilon_s + 2\epsilon_0}. \quad (4.24)$$

where v_0 is the volume of the sphere and \bar{K}_r is the real part of the effective wavenumber whose calculation will be discussed later.

The incident electric field will cause alignment of the internal dipoles, and this alignment will oscillate with the incident frequency. However, there will also be slight misalignment in each particles' dipole due to the effect of the scattered fields from nearby particles (see figure 4.3). To isolate random deviations of the dipole moment the phase dependency of the coherent wave needs to be removed. This will be referred to as "de-phasing" and can be achieved by multiplication of \bar{p}_{int}^j in equation 4.22 for sphere j by the phase factor $e^{-i\bar{K}_r \cdot \bar{r}_j}$.

The coherent addition of the dipole moments will be utilized in section 4.4.2 and is defined as follows. Define the reference point \bar{r}_c as the center of the Monte Carlo test volume (for this calculation we enhance spherical symmetry by using a test volume which is spherical in shape). We can then define the coherent dipole sum $\bar{p}_{sum}(\alpha_l)$ as the addition of the "de-phased" dipoles of spheres within a distance α_l of the reference point :

$$\bar{p}_{sum}(\alpha_l) = \frac{1}{N_r} \sum_1^{N_r} \frac{1}{N_l} \sum_1^{N_l} \bar{p}_{int}^j e^{-i\bar{K}_r \cdot \bar{r}_j} \quad (4.25)$$

where N_l is the number of spheres j that satisfy $|\bar{r}_j - \bar{r}_c| \leq \alpha_l$. The coherent sum can be written $\bar{p}_{sum}(\alpha_l) = p_x(\alpha_l)\hat{x} + p_y(\alpha_l)\hat{y} + p_z(\alpha_l)\hat{z}$.

Dipole Moments due to Incident Field and Scattered Fields

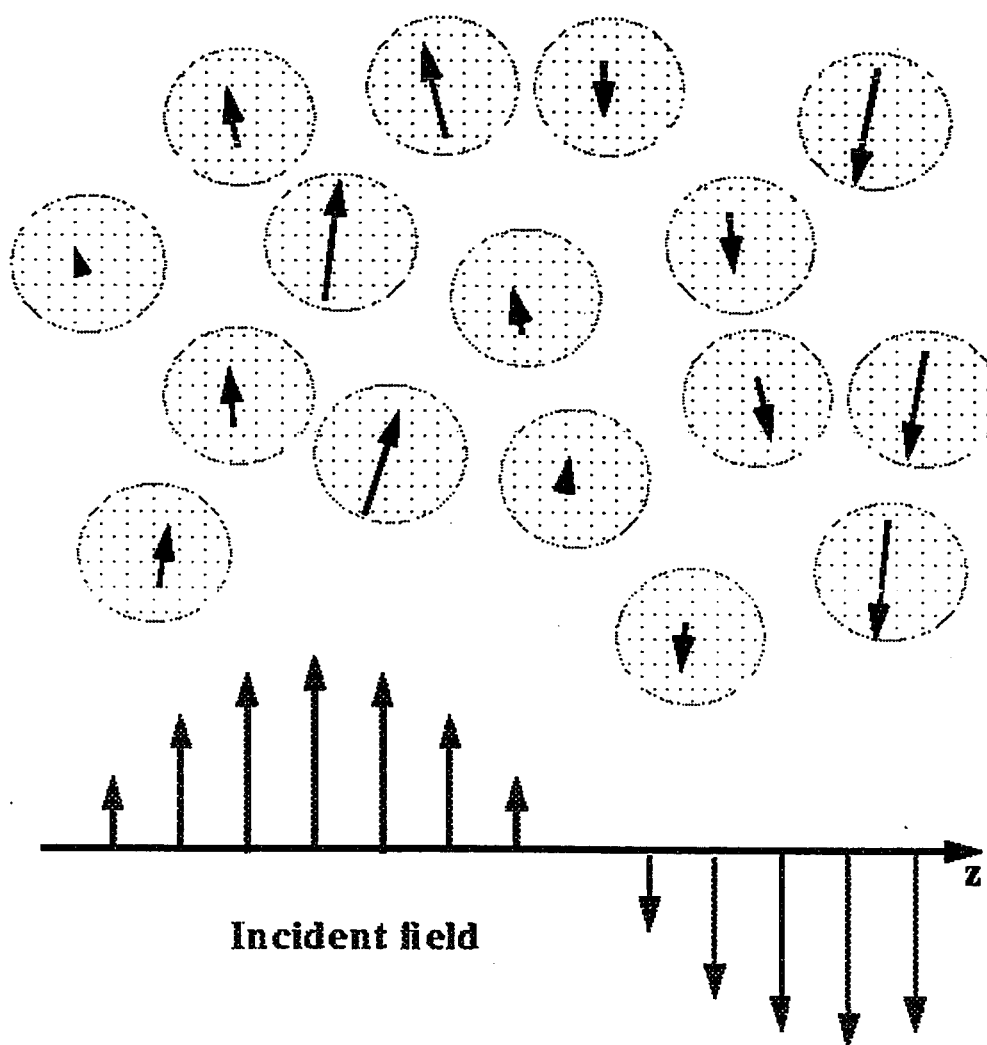


Figure 4.3: Cartoon showing the internal dipole orientation due to incident excitation and scattered fields of surrounding particles

4.3.2 Effective Permittivity

The idea of an effective permittivity for a random medium is that if the random medium were replaced by a homogeneous medium that responds to electromagnetic excitation in a identical fashion as the original random medium, the permittivity of the homogeneous medium is said to be the effective permittivity of the random medium. This concept has been explored and utilized extensively in the past.

In the Monte Carlo simulations the coherent wave responds to the size, shape and effective permittivity of the test volume. To determine the effective permittivity of the collection of spherical scatterers, the scattered coherent field can be compared with the field scattered from a homogeneous volume of the same size and shape as the Monte Carlo test volume. The permittivity of this homogeneous volume when the scattered fields are the same is the effective permittivity of the random medium.

The test volume used in the Monte Carlo simulations for the effective permittivity calculations is a sphere with diameter s . The Mie scattering cross section from a sphere with the same diameter and with a permittivity ϵ_{eff} is denoted as $\sigma_{s,Mie}$. The permittivity at which the Mie cross section is equal to that produced by the coherent scattering from the Monte Carlo spherical test volume is then - by definition - the effective permittivity of the random media. This quantity can be determined by varying ϵ_{eff} in the calculation of $\sigma_{s,Mie}$ until the following equality is satisfied :

$$\sigma_{s,Mie} = \int_0^\pi d\theta_s \sin(\theta_s) \int_0^{2\pi} d\phi_s \frac{R^2}{N_r} \sum_{\sigma=1}^{N_r} |\overline{E}_s^\sigma|^2 \quad (4.26)$$

where \overline{E}_s^σ is the total scattered field. The effective permittivity of the Mie sphere contains an imaginary component that accounts for the loss of energy due to scattering within the medium. The imaginary part of the effective permittivity can be calculated from its relationship to the extinction coefficient under the assumption that $\epsilon_{eff}'' \ll \epsilon_{eff}'$:

$$\begin{aligned}
\kappa_e &= 2k_0 \text{Im} \left\{ \sqrt{\epsilon_{eff}} \right\} \\
&= 2k_0 \text{Im} \left\{ \sqrt{\epsilon'_{eff}} \sqrt{1 + i \frac{\epsilon''_{eff}}{\epsilon'_{eff}}} \right\} \simeq k_0 \frac{\epsilon''_{eff}}{\sqrt{\epsilon'_{eff}}} \\
\epsilon''_{eff} &= \frac{\kappa_e \sqrt{\epsilon'_{eff}}}{k_0}
\end{aligned} \tag{4.27}$$

where ϵ'_{eff} and ϵ''_{eff} are the real and imaginary parts of the effective dielectric constant, respectively.

4.4 Results

In this section we present results from Monte Carlo simulations. Section 4.4.1 discusses the nature of the phase matrix obtained from simulation and section 4.4.2 gives some physical understanding of the source of the observed depolarization. Section 4.4.3 presents the effective permittivity of the random media and comparisons with Clausius-Mossoti and QCA-CP. Section 4.4.4 presents the backscatter from a layer of snow and comparisons of results of independent scattering, DMRT, and Monte Carlo simulations.

4.4.1 Phase Matrix from Monte Carlo Simulations

The phase matrix was calculated as given in section 4.2.1 for spheres with $ka = 0.2$, permittivity $\epsilon_s = 3.2\epsilon_0$, and fractional volume of 35%. Values for the scattering coefficients can be found in table 4.1. The independent scattering assumption grossly overestimates the scattering at this fractional volume. QCA-CP predicts scattering rates that are 30% lower than those calculated with Monte Carlo simulations. This discrepancy could be due to the low frequency solution to QCA-CP.

Table 4.1: Scattering Coefficient for spheres with $a = 0.56$ mm. at 35% fractional volume and $\epsilon_s = 3.2\epsilon_0$

$\kappa_s (\times 10^{-3} \text{ 1/cm.})$						
Independent	QCA	QCA-CP	Monte Carlo			
				$\tau = 0.20$	$\tau = 0.05$	$\tau = 0.01$
3.36	0.23	0.38	0.54	0.87	1.17	9.38

The elements of upper corner of the phase matrix (i.e., $|\mathcal{F}_{11}|^2$, $|\mathcal{F}_{21}|^2$, $|\mathcal{F}_{12}|^2$, $|\mathcal{F}_{22}|^2$) are shown in figures 4.4 and 4.5 as functions of Θ . In the figures the solid line corresponds to non-sticky particles and the dash-dot line is for particles deposited in the test volume with a adhesive potential of $\tau = 0.05$. The open circles are the Rayleigh phase matrix elements where the scattering coefficient is computed with the independent scattering assumption. Depolarization from spheroids with an axial ratio of $c/a = 1.70$ are shown as plus signs in figure 4.5.

Several characteristics of the Monte Carlo phase matrix can be immediately noticed. The copolarized intensities ($|\mathcal{F}_{11}|^2$ and $|\mathcal{F}_{22}|^2$) have the same angular dependency as the Rayleigh matrix but the overall intensity is lower due to the more realistic scattering coefficient. As discussed in [100], the sticky particles have scattering levels that are much greater than the non-sticky particles due to the effectively larger particle size. For spherical particles the off diagonal terms ($|\mathcal{F}_{12}|^2$ and $|\mathcal{F}_{21}|^2$) of the Rayleigh matrix are zero. Monte Carlo simulations of both sticky and non-sticky particles give non-zero depolarized intensities that are approximately two orders of magnitude lower than the copolarized intensities. The level of depolarization calculated in the Monte Carlo simulations for the non-sticky spheres is comparable to the depolarization resulting from spheroids with axial ratios of 1.70.

Figures 4.6 and 4.7 are plots of the depolarization to copolarization ratios($\int_{\Theta} \sigma_{21} / \int_{\Theta} \sigma_{11}$ and $\int_{\Theta} \sigma_{12} / \int_{\Theta} \sigma_{22}$) as a function of permittivity and fractional volume, respectively. The ratio is larger for parallel polarization due to the lack of copolarized energy as Θ approaches $\pi/2$.

4.4.2 New De-polarization vs. Classical

For a single sphere in the presence of plane wave excitation, the dipole moment within the sphere is exactly aligned with the incident polarization and the scattered field in the scattering plane will not undergo any depolarization. Since in classical radiative transfer theory the phase matrix depends only on single particle scattering quantities, the phase matrix contains zero depolarization components in the plane of incidence. The reason for this thinking was the belief that the effect of any small misalignment of a sphere's internal dipole (relative to the incident field) due to the presence of scattered fields from surrounding spheres will cancel. This cancelation is due to the random, isotropic nature of the relative locations of the spheres which causes a randomness in the perturbation of the dipole orientation. For the case of large enough number of spheres the net depolarization was thought to be zero.

A central assumption of this idea is that the wave will continue to add the dipole moments coherently over a large enough distance for this cancelation to occur. If the distance required is large in comparison to the electromagnetic wavelength, the wave will decorrelate and the dipole moments separated by wavelengths apart will not be added coherently. In other words, there is an intrinsic length scale over which coherent addition of dipole radiation is achieved by the electromagnetic wave. If there are enough random, isotropically positioned spheres within this length scale there will be no depolarization. If however only a few hundred spheres are encountered before the wave decorrelates then the cross-dipole moment will not be zero. If we define the length scale for the correlated addition of dipoles as λ_{eff} , then the number of spheres contained within a volume λ_{eff}^3 must be large for the cross-dipole to go to zero.

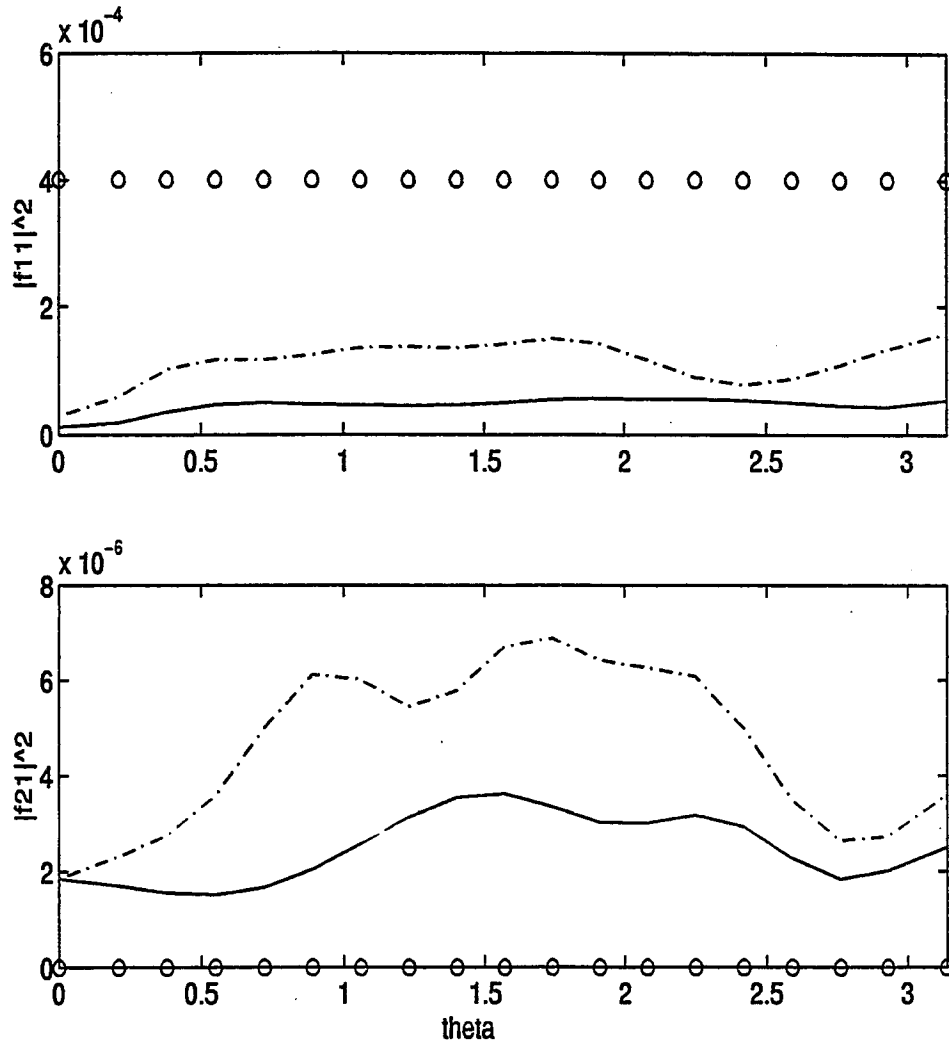


Figure 4.4: Elements of the phase matrix for an incident wave polarized perpendicular to the plane of incidence as a function of Θ . Results for spheres with $\epsilon_s = 3.2\epsilon_0$, 35% fractional volume and $a = 0.6$ mm. at 16 GHz. Monte Carlo results shown for non-sticky spheres (solid line) and sticky spheres with $\tau = 0.05$ (dash-dot line). Independent scattering shown as open circles.

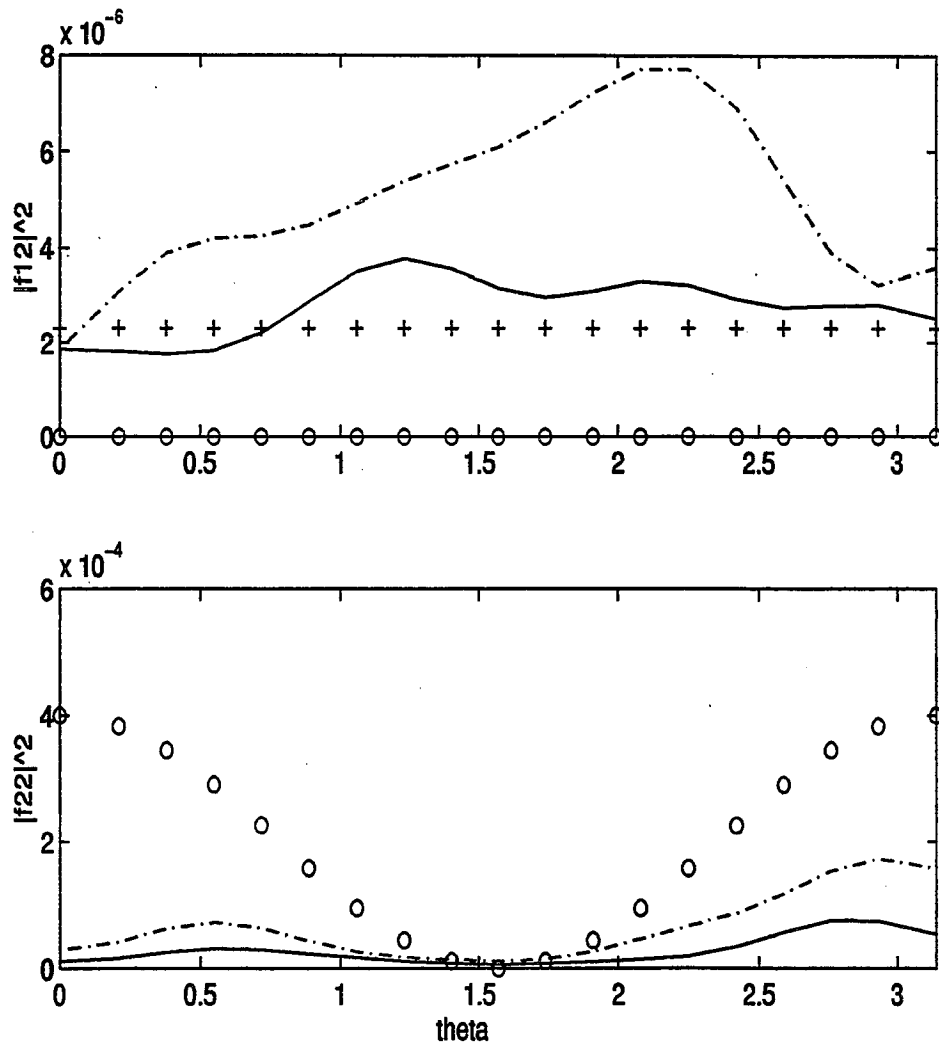


Figure 4.5: Elements of the phase matrix for an incident wave polarized parallel to the plane of incidence as a function of Θ ; parameter values the same as the previous figure. Monte Carlo results shown for non-sticky spheres (solid line) and sticky spheres with $\tau = 0.05$ (dash-dot line). Independent scattering shown as open circles and spheroids with $c/a = 1.70$ shown as plus signs.

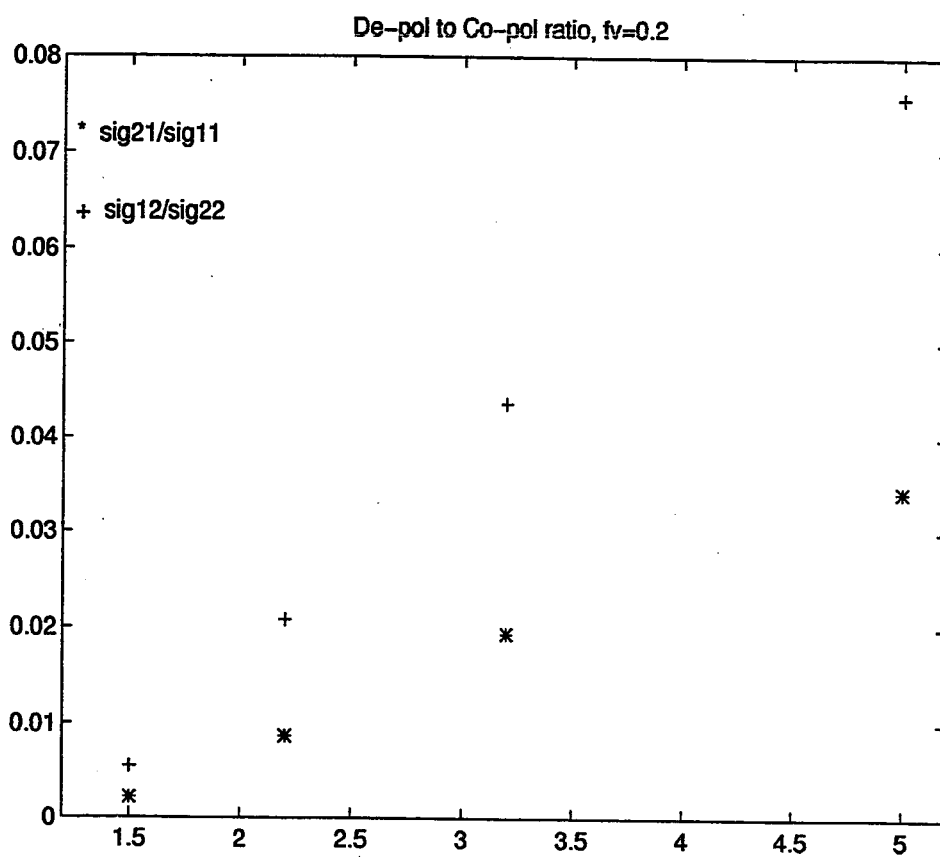


Figure 4.6: Depolarization level σ_{21}/σ_{11} (asterisk) and σ_{12}/σ_{22} (plus) as a function of the spheres' relative permittivity ϵ_s/ϵ_0 .

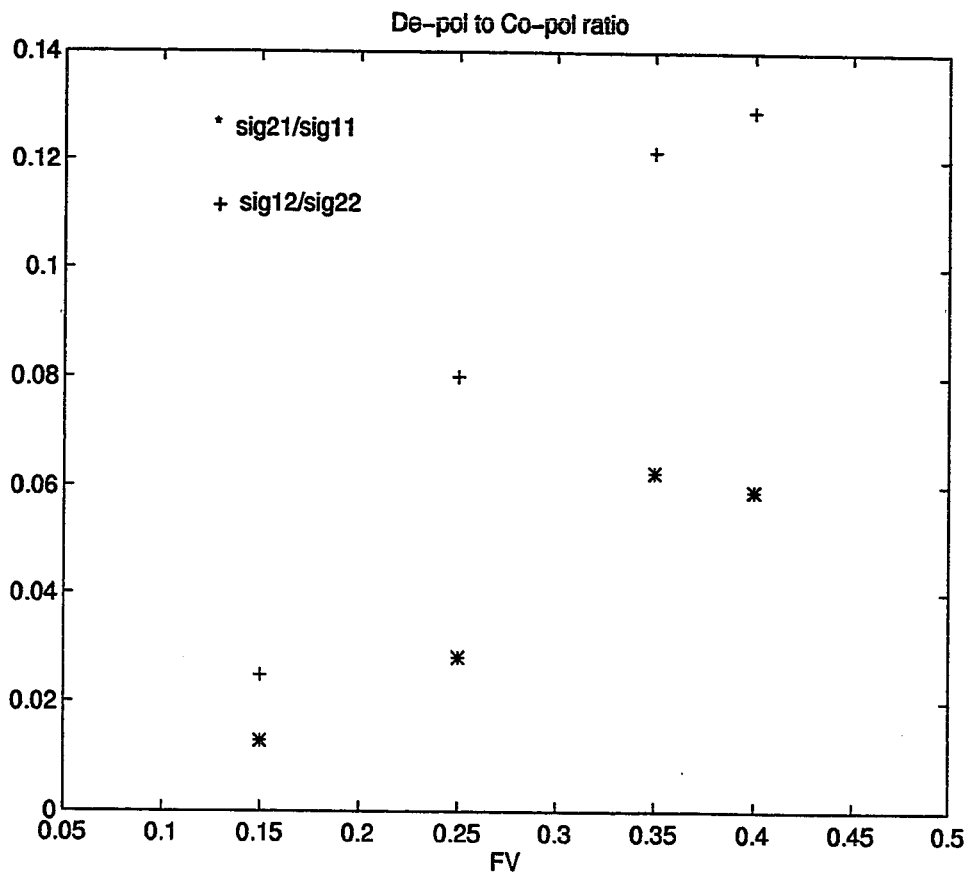


Figure 4.7: Depolarization level σ_{21}/σ_{11} (asterisk) and σ_{12}/σ_{22} (plus) as a function of fractional volume.

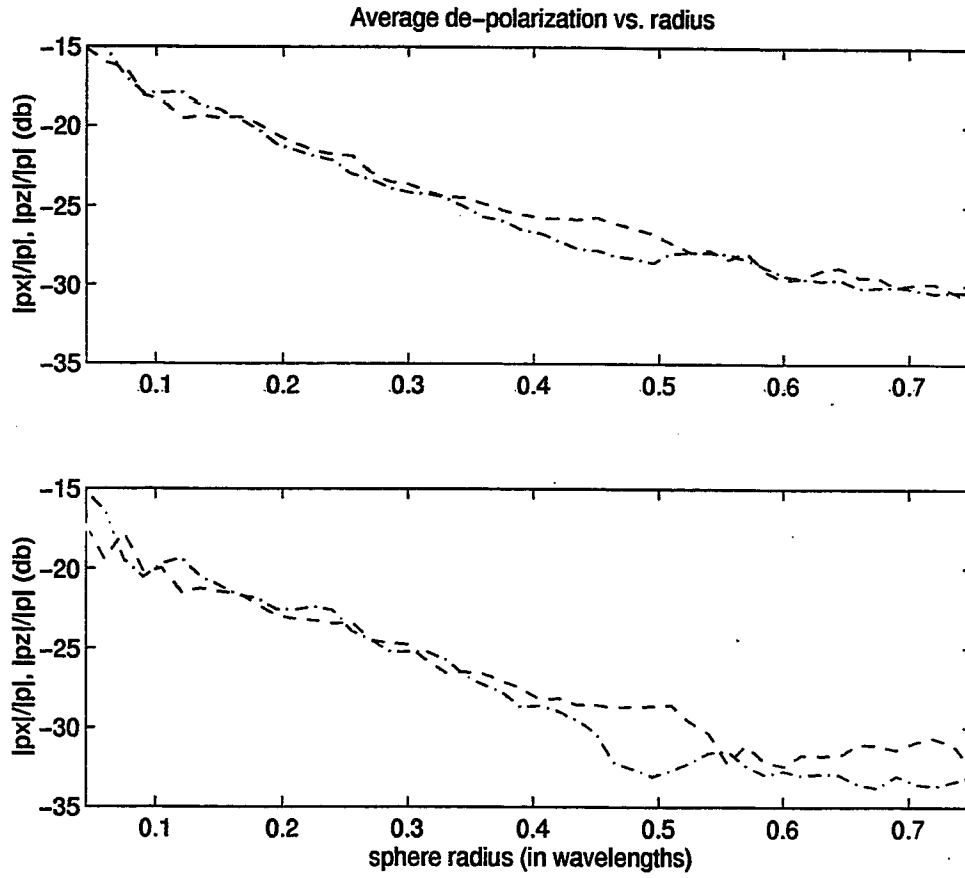


Figure 4.8: Magnitude of the x (dot-dash line) and z (dashed line) components of the internal dipole normalized to $|p_y|$ and computed as specified in equation 4.25. Results shown for 20% fractional volume with 2500 spheres for $\epsilon_s = 3.2\epsilon_0$ (top) and $\epsilon_s = 2.2\epsilon_0$ (bottom). The x axis is the radius a_l/λ_0 of the spherical volume over which the sum is computed.

In attempt to quantify the concept of a length scale for the electromagnetic wave, we used equation 4.25 to calculate explicitly the orientation of the internal electric dipole for 2500 spheres with fractional volume of 20%, and permittivities of $3.2 \epsilon_0$ and $2.2 \epsilon_0$. The magnitude of p_x and p_z relative to $|\overline{p_{sum}}|$ (i.e., those components misaligned with the incident y polarization) for $\epsilon_s = 3.2\epsilon_0$ is shown in a log scale as a function of α_l/λ_0 in the top of figure 4.8. The figure shows that the level of the depolarization decreases as more and more spheres are introduced into the sum in equation 4.25. The resultant net depolarization from the Monte Carlo simulations of -17 db in the phase matrix implies that the electromagnetic wave only adds coherently within the spherical region of diameter $d_l = 2 * \alpha_l = 0.27\lambda_0$. For a permittivity of $2.2 \epsilon_0$ (shown in the bottom of figure 4.8) the depolarization drops more quickly due to the diminished influence of the scattered fields relative to the incident excitation. The depolarization from the simulations corresponds to coherent addition within a distance of $d_l = 0.36\lambda_0$. The effective wavelengths for $\epsilon_s = 3.2\epsilon_0$ and $\epsilon_s = 2.2\epsilon_0$ are $\lambda_{eff} = 0.88\lambda_0$ and $\lambda_{eff} = 0.92\lambda_0$, respectively, where the effective media calculation is described in the next section. These distances indicate that the electromagnetic wave adds the dipoles coherently over roughly a quarter of an effective wavelength. Any existing depolarization within $\sim \frac{1}{4}\lambda_{eff}$ will be added coherently and incoherently outside that distance. This concept has important relevance to the distance scale over which coherent averaging is to be performed.

4.4.3 *Effective Media Calculations*

As outlined in section 4.3.2, the coherent scattering from the Monte Carlo volume can be used to calculate the effective permittivity of a collection of particles within the volume. This calculation was tested by comparing the coherent field scattering pattern as a function of angle from cubes of lengths $s = 1.27$, $s = 1.39$, and $s = 1.50$ containing 3000, 4000 and 5000 spheres of permittivity $\epsilon = 3.2\epsilon_0$, respectively, at 20% fractional volume. Since the size of the Monte Carlo volume varied, the coherent scattering pattern did as well. Scattering from the three cubes was then calculated with the Born approximation and an effective permittivity with the real part ranging between $\epsilon_{eff} = 1.1$ and $\epsilon_{eff} = 1.35$. For all three sized cubes, at an effective permittivity of $\epsilon_{eff} = 1.27$ the magnitude of the forward scattering peak and the fine structure of the sidelobes agreed well with that obtained from the Monte Carlo simulations. For higher fractional volumes a spherical test volume was used for the Monte Carlo simulations and the coherent scattering was calculated exactly from the Mie scattering. Figure 4.9 shows the real part of the effective permittivity as a function of fractional volume. Also shown is the permittivity calculated from the Clausius-Mossotti mixing formula and the quasi-crystalline approximation with coherent potential (QCA-CP). It is interesting to note that the Monte Carlo results agree quite well with those obtained from the mixing formula but are slightly below the values predicted by QCA-CP. In recent work [100] we showed that the extinction rates calculated from Monte Carlo simulations agreed with those produced from QCA-CP, but were higher than those produced from QCA.

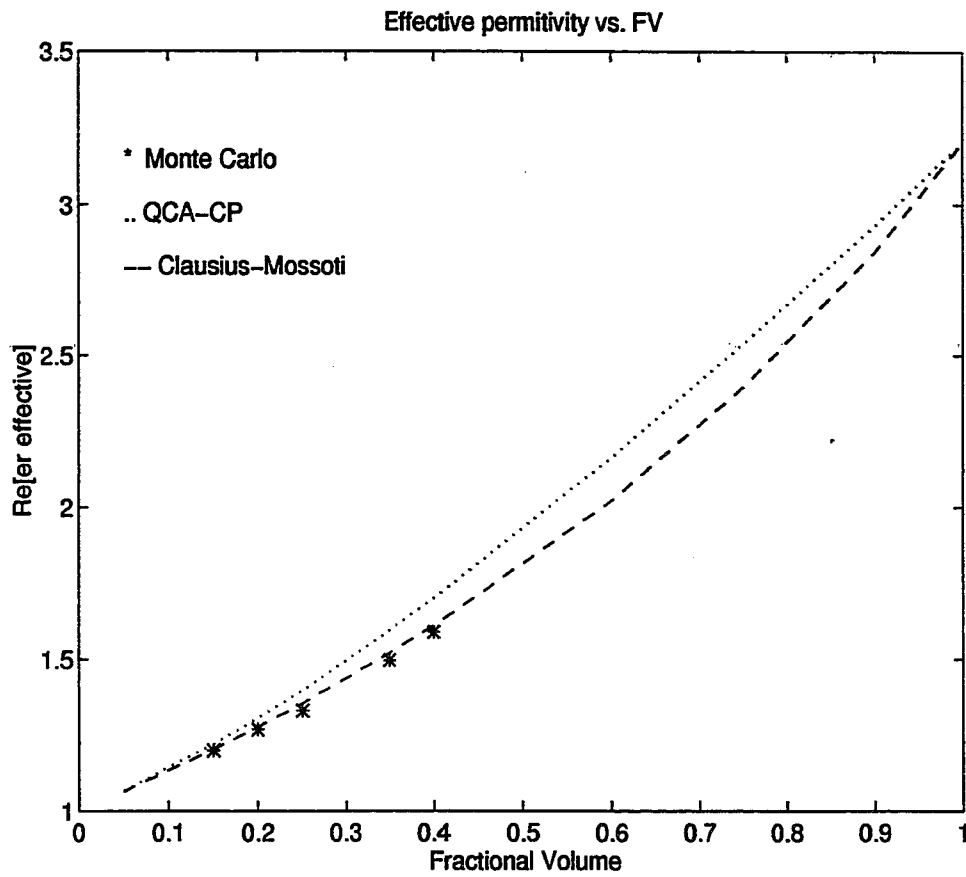


Figure 4.9: Real part of the effective permittivity ϵ_{eff} vs. fractional volume calculated from Monte Carlo simulations (shown as asterisk) and compared with Clausius Mossotti (dashed line) and QCA-CP (dotted line).

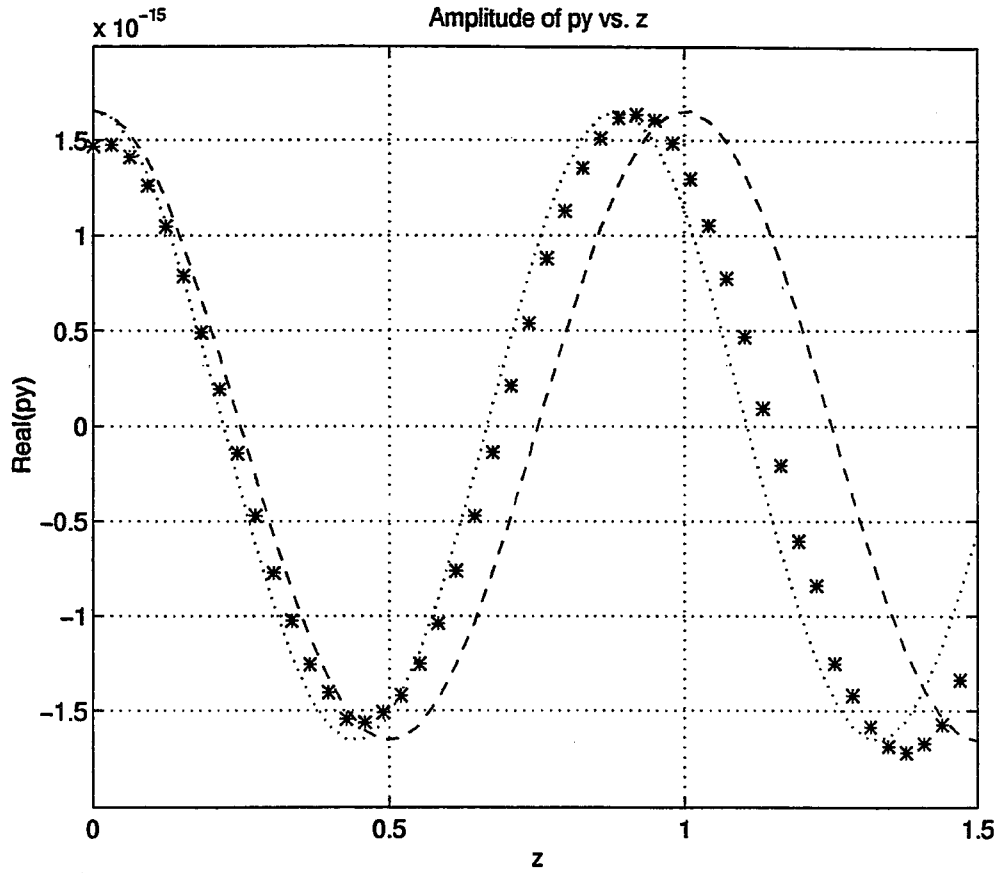


Figure 4.10: $Re(p_y)$ vs. z/λ_0 where p_y is the averaged over constant z planes. Monte Carlo results (asterisk) shown for 20% fractional volume with 5000 spheres with $\epsilon_s = 3.2\epsilon_0$ in a cubic test volume. Also shown is $\cos(K_r z)$ for $K_r = k_0 \sqrt{1.27}$ (dotted line) and $K_r = k_0$ (dashed line).

An alternate method of obtaining the real part of the effective permittivity is to plot $Re\{p_y\}$ as a function of z . The coherent plane wave travels in the z direction through the Monte Carlo cubic volume with a phase determined by $e^{-iK_r z_j}$. This excites a dipole moment polarized in the y direction whose amplitude traces out a cosine curve with a wavelength of $\lambda_{eff} = \lambda_0/\sqrt{\epsilon_{eff}}$. The asterisk in figure 4.10 represent the average of $Re\{p_y\}$ computed along planes orthogonal to the z direction (i.e., x - y planes) for spheres at 35% fractional volume and with $\epsilon = 3.2\epsilon_0$. The dipole oscillation as predicted by the QCA approximation in equation 4.23 is shown as a dotted line for $\epsilon_{eff} = 1.27$ and as a dashed line for free space propagation with $\epsilon_{eff} = 1.00$. The internal dipoles in the Monte Carlo simulation follow closely those predicted by the effective permittivity calculation. There are slight discrepancies close to the ends of the volume (at $z = 0$ and $z = 1.5\lambda_0$ planes) since these planes are not completely embedded in the effective medium.

4.4.4 Active Remote Sensing from a Layer of Snow

The radiative transfer (RT) model can be applied to determine the effect of volume scattering within a layer of discrete spherical scatterers overlying a homogeneous half-space. The results depend on the method in which the scattering coefficient, the phase matrix, and effective permittivity are determined. In this section we present the results from the classical model, DMRT model, and Monte Carlo model. All three models are applied to the geometry shown in fig 4.1 where the bottom layer has a permittivity of $\epsilon_2 = (6.0 + i0.6)\epsilon_0$, a typical value for soil. Region 1 is composed of scatterers with $\epsilon_s = 3.2\epsilon_0$ in a background of air $\epsilon_1 = \epsilon_0$. The scatterers occupy 35% by volume and have a radius of 0.6 mm. at 16 GHz.

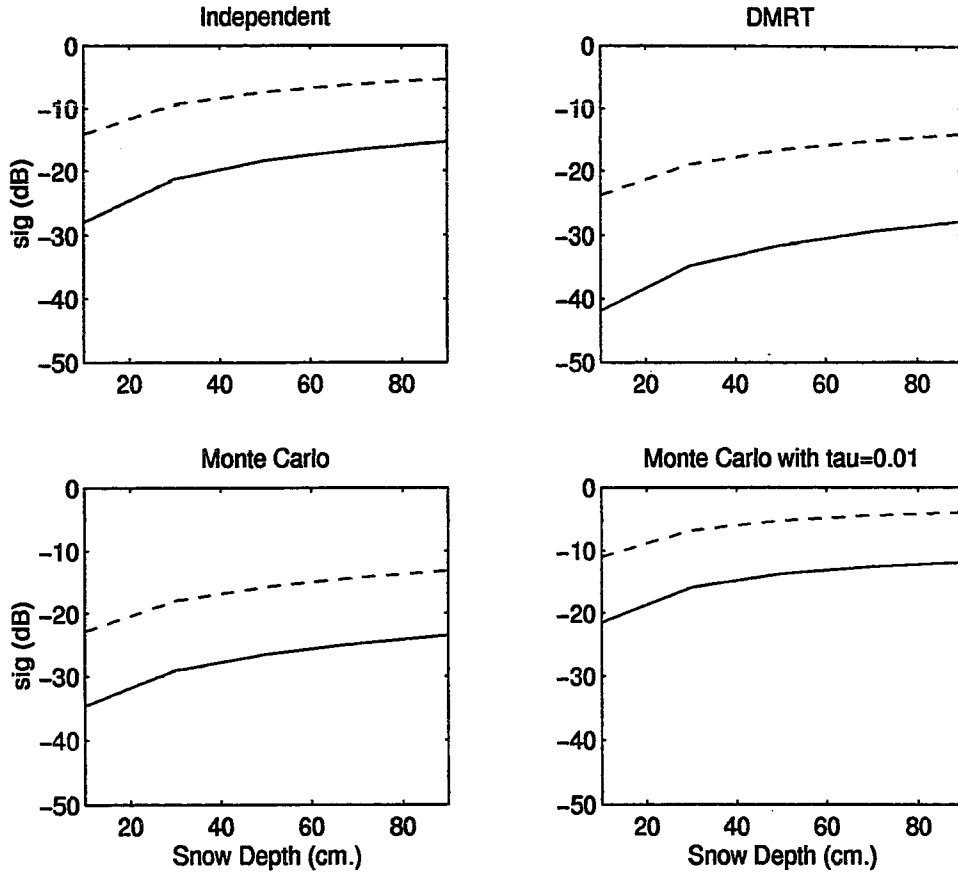


Figure 4.11: Backscattering as a function of snow depth for 16 GHz at $\theta_i = 19.31^\circ$ from a layer of snow with $a = 0.6$ mm., $\epsilon_s = 3.2\epsilon_0$ and 35% fractional volume. The dashed line is σ_{vv} and solid line is σ_{hv} . The four plots show results of the radiative transfer theory for the classical model (top left), DMRT model (top right), Monte Carlo simulations (bottom row) and sticky particles with $\tau = 0.01$ (bottom right).

Figure 4.11 shows the backscattering cross section as a function of snow thickness d for an incident angle of 19.31° as calculated with the three models. In the figure, the copolarized backscatter σ_{vv} is shown as a dashed line and the depolarized σ_{hv} backscatter as a solid line. Results from the classical model (top left) have very high copolarized and depolarized levels due to the overestimation of the scattering coefficient from the independent scattering assumption. For the depolarized backscatter, the first order RT solution is zero when the Rayleigh phase matrix is used. The second order solution is non-zero with $|\sigma_{hv}^{(2)}| \sim \kappa_s^2 d^2$. Thus in top left and right plots the copolarized backscatter is a first order effect and the depolarization is second order. For scatterers at 35% by volume, DMRT predicts a more reasonable estimate of the scattering coefficient and gives a copolarized level that is 10 dB. down and a depolarized level that is 13 dB. down relative to the classical model.

The backscattering cross sections from the Monte Carlo model are shown in the bottom two plots. For the non-sticky case (lower left) the extinction coefficient calculated from the Monte Carlo simulations is not significantly larger than κ_s^{DMRT} and the level of the copolarized return is comparable to that from the DMRT model. However, the depolarized backscatter is much greater, particularly at small snow depths such as 10 cm. where it is more than double that predicted by DMRT. This is because the phase matrix from the Monte Carlo simulations has non-zero off-diagonal terms and thus the depolarization has non-zero first order as well as second order contributions. The first order contribution is linearly dependent on d and will therefore be greatest in comparison to the second order when the snow depths are small.

In bottom right plot the backscattering cross sections from the Monte Carlo model are shown when the particles were deposited with a sticking potential of $\tau = 0.01$. This scenario could represent snow that has been on the ground long enough for metamorphic forces to cause the grains to become rounded, cluster together, and bond. The effects of this clumping are to increase the effective particle size and thus increase the scattering coefficient to a value approximately three times as large as that predicted under the independent scattering assumption for non-sticky particles [100]. Both the copolarized and depolarized backscattering from a layer of clustered snow grains are higher than that calculated under the classical model for non-sticky particles. For these very sticky particles the level of the depolarized backscatter is due mainly to the second order contributions.

The bistatic cross sections computed using the Monte Carlo model shows even greater increases in depolarization relative to conventional theory. Figure 4.12 shows the bistatic scattering at $\theta_s = 59^\circ$ for spheres with $\tau = 0.2$ and the same parameters as the previous plots. The first order copolarized return is shown as a dotted line, the first order depolarization is shown as a dashed line, and the second order depolarization is shown as a dash-dot line. The first order depolarization, which would be zero under conventional theory, is 7 dB. higher than the second order at shallow snow depths, and reaches -22 db at depths of 90 cm.

The increased extinction predicted from sticky particles can be used to explain the higher levels seen in backscattering data. Results from Monte Carlo simulations of sticky particles are compared with active microwave measurements made on December 16, 1979 at a test site in Colorado [72]. Figure 4.13 shows the backscattering at 17 GHz for a 47.5 cm. layer of snow with grain radius of $a = 0.56$ mm. and fractional volume of 20% as a function of incidence angle. The copolarized backscatter (shown as a dotted line) and the depolarized backscatter (shown as a solid line) were computed using the extinction coefficient and phase matrix for spheres with $\tau = 0.1$.

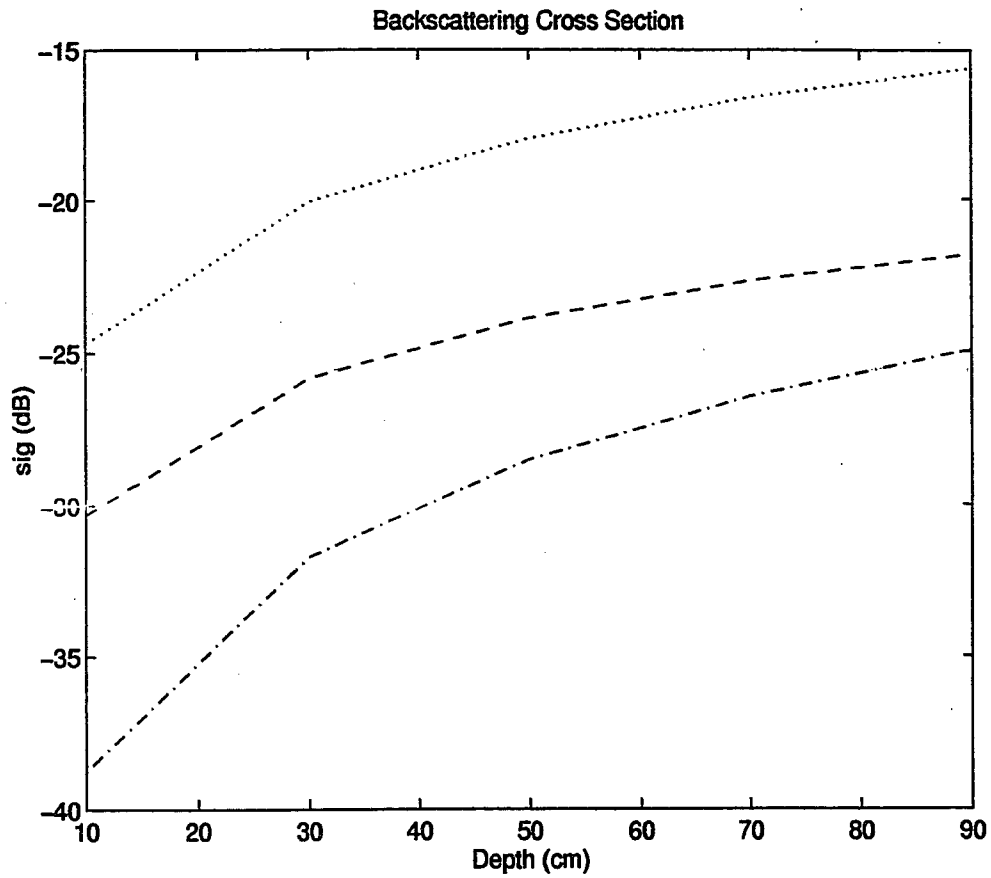


Figure 4.12: Bistatic cross sections for the same parameters as in the previous plot except $\theta_s = 59^\circ$ and $\tau = 0.20$. The first order copolarized return is shown as a dotted line, the first order depolarization is shown as a dashed line, and the second order depolarization is shown as a dash-dot line.

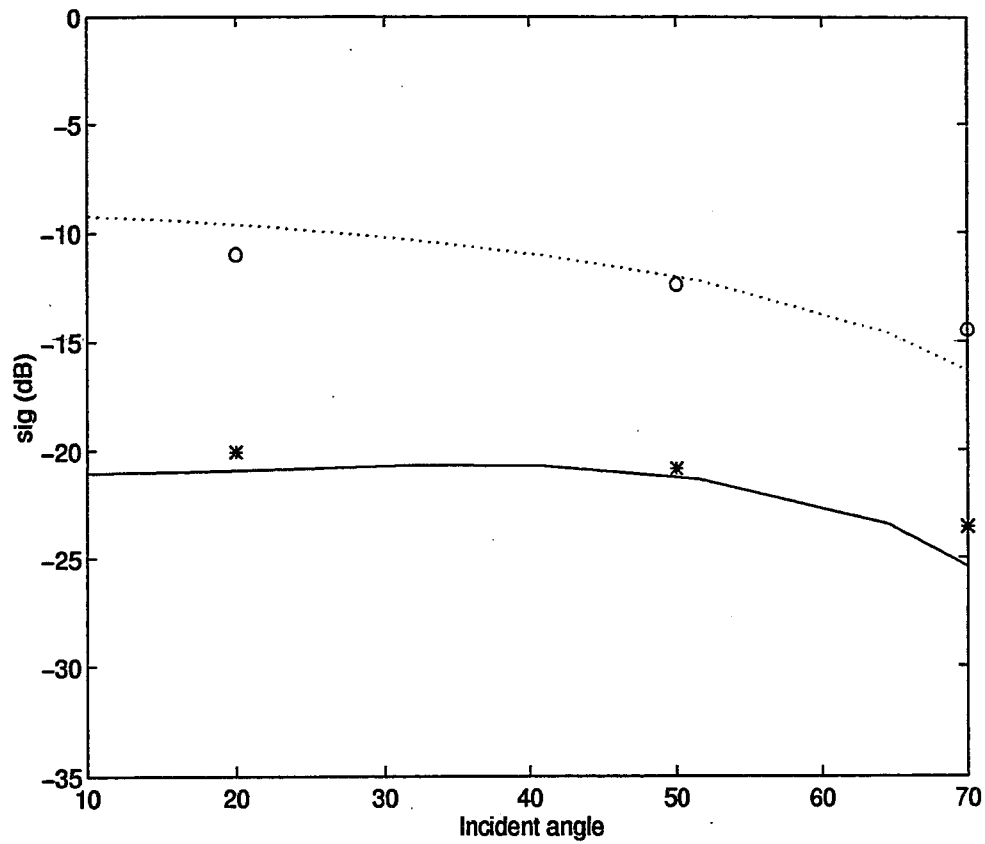


Figure 4.13: Backscattering cross section for 17 GHz compared with data for a 47.5 cm. deep snow cover with grain radius $a = 0.56$ mm and fractional volume $fv = 0.2$. Data shown as circles (co-pol) and asterisks (de-pol); RT model with sticky spheres $\tau = 0.1$ shown as a dotted line (co-pol) and solid line (de-pol).

4.5 Discussion and Conclusions

The Monte Carlo simulations provide a valuable tool for testing our understanding of electromagnetic wave propagation through dense media. The simulations take into account correlated scattering and coherent wave interaction. The coherent and incoherent fields distributions can be used to calculate the extinction coefficient, phase matrix, and effective permittivity of the discrete random medium. These quantities are necessary for solution of the radiative transfer equation. The extinction coefficient from Monte Carlo simulations is significantly lower than that predicted by independent scattering, but is comparable with QCA-CP.

The co-polarized elements of the phase matrix from the Monte Carlo simulations agrees with that obtained from DMRT. However, the off-diagonal elements are non-zero but are two orders of magnitude smaller than the copolarized energy. The presence of this depolarization is due to the random organization of the spheres which can give rise to perturbations in the internal dipole alignment. For very low frequencies, the random, isotropic arrangement of spheres causes cancellation of these deviations. For higher frequencies, since the wave will only add the dipole moments coherently over scales on the order of $\frac{1}{4}$ of a wavelength, the depolarization in the scattered field will remain.

Application of a radiative transfer model can yield different results depending on the assumptions used in calculation of the extinction coefficient, phase matrix, and effective permittivity. The independent scattering assumption gives overly high levels of backscatter due to overestimation of scattering. DMRT gives more realistic scattering coefficients, but neglects the first order depolarization effect. First order depolarization arises from coherent near field interaction among the spheres that creates

non-alignment of dipole moments. Using the phase matrix and scattering coefficient obtained from Monte Carlo simulations can produce co-polarized backscattering that is comparable to QCA-CP but also much higher levels of depolarized backscatter due to non-zero contributions from both first and second order effects. This combination results in a different snow depth and frequency dependence than indicated by conventional theory. Large increases in both copolarized and depolarized backscatter can be achieved by including the clustered nature of metamorphosed snow with a sticky particle model.

The effective permittivity of snow can be derived from the results of Monte Carlo simulations. The imaginary part of the effective wavenumber is related to the extinction coefficient for the incoherent wave and the real part corresponds to the phase progression of the coherent wave. The phase information is available both in the coherent scattering from the Monte Carlo volume as well as the oscillation of the internal dipole within the scatterers. The effective permittivity obtained from simulation yields an imaginary part that is in agreement with that predicted by QCA-CP. The real part of the permittivity agrees with that obtained from mixing formulas such as Clausius-Mossotti formula but is slightly lower than that predicted from QCA-CP.

Chapter 5

PAIR FUNCTION RETRIEVAL FROM PLANAR SNOW SECTIONS

Electromagnetic wave scattering in dense media, such as snow, depends on the 3-D pair distribution function of particle positions. In snow, 2-D stereological data can be obtained by analyzing planar sections. In this chapter we calculate the volume 3-D pair distribution functions from the 2-D stereological data by solving Hanisch's integral equation. We first use Monte Carlo simulations for multi-size particles to verify the procedure. Next we apply the procedure to available planar snow sections. A log-normal distribution of particle sizes is assumed for the ice grains in snow. To derive multi-size pair functions, a least squares fit is used to recover pair functions for particles with sufficient number density and the hole correction approximation is assumed for the larger particles. A family of 3-D pair distribution functions are derived which give scattering rates comparable to those calculated under the Percus-Yevick approximation of pair distribution functions of multiple sizes.

5.1 *Introduction*

Snow is a dense medium because the ice grain that comprise snow are densely packed. The classical approach for random discrete scatterers is the independent scattering approximation which states that the collective scattering of the system is equal to the scattering from each individual particle multiplied by the number of particles in the system. For dense systems (particles occupy more than a few percent by volume) this approximation is not valid because the correlation of the particles' positions affects

the scattering physics. This has been shown experimentally [39, 44] and theoretically. To account for the correlation between particles, analytic dense media theory such as the quasicrystalline approximation (QCA) and quasicrystalline approximation with coherent potential (QCA-CP) [81] has been assumed for the first moment of the field. The extinction coefficients are in good agreement with controlled laboratory experiments [52, 98, 99]. Both QCA and QCA-CP rely on a bi-variate statistic called the pair distribution function to describe the particle positions. The Percus-Yevick [60] (PY) pair distribution function from molecular physics has been used extensively to model impenetrable spheres. For the application of scattering from snow it is desirable to derive the pair distribution functions directly from snow samples.

In addition to analytic theory such as QCA-CP, Monte Carlo simulations have been used to calculate the extinction coefficient, phase matrix, and absorption coefficient of a volume of up to 5000 spheres [85] - [102] and these quantities used in radiative transfer theory to calculate bistatic scattering properties. The extinction rates derived from the simulations in which spheres are randomly deposited are in excellent agreement with QCA-CP with PY. Snow is a naturally occurring geophysical dense medium in which metamorphic processes can yield clusters or aggregations of ice grains. The ice crystals lose their original atmospheric form, reducing their surface-area-to-volume ratio by forming larger, more rounded shapes. Deposited snow increases in density as the grains grow and form "necks" with neighboring particles. Much research has been done to understand the sintering process [43, 37, 16] and to model scattering in clustered systems [25].

In this chapter we quantitatively utilize snow data to devise a more realistic pair function. Stereological methods provide a quantitative description of the snow organization and researchers in the snow community are experimenting with stereological tools [90] to attempt to quantify the microstructure of snow. The relationship between the area pair distribution function and the volume pair distribution function can be expressed in the form of Hanisch's integral equation [34] which is presented in section 5.2. It is possible to solve Hanisch's integral equation to obtain a 3D volume pair distribution function for 2D pair functions if the size distribution is known. We follow Shi et. al. [70] and assume a log-normal size distribution. Measurements obtained from 2-D subsections of snow allow us to invert the equation and recover the total volume pair distribution function. To calculate scattering for multi-size spheres the total volume pair distribution function is then decomposed into a family of functions related to each of the sizes present. In section 5.3.1 we describe a non-linear least squares fit combined with a set of physically meaningful rules that allows us to accomplish this decomposition.

The recovery of the pair distributions functions is tested first in the controlled computer environment of Monte Carlo simulations. Results obtained for the simulations are described followed by the results from snow data in section 5.6.

5.2 Volume Pair Distribution Function from Section Data

Quantitative stereology attempts to characterize numerically the geometrical aspects of those features of the microstructure which are of interest. A considerable number of research efforts in the stereological community deal with the problem of determining properties of particles from their 2-D or 1-D cross-sections. A detailed discussion of stereological theory is given in Underwood [90].

The volume pair distribution function, g_v , is defined by Hanisch as

$$g_v(r) = \frac{1}{4\pi r^2} \frac{dK_v(r)}{dr} \quad (5.1)$$

where $N_v K_v(r)$ can be interpreted as the mean number of particles in a sphere with radius r centered at an arbitrary point and N_v is the mean number of spheres per unit volume. For a single particle size, $g_v(r)$ is the same as the pair distribution function used in dense media theory to calculate scattering. Likewise, g_A is the area pair distribution function measurable from section data,

$$g_A(r) = \frac{1}{2\pi r} \frac{dK_A(r)}{dr}, \quad (5.2)$$

with $N_A K_A(r)$ the mean number of particles in a circle with radius r and N_A is the mean number of circles per unit area.

In the case where the particles are spherical in shape and their size distribution is known an integral equation due to Hanisch can be developed from probability expressions which relates the pair distribution function to parameters that can be obtained from a section of thickness $2t$ [34]:

$$g_A(r) = \frac{1}{4(E[\xi_n] + t)^2} \int_0^\infty f(u, t) g_v(\sqrt{r^2 + u^2}) du \quad (5.3)$$

where $E[\xi_n] = r_0$ is the mean radius of the ice grains and $f(u, t)$ for a section with thickness $t = 0$ can be calculated from the cumulative distribution function R_v for the sphere radii as

$$f(u, t = 0) = 2 \int_0^\infty [1 - R_v(|v - u|/2)] [1 - R_v((u + v)/2)] dv. \quad (5.4)$$

5.2.1 Calculation of g_A

A measure of g_A can be computed by counting the occurrence of separation distances between the centers of the intersection circles. If the frequency estimate for a separation r , $r_i - \delta/2 < r < r_i + \delta/2$ is defined as $w(r_i)$ then g_A is given by

$$g_A(r_i) = \frac{w(r_i)}{N_A \pi (r_{i+1}^2 - r_i^2) (N_c - 1)} \quad (5.5)$$

where N_c is the total number of circles appearing on the sections. The factor $\pi(r_{i+1}^2 - r_i^2)$ appearing in the denominator accounts for the finite area in the circular shell over which the counting is done.

The accuracy with which g_A can be estimated depends on the number and size of the available sections, the density of those sections, and the number of frequency bins considered. The first two of these factors is limited by the amount and nature of the section data and might not be adjustable. However, the specification of the sampling size is. As the size of the discrete separations δ increases, the number of pairs of circles that contribute to this bin also increase. This additional averaging can give a smoother estimate of g_A as long as δ is not so large that the underlying g_A is changing appreciably within range. If it is not, the smoother estimate of g_A is more desirable since inversion of (5.7) will propagate noise to the recovered g_v .

The crucial region of g_A is close range. For a multi-size system of spheres, this region is approximately between zero and two times the average particle size (the exact extent will vary depending on the size distribution). As larger and larger separation distances are considered, g_A will approach one, which signifies an absence in correlation between circle centers.

The actual volume pair distribution function g_v is calculated from the Monte Carlo data in a similar fashion as g_A but has a term in the denominator relating to the volume of the spherical shell instead of the area.

5.2.2 Solution of Hanisch's Equation

The integral in (5.3) can be inverted by employing point matching techniques [36]. To recover the volume pair distribution function over a linear spacing, first make a change of variables $x = \sqrt{r^2 + u^2}$ to obtain

$$g_A(r) = \frac{1}{4r_0^2} \int_r^\infty f(\sqrt{x^2 - r^2}, t = 0) \frac{x}{\sqrt{x^2 - r^2}} g_v(x) dx. \quad (5.6)$$

Then assume that over some small interval $x - \frac{\delta x}{2}, x + \frac{\delta x}{2}$ the function $g_v(x)$ remains sufficiently constant to obtain the matrix equation

$$g_A(r) = \frac{1}{4r_0^2} \sum_{x=0, x \geq r}^{x_{max}} g_v(x) I(x, r) \quad (5.7)$$

where

$$I(x, r) = \int_{u1}^{u2} f(u, t = 0) du \quad (5.8)$$

with integration limits

$$u1 = \begin{cases} \sqrt{(x - \frac{\delta x}{2})^2 - r^2} & (x - \frac{\delta x}{2})^2 > r^2 \\ 0 & \text{otherwise} \end{cases} \quad (5.9)$$

$$u2 = \sqrt{(x + \frac{\delta x}{2})^2 - r^2}. \quad (5.10)$$

The integral $I(x, r)$ in (5.7) can be computed analytically for some forms of Rv . For a single size sphere of radius r_0 it simplifies to

$$I(x, r) = (2r_0 - .5)(\min(u2, 2r_0) - u1) \quad (5.11)$$

$$(5.12)$$

It is also possible to compute $I(x, r)$ for a size distribution made of a small number of discrete sizes with known densities. For more complicated distributions it can be evaluated numerically.

The matrix equation (5.7) is upper triangular, and for large values of r it is strongly diagonal. The number of points necessary to get a good estimate of $g_v(r)$ is small since the particle positions become independent (and $g_v(r) \rightarrow 1$) within a few particle diameters.

5.2.3 Results from Simulation

Recovery of the pair distribution function g_v was tested using a computer generated system of $N=3500$ spheres of radius r_0 . The spheres were deposited using a Metropolis technique into a test cube so that they occupied 30% by volume and their positions were non-overlapping. The volume was cut by 17 section planes and $g_A(r)$ was calculated as described in section 5.2.1. The area pair distribution function $g_A(r)$ is shown normalized to r_0 in the right-hand plot of figure 5.1. Note that $g_A(r) \neq 0$ for $r < 2r_0$.

For single size spheres the integral $I(x, r)$ is given in (5.11) and (5.7) can be easily inverted to give $g_v(r)$. The resulting volume pair distribution function normalized to r_0 is shown as a solid line in the left-hand plot of figure 5.1. Also shown for comparison is g_v calculated from the simulation volume by a counting procedure (dashed line) and g_v calculated from the Percus-Yevick approximation (dotted line). The agreement between the three is quite good.

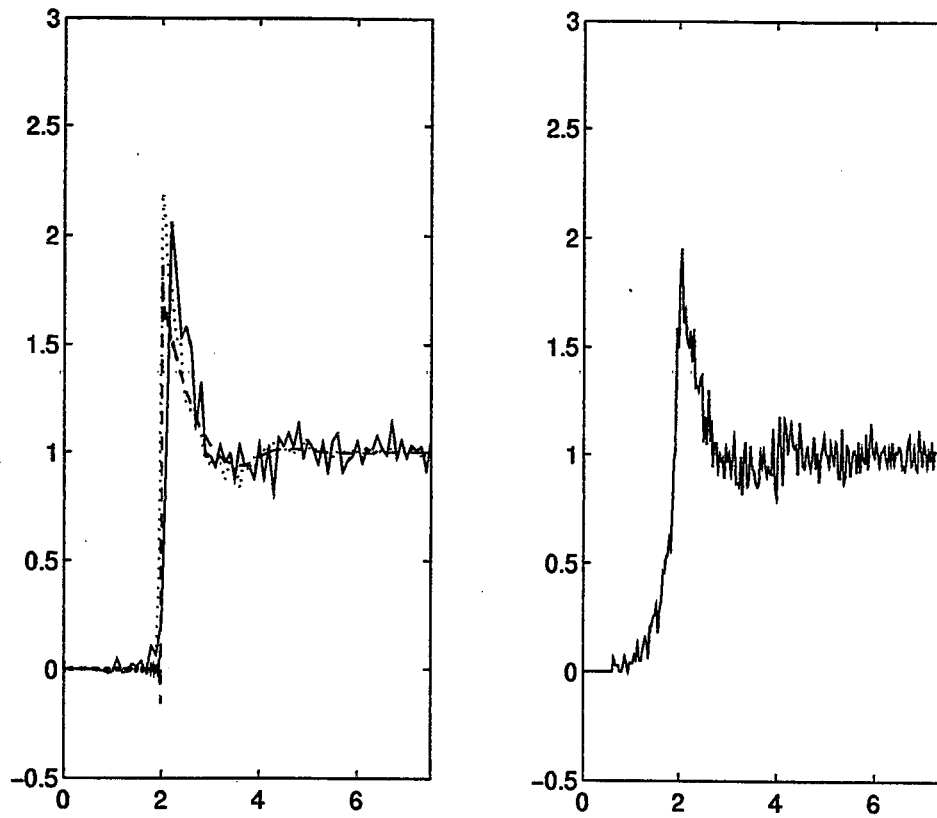


Figure 5.1: Left hand plot shows volume pair distribution function g_v normalized to r_0 recovered from computer simulation (solid line), calculated from Percus-Yevick (dotted line) and calculated from Monte Carlo volume (dashed line). Right-hand plot shows area pair distribution function g_A calculated from sections of computer simulation.

5.3 g_v and g_{ij}

The function g_v is the volume pair distribution function for all the particles in a system and can be obtained from section data as discussed in section 5.2. Of interest in a multi-size system the pair functions that describe the interaction between different size spheres. In a system of particles with L different species denoted by $s_j = 1, 2, \dots, L$ and number density n_{s_j} , $g_v(r)$ can be represented as a sum

$$g_v(r) = \sum_{i,j} \frac{n_{s_i} n_{s_j}}{n_0} g_{ij}(r) \quad (5.13)$$

where n_0 is the total particle density and $g_{ij}(r)$, $i, j = 1 \dots L$ is the pair distribution function for interaction between two particles of species s_i and s_j . Hanisch's integral equation allows recovery of g_v but does not provide information on the contributing $g_{ij}(r)$. From (5.13) we see that the contribution to $g_v(r)$ from a given $g_{ij}(r)$ is weighted by the number densities of species s_i and s_j . Thus species that occur in small numbers will have little effect on the function $g_v(r)$ and will be difficult to recover.

Under the Percus-Yevick approximation a closed form solution for $g_{ij}(r)$ exists which allows calculation of $g_v(r)$ from when the sizes and numbers densities of each species is specified.

5.3.1 Nonlinear Model Fit to get g_{ij} from g_v

The pair distribution function $g_v(r)$ can also be modeled as

$$g_v(r) = \sum_{k=1}^L X_k(r) \quad (5.14)$$

where $X_1(r), \dots, X_L(r)$ are basis functions. The maximum likelihood estimate of the model parameters is obtained by minimizing the chi-square quantity

$$\chi^2 = \sum_{i=1}^{N_d} \left[\frac{g_v(r_i) - \sum_{k=1}^L X_k(r_i)}{\sigma_i} \right]^2 \quad (5.15)$$

where $r_i = i\delta$ with $i = 1, 2, \dots, N_d$ and σ_i is the measurement error at that point. For snow section data we do not know the measurement error for g_v (this is equivalent to knowing error in estimating the unknown g_A) and (5.15) can thus serve only as a relative measure of fit.

Ideally, the L functions in (5.14) would correspond to the L individual pair functions g_{ij} in (5.13). Then the least squares fit for the unknown parameters of X_k would give a functional form for the g_{ij} . Characteristics of non-overlapping particles are :

- At values of r less than the sum of the two particles' radii the particles cannot overlap and the pair function is zero.
- In densely packed systems, two particles that are close together ($r \sim r_i + r_j$) have strong correlation resulting in a peak in their pair distribution function at that point.
- Densely packed systems have oscillatory pair functions.
- As r becomes large the particles' position becomes uncorrelated and the pair function approaches one.

From the above considerations a reasonable model can be chosen for $g_{ij}(r)$ of the form similar to that proposed by Verlet and Weis [93]

$$X_k(r) = h(r - r_k) \left[\frac{A_k}{r} \exp(-\mu_k(r - r_k)) \cos(\mu_k(r - r_k)) + 1 \right] \quad (5.16)$$

where the double index i, j has been collapsed into a single index k with

$$r_k \equiv r_i + r_j \quad (5.17)$$

and $h(r)$ is the step function given by

$$h(r) = \begin{cases} 0 & r < 0 \\ 1 & \text{otherwise} \end{cases} \quad (5.18)$$

Equation (5.16) contains two adjustable parameters A_k and μ_k , which represent the amplitude of the spike in the pair function as it “comes on”, and the strength of the decay and oscillation, respectively.

Minimization of (5.15) with respect to A_k and μ_k can be achieved through a steepest descent method. Since the form of the basis functions is known, both the first and second derivative w.r.t. the adjustable parameters are known, and the minimization of χ^2 can also utilize a Hessian matrix algorithm [63]. The Levenberg-Marquardt method combines these two strategies and is the standard nonlinear least-squares routine. The method entails choosing an initial guess for the fit parameters and then iterating until an error threshold is reached. Since the intent of the fit is not only to find a model fit for g_v but to find one in which the basis functions represent g_{ij} , choosing the initial parameters is important.

5.3.2 Snow Subsections

The 2-D subsections of snow were prepared by first saturating the pore void with filler, then cutting, polishing and enhancing the contrast so that the snow grain profiles can be automatically classified against the pore filler (formerly air) [59, 32, 27, 19]. Figure 5.2 shows a portion of a snow section from a site in Fairbanks, Alaska prepared at the Cold Regions Research Engineering Laboratory (CRREL) in Hanover, New Hampshire. The fractional volume of ice grains can be determined from the point density and is approximately 22 % for this section.

In this chapter we are assuming a spherical shape for the ice grains. For grains that are not perfect spheres, this approximation does not produce a large error if the grains are randomly aligned. The position and diameter of the ice profiles on the cross section indicate it is impossible to find a single representative sphere size for the snow. The diameters of snow grains has been observed to follow a log-normal distribution [17] which has been used to model snow sizes [70]. We will also assume a log-normal distribution but the choice of an alternate size distribution would simply alter the form of equation 5.4. The log-normal distribution for diameter d can be written as [57]

$$f(d) = \frac{1}{d \log \sigma_g \sqrt{2\pi}} \exp \left[-\frac{1}{2} \left(\frac{\log d - \log D_g}{\log \sigma_g} \right)^2 \right] \quad (5.19)$$

where D_g is the geometric mean and σ_g is the geometric standard deviation. These can be expressed in terms of the first, second and third moments of the intersection lengths, \bar{L} , \bar{L}^2 , and \bar{L}^3 , respectively, as [70]

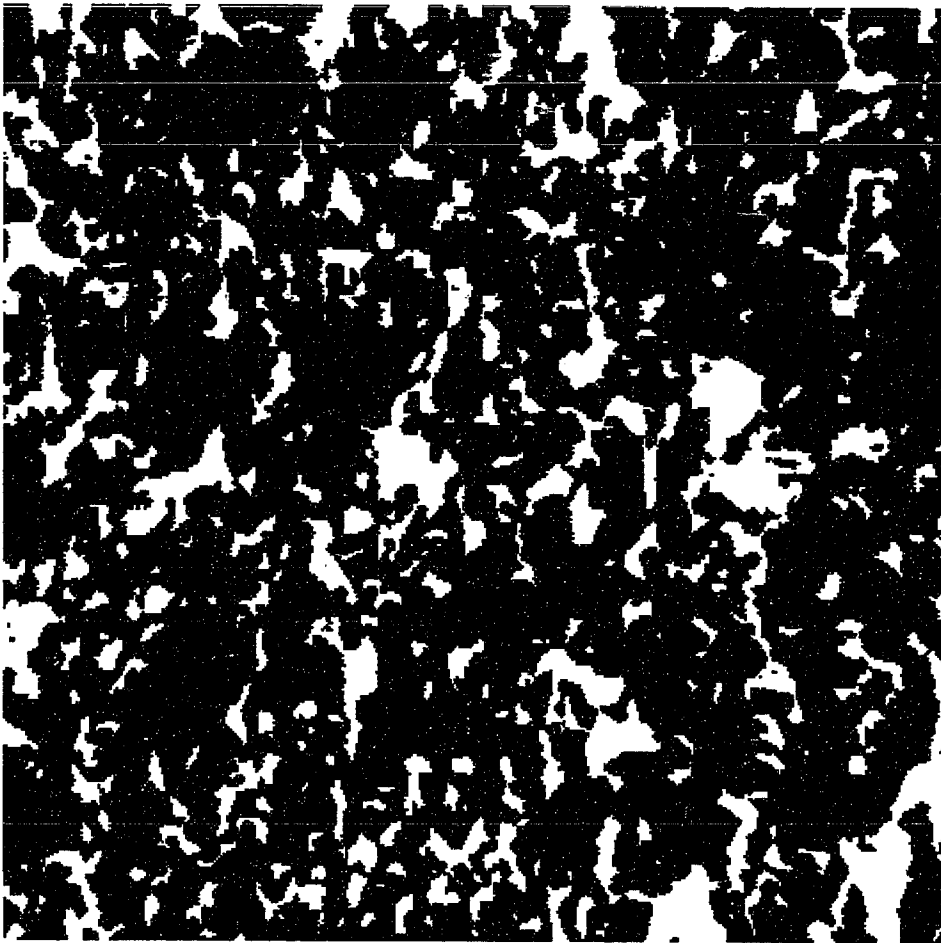


Figure 5.2: Snow section from March 3, 1993.

$$\log D_g = \frac{\bar{L}^4}{\bar{L}^2 \bar{L}^3 \sqrt{\bar{L} \bar{L}^3}} \quad (5.20)$$

$$\log^2 \sigma_g = \log \left(\frac{\bar{L} \bar{L}^3}{\bar{L}^2} \right). \quad (5.21)$$

The geometric mean and standard deviation for the ice grain diameters in fig. 5.2 were calculated using (5.20) and (5.21) to be $D_g = 0.552$ mm and $\sigma_g = 1.8$.

5.3.3 Recovery of g_v

To measure the area pair distribution function g_A the grain profiles appearing on the sections were fit with equivalent sized circles. This process was applied to fig. 5.2 and repeated for a second snow section from the same day. The two were averaged together to give g_A as a function of distance in millimeters which is shown in figure 5.3b. The integral in 5.11 was evaluated numerically for a log-normal cumulative distribution R_v to obtain the matrix in (5.7). The matrix inversion yielded the volume pair distribution function g_v shown as a solid line in fig. 5.3a.

As also seen in tests with multi-size Monte Carlo data, g_v bears a close resemblance to g_A . The difference between the two is most pronounced at short distances where peaks and valleys appear and deepen in g_v . Also shown in fig. 5.3a is g_v calculated under the Percus-Yevick (PY) approximation. The dotted line is for a PY calculation where five sizes (25 pair functions) are considered in the sum in (5.13). This curve agrees somewhat with g_v recovered from the snow data, but fails to produce the peaks for particles approximately 1.5 mm in diameter. The dashed line more closely approximates a continuum of sizes by using 100 diameters (10000 pair functions) in the PY calculation. As seen from the figure, the resultant volume pair distribution function has the form of a hole correction approximation and does not agree well with the data. This suggests that the snow is not a true continuum of sizes but can be better modeled by careful choice of a small number of representative diameters.

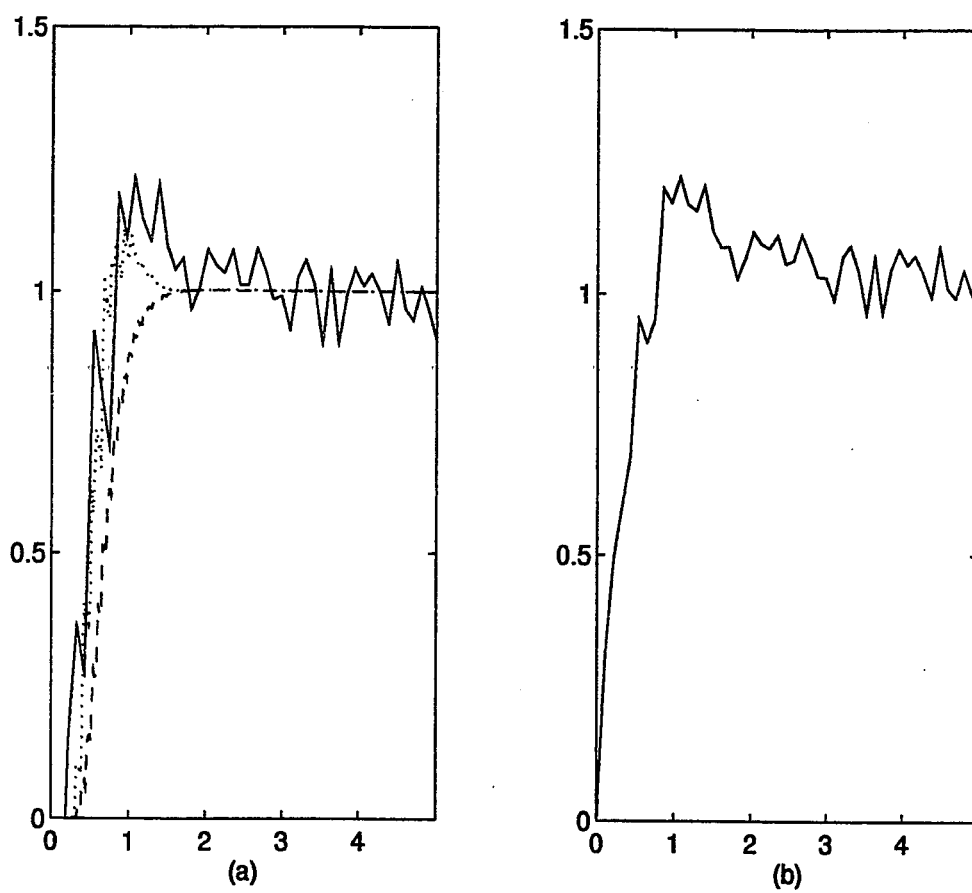


Figure 5.3: a) Recovered volume pair function g_v for particles in fig. 5.2 (solid line), g_v calculated from PY with five sizes (dotted line) and g_v calculated from PY with 100 sizes (dashed line). b) area pair function g_A from snow sections.

5.4 Scattering from a Distribution of Spheres

Under the QCA approximation, the effective wavenumber K for particles of relative permittivity ϵ_s can be written [22]

$$K^2 = k^2 + \frac{3k^2}{D} \sum_{s_l=1}^L f_{s_l} y \cdot \left\{ 1 + i \frac{2k^3 y}{3D} \left[a_{s_l}^3 + \sum_{s_j=1}^L a_{s_j}^3 8\pi^3 n_{s_j} H_{s_j s_l}(p=0) \right] \right\} \quad (5.22)$$

where

$$y = \frac{\epsilon_s - \epsilon}{\epsilon_s + 2\epsilon} \quad (5.23)$$

$$D = 1 - y f_v \quad (5.24)$$

and $H_{s_j s_l}(p=0)$ is related to the Fourier transform of the correlation function $h_{ij}(r) = g_{ij}(r) - 1$ by

$$\tilde{H}_{ij}(p) = (n_{s_i} n_{s_j})^{\frac{1}{2}} \int dr \exp(ip \cdot r) h_{ij}(r) \quad (5.25)$$

$$H_{s_i s_j}(p) = \frac{\tilde{H}_{ij}(-p)}{(2\pi)^3 (n_{s_i} n_{s_j})^{\frac{1}{2}}} \quad (5.26)$$

The extinction of the coherent wave is due loss of energy to scattering and absorption with an extinction coefficient of $\kappa_e = 2Im(K)$. In this chapter we consider spheres with a real permittivity of $\epsilon = 3.2\epsilon_0$ and the extinction is due solely to scattering effects. The effective wavenumber under QCA-CP can also be written in terms of $H_{s_j s_l}(p=0)$ as

$$K^2 = k^2 + \frac{3K^2}{D} \sum_{s_l=1}^L f_{s_l} y \cdot \left\{ 1 + i \frac{2K^3 y}{3D} \left[a_{s_l}^3 + \sum_{s_j=1}^L a_{s_j}^3 8\pi^3 n_{s_j} H_{s_j s_l}(p=0) \right] \right\}. \quad (5.27)$$

Under the Percus Yevick approximation, \tilde{H}_{ij} can be calculated and the inverse Fourier transform yields g_{ij} . The hole correction approximation gives

$$g_{ij}(r) = \begin{cases} 0 & r < a_{s_l} + a_{s_j} \\ 1 & r \geq a_{s_l} + a_{s_j} \end{cases} \quad (5.28)$$

and

$$\int_{-\infty}^{\infty} d\bar{r} [g_{ij}(\bar{r}) - 1] = (2\pi)^3 \tilde{H}_{ij}(p) = -\frac{4\pi}{3} (a_{s_l} + a_{s_j})^3. \quad (5.29)$$

For densely packed systems with a small number of distinct particle sizes it has been shown that the hole correction approximation is not accurate because it neglects the loss of freedom in particle position that the density imposes [22]. However the contribution from the pair distribution function to scattering is weighed by the particles' number density and size as can be relatively small for large particles with very small number densities, as discussed in the following section.

5.4.1 Independent Scattering and Correction Terms

For large particles with a low number densities the contribution to g_v in (5.13) is small. However, the scattering contribution for is not small because it is proportional to the particle size. This can be understood by examination of equations (5.22) and (5.27). The scattering strength is proportional to the imaginary part of these expressions, or the part in the square brackets. The first term in the brackets is the independent scattering contribution from species s_l . Using the QCA-CP approximation, we can define the independent extinction coefficient as the independent scattering from all species:

$$\kappa_{ind} = \frac{8k^5 y^2 \pi}{3K_r D^2} \sum_{l=1}^L \zeta(a_{s_l}) \quad (5.30)$$

$$\zeta(a_{s_l}) = n_{s_l} a_{s_l}^6 \quad (5.31)$$

where K_r is the real part of the effective wave number. For large particles, the factor of $a_{s_l}^6$ in (5.31) results in a strong independent scattering contribution.

The second term contributing to scattering is a “correction” term due to interaction between species s_l and s_j . This term accounts for the correlated scattering in a densely packed system and serves to *decrease* the independent scattering. The magnitude of the correction term is governed by the structure factor $H_{s_j s_l}(0)$ and multiplied by $n_{s_j} a_{s_j}^3$. We can define the correction term for a given species s_j with all other species s_i as

$$\zeta_{corr}(a_{s_j}) = \sum_{i=1}^{i=L} n_{s_i} n_{s_j} a_{s_i}^3 a_{s_j}^3 8\pi^3 H_{s_i s_j}(0) \quad (5.32)$$

For the large, sparse particles the correction terms are small in comparison with the independent scattering implying that knowledge of the exact form of the pair functions for these sizes is not crucial. The total scattering is a combination of the independent and correction terms and can be represented as a cumulative sum

$$\Gamma(a_{s_l}) = \kappa_{ind} + \frac{8k^5 y^2 \pi}{3K_r D^2} \sum_{j=1}^{j=l} \zeta_{corr}(a_{s_j}) \quad (5.33)$$

such that $\Gamma(a_{s_L}) = \kappa_e$.

5.4.2 Representative Particle Diameters

An important question is which particle sizes to choose to represent the ice grains. To explore this question we compared a log-normal system with 200 sizes with one with only seven representative diameters. For both the geometric mean diameter was $D_g = 0.52$ mm and the geometric standard deviation was 1.8. Figure 5.4 shows the comparison between the 200 sizes (dashed lines) and the seven sizes (shown as asterisks). Figure 5.4a shows the normalized density of the particles and Fig.5.4b and 5.4c shows the cumulative extinction Γ as a function of particle diameter with a PY pair distribution function at a frequency of 17 GHz. The plot in Fig.5.4b shows Γ decreasing rapidly as the correction terms for particles on the order of 2 mm in diameter are added. When all particles less than approximately 4 mm have been accounted for, Γ levels off indicating that the correction terms from the larger sizes have little effect on the cumulative scattering. The shape of Γ for the seven sizes in Fig.5.4c exhibits the same characteristics. The extinction coefficient calculated for the seven sizes ($\Gamma(a_{s_L}) = \kappa_e = 0.2394 \text{ m}^{-1}$) is within 1% of that calculated with the 200 sizes.

The solid line in fig. 5.4d shows the independent scattering term $\zeta(a_{s_j})$ for fig.5.4b normalized to its maximum and plotted as a function of diameter. The strongest contribution is from particles approximately 3 mm in diameter. Particles that are larger than this have insignificant number densities and smaller particles don't scatter as strongly due to the factor of a^6 in (5.31). The dotted line is the slope of fig.5.4b

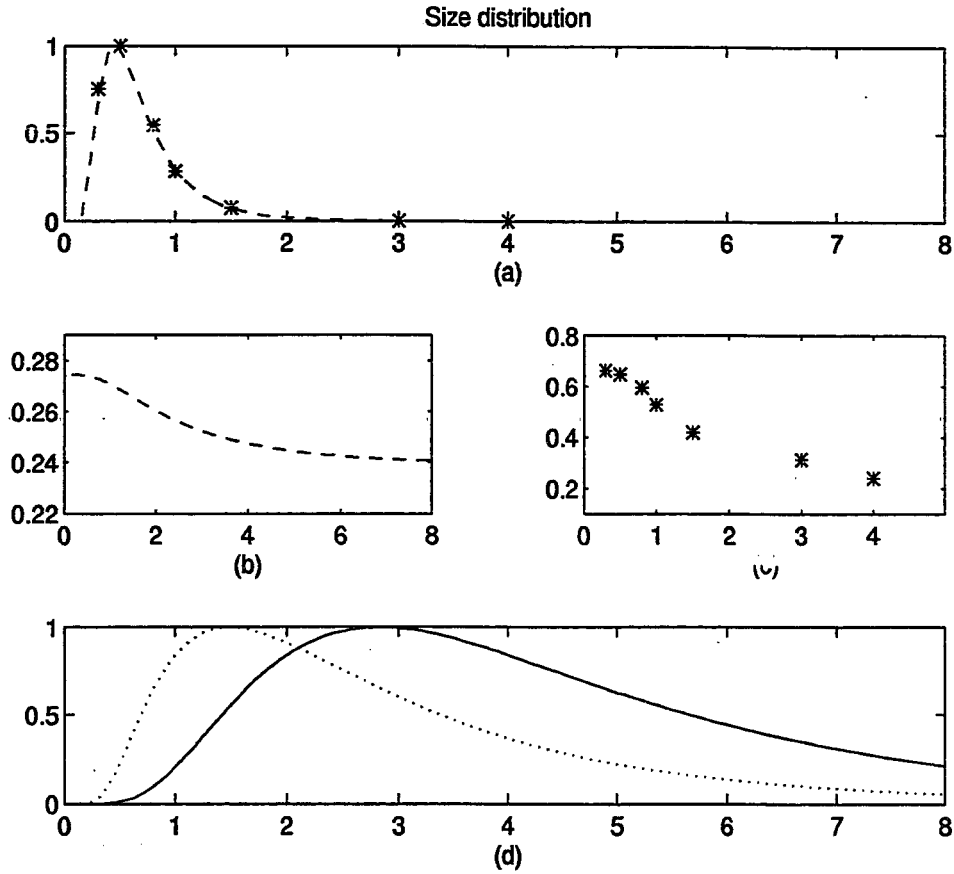


Figure 5.4: Calculations plotted versus particle diameters based on system of log-normally distributed spheres with $D_g = 0.52$ and $\sigma_d = 1.8$. a) Normalized densities for 200 sizes (dashed line) and discrete diameters 0.3, 0.5, 0.8, 1.0, 1.5, 3.0 and 4.0 mm (asterisks) b) Extinction $\Gamma(a_s)$ for continuous sizes c) Extinction $\Gamma(a_s)$ for discrete sizes d) Independent scattering (solid line) and derivative with respect to diameter (dotted line) for plot in b.

normalized to its maximum negative value. This curve is a measure of the relative strength of the correction term ζ_{corr} and has a maximum at a sphere diameter of approximately 1.5 mm. This indicates it is necessary to include the small- to mid-range particles when the pair functions are calculated or the density effects will not be taken into consideration. The effect of the more numerous particles is to restrict the freedom of the system resulting in a reduction in scattering strength relative to independent scattering.

The larger particles scatter strongly but the relative contribution from their correction terms is small. This implies that the scattering computation for the seven sizes can be further simplified by using the hole correction approximation for the two larger sizes (3.0 and 4.0 mm). This approximation cannot be applied to the small and middle size particles since the density effects included in those pair functions are important. The extinction coefficient calculated in this manner is $\kappa_e = 0.2437 \text{ m}^{-1}$ which is within 8% of the value obtained using PY for 200 sizes.

5.5 Results with Monte Carlo Data

Calculations of densely packed systems of multi-species particles were tested with computer generated realizations of spheres. The spheres had three discrete sizes ($L=3$) whose relative number densities were specified by a log-normal distribution. The spheres were deposited using a Metropolis technique [24] with 30 shuffles for each of the 30 realizations so that their positions were non-overlapping and described by the Percus-Yevick pair distribution function. The following sections will discuss results from a Monte Carlo simulation for 30% fractional volume with geometric mean diameter $D_g = 0.5 \text{ mm}$ and sizes $r_1 = 0.25$, $r_2 = 1.5r_1$, and $r_3 = 2.5r_1 \text{ mm}$.

5.5.1 Pair Functions and Scattering Calculations

The largest size particle is on the tail of the log-normal distribution and occurs in small numbers, accounting for only 2.05 % fractional volume. In the Monte Carlo simulations, of the $N = 3949$ spheres only 29 of the larger size were present in each realization. This means many more realizations are needed to get an accurate estimate of g_{33} than for the more plentiful smaller sizes. However, the relative contribution of the larger size to the total pair function is small since there is a factor of $n_{s_i}n_{s_j}$ in (5.13) and $n_3 \ll n_1$. The right panel of fig. 5.5 shows the total pair function g_v in (5.13) from the Monte Carlo data (dotted line) compared with that calculated analytically from the Percus-Yevick formulation (solid line). As seen in the figure the total pair function g_v calculated analytically compares well with that calculated from Monte Carlo simulations. The left panel of the same figure shows the individual g_{11} , $g_{12} = g_{21}$, $g_{13} = g_{31}$, $g_{22}, g_{23} = g_{32}$ and g_{33} from analytical calculation.

Figure 5.6 shows the pair functions for the three species with extinction values at 17 GHz. For each of the three sizes the independent scattering term ζ and the cumulative extinction Γ is given in units of m^{-1} to the left of that row. The total normalized extinction coefficient for all three species is $\kappa_e = 0.014 \text{ m}^{-1}$.

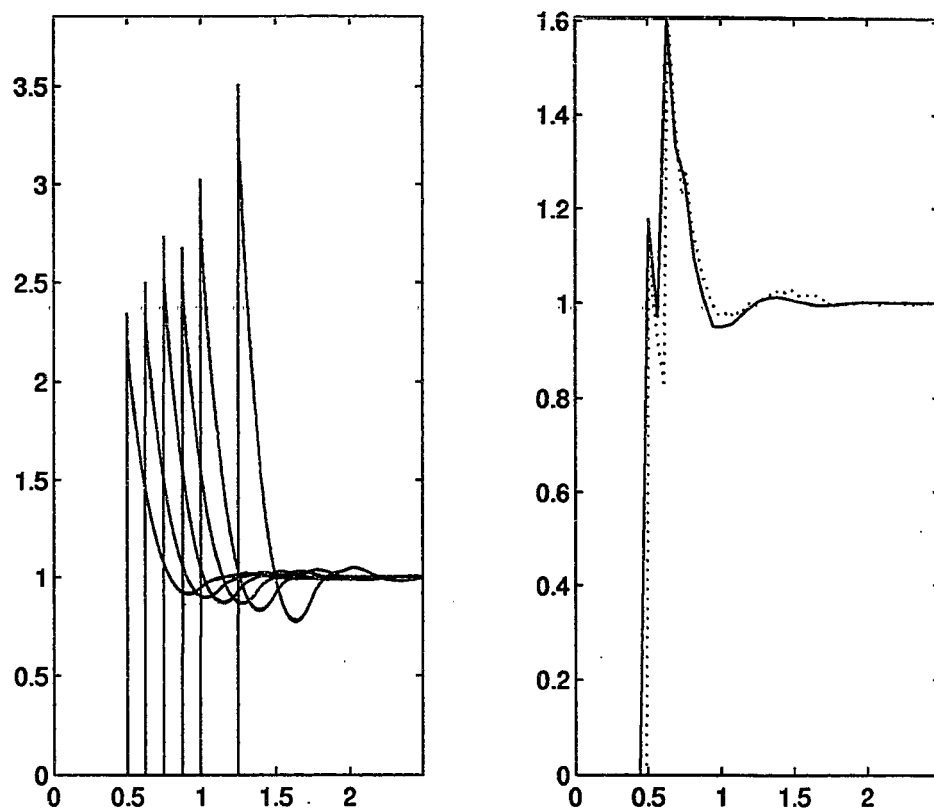


Figure 5.5: Pair functions calculated from Percus-Yevick (solid line) and Monte Carlo simulations (dotted line) for sizes $r_1 = 0.25$, $r_2 = 1.5r_1$, and $r_3 = 2.5r_1$ mm. and number densities $n_1 = 2964$, $n_2 = 956$, $n_3 = 29$.

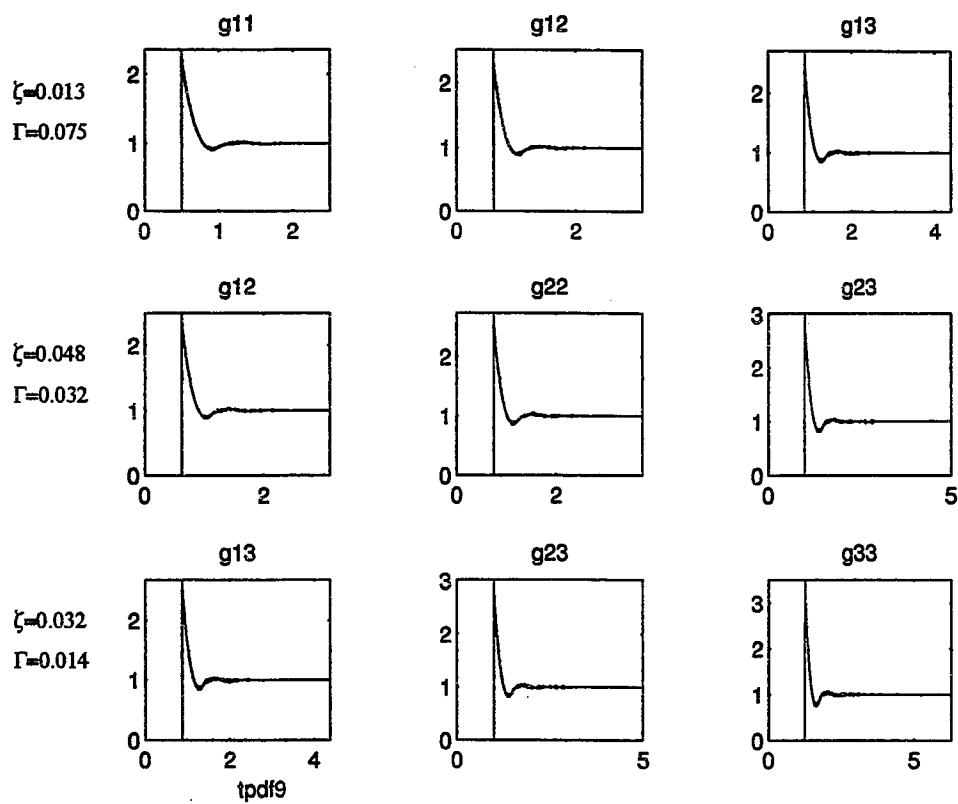


Figure 5.6: Pair functions and extinction rates for particles in fig. 5.5.

From the values in the figure, the following observations can be made :

- The smallest size is the most abundant in the system but has the lowest independent scattering contribution because of its size. Its importance is in the correction terms (decrease in the freedom of position that it imposes on the system).
- The middle size has adequate number density and sufficient size such that its contribution as a scatterer and as a space occupant are both important.
- The largest size represents a strong scatterer but has a weak correction term due to its low number density. Although it constitutes only 6.8 % of the scatterer volume it accounts for over 50 % of the independent scattering contributions. Note that g_{33} is strongly peaked indicating a lack of freedom in position. Even though there is a small number of these large particles, they are packed in with the other two more numerous species.
- Under the independent scattering assumption $\kappa_e = 0.013 + 0.048 + 0.032 = 0.093 \text{ m}^{-1}$ which is 6.4 times larger than the extinction when the interaction between the species (the correction terms) are considered.

The above observations indicate that each of the species in the system plays an important but different role in determining the level of the scattering. More specifically, the densely distributed small and medium sized spheres constrain the system, while the large and medium spheres have strong independent scattering.

5.5.2 Pair Function Retrieval

For the Monte Carlo data, the volume pair distribution function g_v is known since the 3-D positions and sizes of all the particles are known from the simulation : g_v averaged over the 30 realizations is shown in fig. 5.7a. The value for $I(x, r)$ can be computed analytically where R_v is a distribution of three discrete sizes with specified number densities. The two together can be used in (5.3) to give the "actual" g_A which is shown in fig. 5.7b. The top row of fig. 5.7 shows that the sharp features of g_v are still present in g_A but are considerably smoothed due to the 2-D sampling of the Monte Carlo volume.

When the 3-D characteristics of a discrete particle system are not known g_A cannot be determined as above but needs to be measured from the 2-D section data as outlined in equation (5.3). The Monte Carlo data provides an ideal opportunity to test the accuracy of the measurement process against the "true" g_A . The $N_r = 30$ realizations of $N = 3949$ spheres each were "cut" into $N_s = 20$ equally spaced section planes. Some of the particles - particularly the larger sizes - were cut more than once in different locations. An estimate of g_A was then obtained by averaging (5.5) over the 30 realizations. For the result shown in fig. 5.7d a sampling spacing of $\delta = 0.025$ mm over the range of 0 to 2.50 mm was used. Comparison between fig. 5.7b and fig. 5.7d indicates the estimate of g_A is very good.

The retrieval of g_v via (5.3) uses the size information in R_v to recover the sharp features and results in a function that looks similar to g_A but with more pronounced elements. Figure 5.7a compares well with fig. 5.7c and the notch in the pair function due to the discretization of the three sizes (at $r=0.625$ mm where the pair function g_{12} comes on) is quite conspicuous. Also noticeable is the increase of noise due to the inversion.

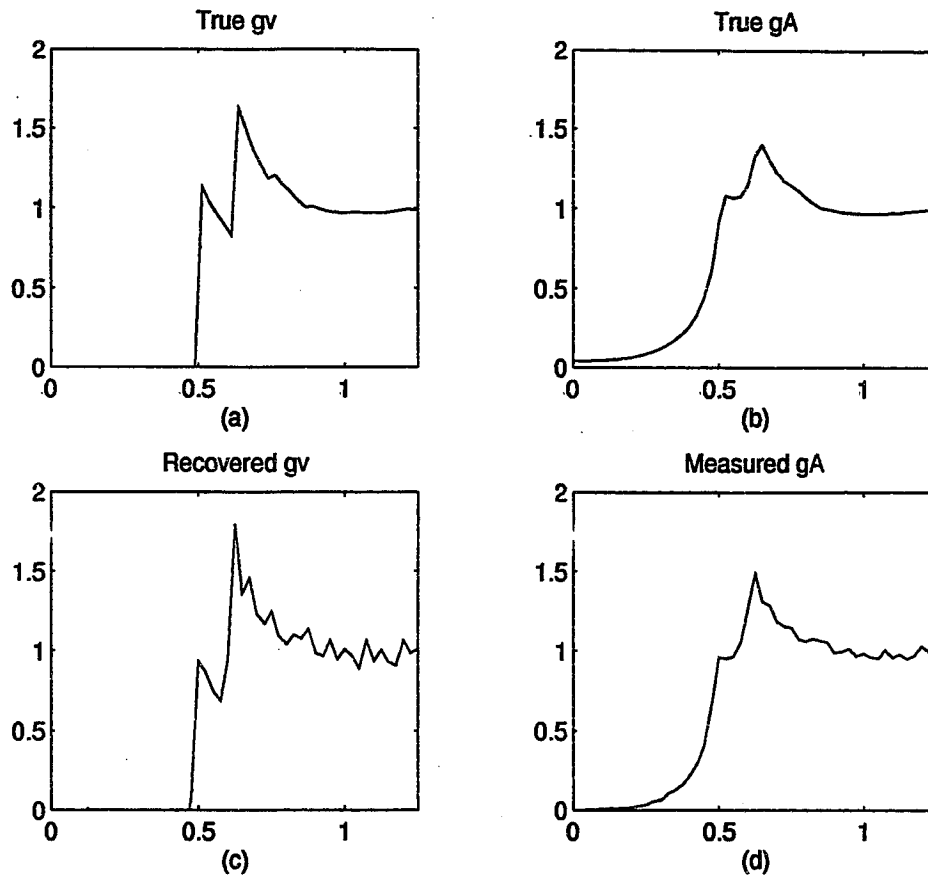


Figure 5.7: Recovered pair function for particles in fig. 5.5. The left hand plots show the total volume pair distribution function g_v and the right hand plots show the area pair function g_A . a) g_v is computed from Monte Carlo data b) g_A is obtained by solution of (5.3), c) g_v is obtained by solution of (5.3), d) g_A is computed from Monte Carlo data.

Table 5.1: Parameter values for investigation of sampling dependencies.

Figure	δ (mm)	A (cm ²)	χ^2
(c&d)	0.0125	768.0	1.7582
	0.0167	768.0	1.0556
	0.0250	768.0	0.4572
(a&b)	0.0333	768.0	0.3158
	0.0500	768.0	0.3591
(g&h)	0.0333	12.8	0.5696
(e&f)	0.0333	25.6	0.5575
	0.0333	76.8	0.4591
	0.0333	128.0	0.4319
	0.0333	256.0	0.3577

Sampling Requirements

To quantify the accuracy of the recovered g_v relative to the actual pair distribution function g_v^{actual} a chi-square statistic for two binned data sets can be employed

$$\chi_{gv}^2 = \sum_i \frac{\left(g_v^{actual}(r_i) - g_v(r_i)\right)^2}{g_v^{actual}(r_i) + g_v(r_i)}. \quad (5.34)$$

The value χ_{gv}^2 can be used to determine the resultant error in terms of the measurement parameters of g_A . This allows a quantitative exploration of the error associated with sampling size or with insufficient section data. Since it can be expected that the results will vary depending on particle distribution and density, this one case will provide only a general guide to the interplay between measurement parameters and error statistics. Numerical results can be found in table 5.1 with figure 5.8 showing the measured g_A and recovered g_v for selected cases.

The sampling size δ determines the appearance of the measured g_A as well as the spacing of the matrix in (5.7). Larger values of δ result in a very smooth g_A but at the expense of not capturing the sharper features. We varied δ from 0.0125 to 0.050 mm and found an error minimum at a spacing of 0.033 mm. This case is shown in the top row of figure 5.8a&b. Both g_A and g_v are noticeably smoother than in fig. 5.7 and the noise has decreased. However, the finer details of g_v are also lost. The height of both of the peaks has been smoothed and the coarser discretization has shifted the location of the valley slightly. The following two plots fig.5.8c&d show the opposite extreme with $\delta = 0.0125$. In these plots details of g_A and g_v are visible, but the noise has increased considerably. Thus there appears to be a trade-off between minimizing the noise and capturing finer details. In the general case when the actual g_v is not known a reasonable value for the spacing can be determined through trial and error by successively decreasing δ and resultant noise in g_A .

The extent of the section data is typically less controllable than the spacing, but it plays a related role. The section planes in the Monte Carlo simulation are 128 mm² in area and intersect approximately 190 spheres. In each realization the volume is cut into 20 sections, but because some spheres are cut more than once these sections are not independent. The total area of the sections in cm² is $A = 1.28 \times N_r \times N_s$, where N_s is the number of sections per realization. The results discussed thus far have been averaged over 30 realizations with $A = 768$ cm². Table 5.1 gives error estimates for limited section data with areas ranging between 12.80 to 256 cm².

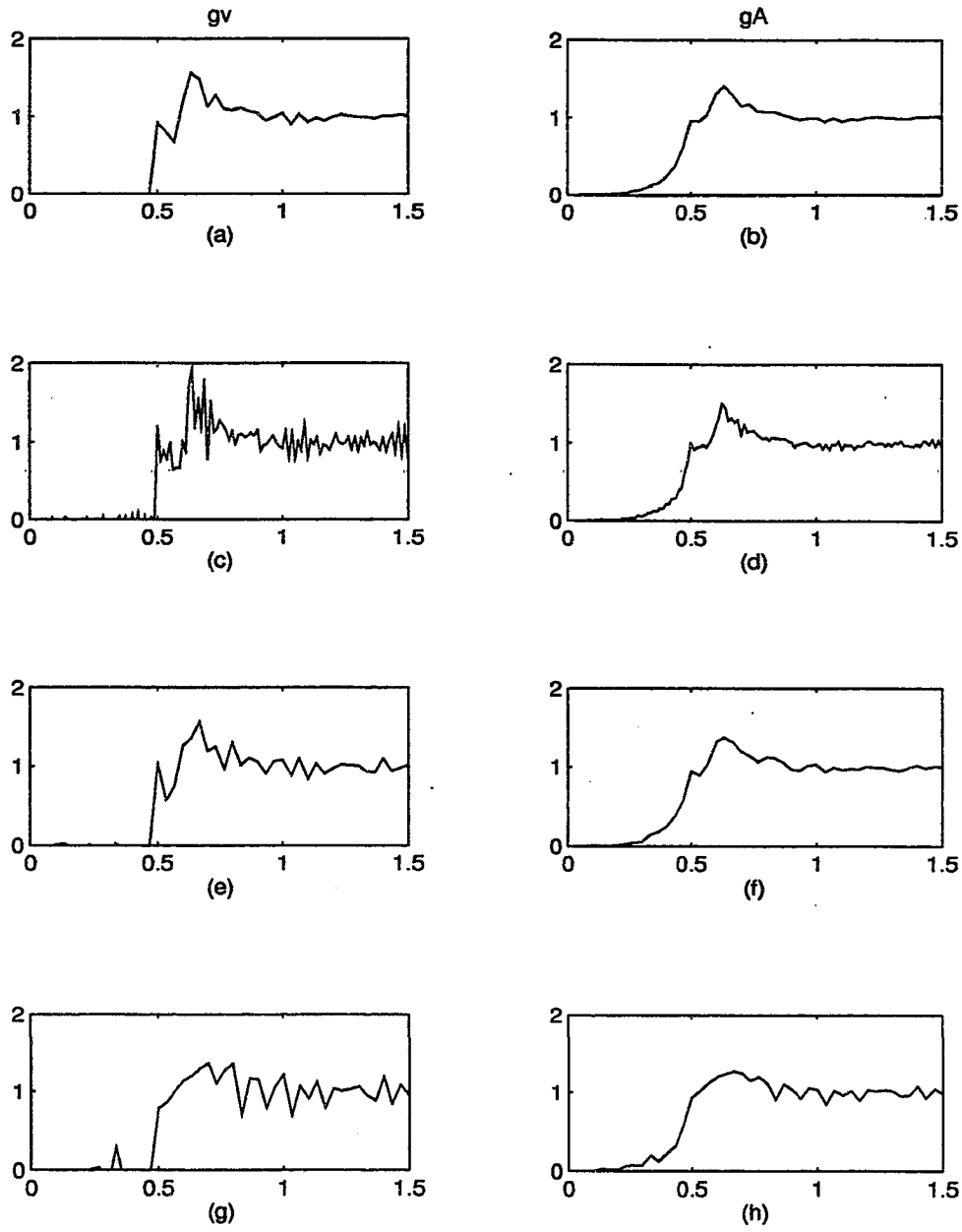


Figure 5.8: Examples of measured g_A and recovered g_v for the values in table 5.1.

For a single realization, the 20 sections total to only 25.60 cm^2 in area, but still produce a reasonable recovery of g_v as shown in figure 5.8e&f. The ramification of fewer realizations is the inability to capture the peaks in g_A and a rise in the noise level. This produces a more noisy g_v which is not as sharply peaked. Decreasing the section area to $A = 12.8 \text{ cm}^2$ by cutting only 10 sections from the single realization gives the plots in figure 5.8g&h. In these the lack of the dominant peak is highly prominent. Note that for this case the chi-square error is only 0.5575 - only a third of the computed error for fig.5.8c&d in which the features of g_v are successfully recovered. This illustrates the bias in the chi-square statistic. Because it is a least-squares measure, it tends to assign lower error values to less noisy data. If the intent of the recovery is to locate the peaks of g_v with great accuracy then the chi-squared statistics should be used in conjunction with the appearance of g_A and the recovered g_v .

Model Fit for Monte Carlo Data

Figure 5.9 shows the result of the model fit for the recovered pair distribution function. If the fit were perfect, the left panel would be identical to that in fig. 5.5. In fact, the pair functions for the more numerous, smaller sizes compare favorably but the fit is unable to determine the proper coefficients for the largest size, g_{33} . This is due to the previously mentioned fact that the number densities for these larger sizes are so low that g_v does not contain sufficient information to recover them properly. The comparison of the recovered g_v (solid line) with the fit (dotted line) is shown in the right-hand plot of the figure.

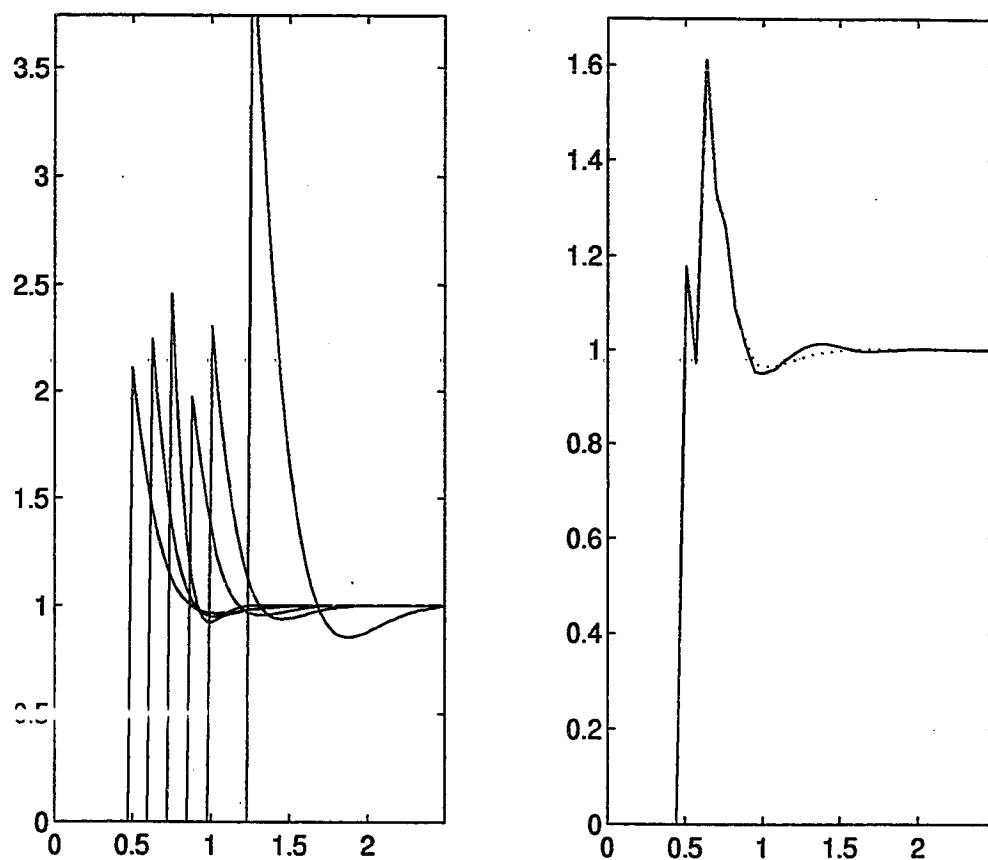


Figure 5.9: Recovered pair functions for particles in fig. 5.5. Left panel shows the six basis functions with adjusted parameters. Right panel shows the total pair function computed Percus Yevick (solid line) and the modeled g_v (dotted line) as in (5.14).

5.6 Scattering Calculations Based on Snow Section Data

The above analysis indicates that it is possible to retrieve g_v if a sufficient amount of section data is available. Furthermore, some of the individual pair functions can be modeled from a non-linear least squares fit of g_v . In this section we consider the procedure when applied to snow sections.

5.6.1 Model Fit for g_v

Based on the analysis of section 5.4.1 we choose five mid-range particle sizes for the fit. The recovered pair functions can then be used to determine the scattering for these five particles and the hole correction can be used to calculate the extinction for the two larger sizes.

The results of the fit procedure are strongly dependent on the initial guess. Since the objective is to find functions X_k which are indicative of the physically meaningful pair functions g_{ij} we guided the fit in the following manner :

1. Choose the amplitude of g_{ij} so that it accounts for the value of the pair function at their peak, i.e., $A_{ij} = (g_v(r = r_i + r_j) / (n_i n_j - 1)) * (r_i + r_j)$. Choose the decay factor μ_{ij} so that it is inversely proportional to the number density of the i th and j th species.
2. Allow the fit to determine the ideal values for A_{ij} and μ_{ij} . Accept or reject the resultant values based the following criteria:
 - Reject any negative values.
 - Accept amplitudes that are very large (i.e., $A_{ij} > 100$) only if $r_i = r_j$ is the smallest radii considered.
 - Reject if the large, sparse sizes have slow decays.
 - Accept the small to medium sizes if they have slow decays.

3. Hold the accepted values constant and fit the remaining (rejected) values by returning to step 1. Stop when none of the values are rejected.

Since the solution to (5.13) is non-unique, these “rules” are necessary to restrict the parameter space of the fit process. In particular, they force the pair functions for the small, more densely distributed spheres have longer correlation lengths while the larger, sparsely distributed spheres are strongly peaked with rapid decay and oscillation. This behavior is seen in the Percus-Yevick pair distribution functions and indicates that the positions of the larger particles are most strongly constrained due to their size. The decay parameter μ_{ij} determined from Percus-Yevick for a three size system is shown as a function of $r_i + r_j$ in figure 5.10.

The family of functions recovered for the snow section are shown in fig. 5.11 and fig. 5.12 for diameters 0.30, 0.50, 0.80, 1.00, 1.50 mm. The values obtained from the model fit can be combined with a hole correction calculation of larger particles (at 3 and 4 mm) to yield a total extinction of $\kappa_e = 0.2456 \text{ m}^{-1}$. This is comparable to the extinction $\kappa_e = 0.2393 \text{ m}^{-1}$ derived under PY for 200 sizes.

5.7 Discussion and Conclusions

The 3-D pair distribution function can be related through Hanisch’s integral equation to the 2-D probability of particle separation. This second quantity is easily obtained stereologically and the inverse of the integral equation yields the volume pair distribution function. This process has been tested with computer simulation and applied to snow sections.

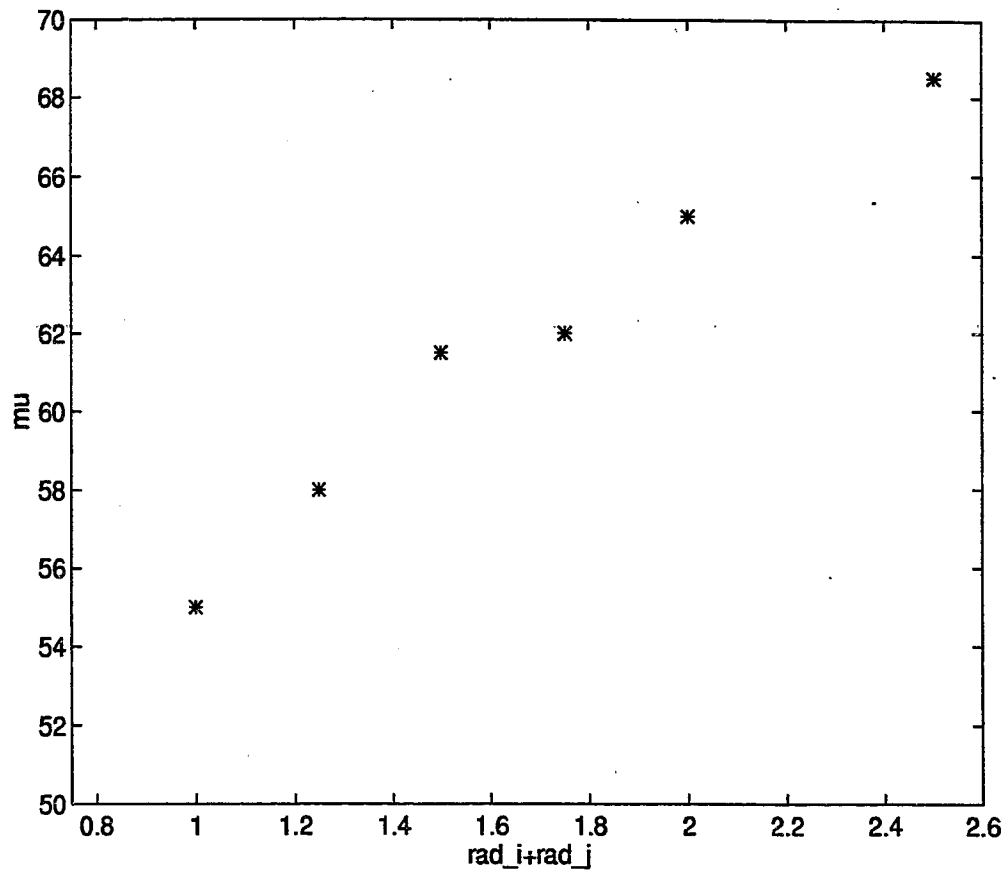


Figure 5.10: Decay parameter μ_{ij} determined from Percus-Yevick for a three size system and shown as a function of $r_i + r_j$.

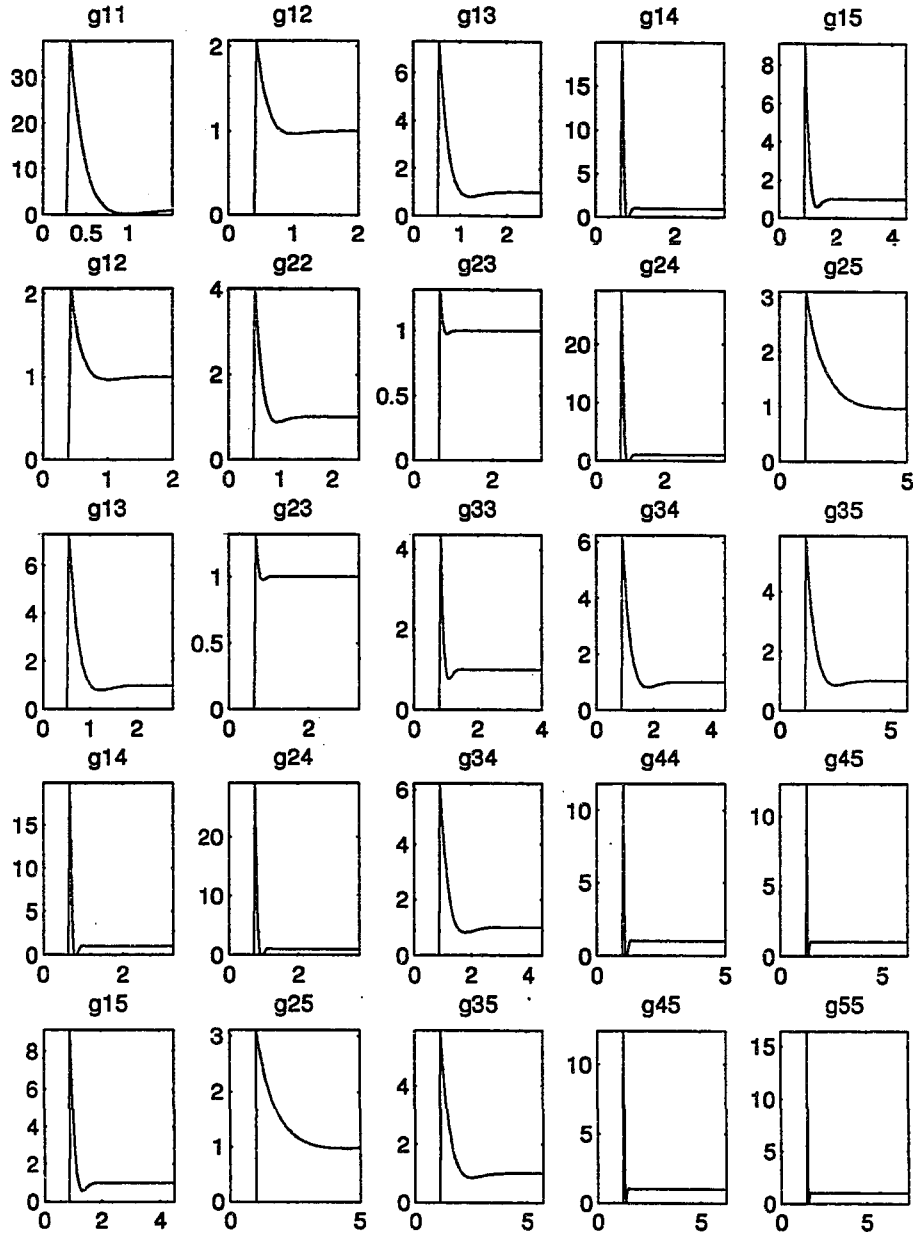


Figure 5.11: Non-linear model fit for snow section in fig. 5.2 and five diameters 0.30, 0.50, 0.80, 1.00, 1.50 mm. Each pair function $X_k(r) = g_{ij}(r)$ is described by the parametric form in (5.16).

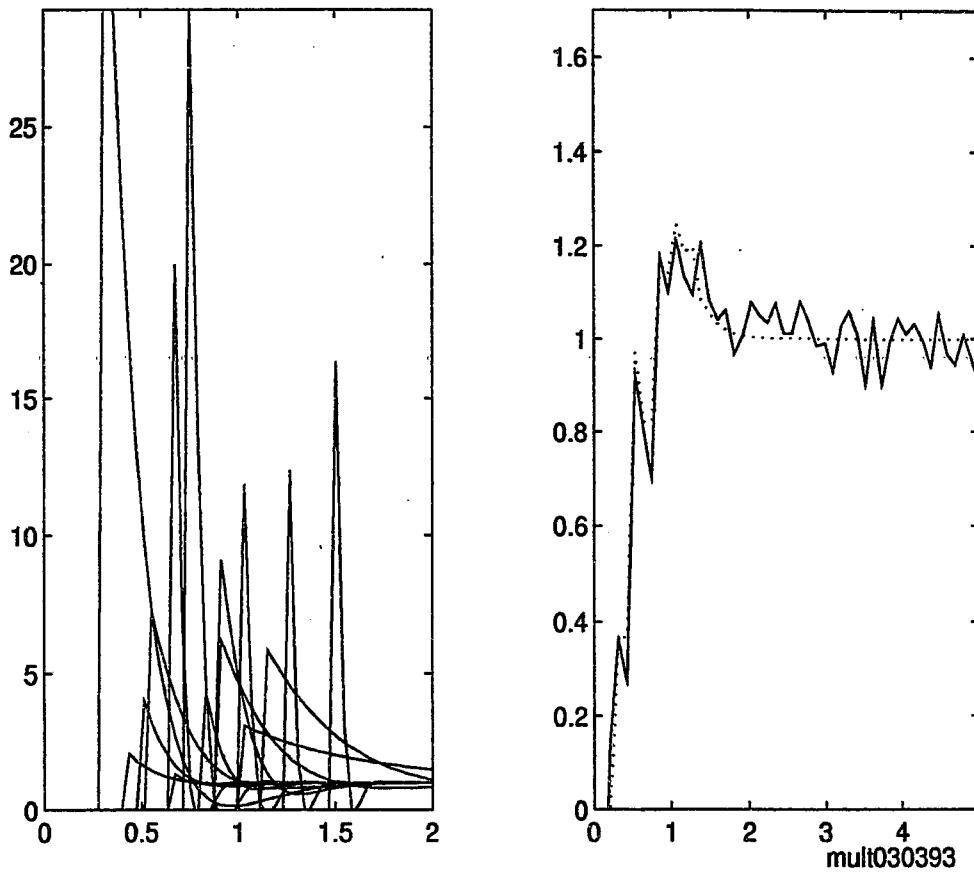


Figure 5.12: Non-linear model fit for snow section in fig. 5.2. The left panel shows the 15 pair functions g_{ij} and the right panel shows the total pair function g_v where the dotted line is the fit and the solid line is from the snow section.

The snow is modeled as a collection of spherical ice grains with a log-normal distribution of diameters. The parameters of the distribution are determined from stereological measurements. The recovered volume pair distribution function can be represented as a weighted sum of size specific pair distribution functions whose forms are determined through a least squares fit. Only those sizes in the distribution which have sufficient number density can be retrieved. To restrict the domain of the fit a set of physically meaningful rules is devised to guide the initial guess.

In multi-species systems different sized spheres have distinct roles in the collective scattering. The independent scattering contribution from each size particle is heavily weighted by its size. The correction terms account for the interaction of each species with the others and include the pair distribution function. Larger spheres which occur in small numbers have a major independent scattering contribution but relatively small correction terms. For small- to mid-range particles the opposite is true : the independent scattering is moderate but the correction terms are large due to the higher number densities.

In the snow data the grain sizes are approximated by seven discrete sizes where scattering from the largest two is calculated under the hole correction approximation. The five remaining sizes yield fifteen unique pair functions which are retrieved by the non-linear least squares fit. The resulting pair functions yield scattering rates that are comparable to those calculated under the Percus Yevick approximation.

Chapter 6

CONCLUSIONS AND RECOMMENDATIONS

This dissertation investigates the correlated scattering in densely packed, discrete random scatterers using Monte Carlo simulations and analytic dense media theory. The Monte Carlo simulations provide a tool with which to evaluate results obtained under classic methods and with dense media theory such as quasi-crystalline approximation (QCA) and quasi-crystalline approximation with coherent potential (QCA-CP). In addition, the Monte Carlo simulations are used to determine the scattering coefficient, absorption coefficient, effective permittivity and phase matrix for use in the dense media radiative transfer equations for application to active microwave remote sensing of snow covered regions.

To investigate the effect of the scatterer placement on the electromagnetic wave a sticky-particle pair distribution function is introduced which includes the adhesive character of the particles that causes them to clump together. This adhesive character may provide a more accurate depiction of particles that exist in clusters (for example snow grains). The effect of the sticky-particles on the electromagnetic wave is calculated analytically using QCA and numerically with Monte Carlo simulations. To generate a more realistic description of snow, snow sections prepared for stereological analysis are used to determine a family of pair distribution functions that contribute to the scattering.

6.1 Summary of Research

6.1.1 Sticky Hard Sphere Pair Distribution Function

We have shown that it is possible to describe adhesive particles statistically with the Percus-Yevick sticky particle pair distribution function. It is also possible to use this pair function in dense media scattering theory when the media in consideration has particles with a tendency to cluster. The experimental data we considered from one such media could only be explained by considering this stickiness.

The effect on the scattering behavior when the particles bond has been investigated. The primary effect is the increased attenuation due to the large cluster size, which show characteristics of scattering from a larger particle. However, when we attempted to reproduce the scattering using only non-sticky particles, we were unable to do so. This implies the stickiness of the particles needs to be taken into consideration to obtain accurate results.

6.1.2 Monte Carlo Simulations

The Monte Carlo simulations provide a valuable tool for testing our understanding of electromagnetic wave propagation through dense media. The simulations take into account correlated scattering and coherent wave interaction. The coherent and incoherent fields distributions can be used to calculate the extinction and absorption coefficient of densely packed discrete, dielectric, absorbing spheres. The spheres are deposited into a test volume in a random fashion, both with and without surface adhesion. Scattering and absorption are calculated using a numerically exact iterative formulation of Maxwell's multiple scattering equations, in which the contributions of the electric and magnetic dipoles were considered.

The scattering predicted by QCA and QCA-CP agrees well with the results of the Monte Carlo simulations. In contrast, the independent scattering assumption overestimates the amount of scattering when the scatterers occupy any more than a few percent by volume. At higher fractional volumes (i.e., $> 35\%$), QCA and QCA-CP predict slightly lower extinction rates than the Monte Carlo simulations, perhaps due the low-frequency approximations used in the solution for QCA and QCA-CP. The validity of the low-frequency approximation depends on ka and on the fractional volume. For a given ka , there is a threshold fractional volume above which the low-frequency assumption no longer holds. The value of the threshold decreases as ka increases.

The absorption coefficient for an ensemble of absorbing spheres was larger than that predicted by assuming independent absorption. While this may not be surprising for the case of clustered particles, it is also true when non-clustered, randomly positioned spheres are considered. The absorption enhancement is due to a modulation of each sphere's local exciting field as a result of the neighboring particles. In essence, the high local fields aid the ability of each sphere to absorb incident energy. The validity of the independent absorption assumption again depends on ka and the fractional volume, as observed for the validity of the low-frequency approximations used in QCA-CP. Results from a low-frequency approximation begin to disagree with the Monte Carlo results when fractional volumes greater than a threshold value are considered. The value of the threshold decreases with increasing ka .

Results of the Monte Carlo simulations show a clear dependence on the initial placement of the spheres. When interparticle adhesive forces cause clustering of the spheres, the scattering increases dramatically because of the effectively larger particle the clusters represent. This is in agreement with previous research on single fractal aggregations, which also found an increase in scattering. Both QCA-CP and the Monte Carlo simulations predict this increase in scattering for sticky spheres relative to the non-sticky case, but the magnitude of the increase is overestimated by QCA-CP. The increase is less pronounced at higher fractional volumes since the declining freedom of sphere placement curtails the clustering behavior.

6.1.3 Radiative Transfer Equation Applied to Remote Sensing of Snow

The Monte Carlo simulations can be used to calculate the extinction coefficient, phase matrix, and effective permittivity of the discrete random medium. These quantities are necessary for solution of the radiative transfer equation. The co-polarized elements of the phase matrix from the Monte Carlo simulations agrees with that obtained from DMRT. However, the off-diagonal elements are non-zero but are two orders of magnitude smaller than the copolarized energy. The presence of this depolarization is due to the random organization of the spheres which can give rise to perturbations in the internal dipole alignment. For very low frequencies, the random, isotropic arrangement of spheres causes cancelation of these deviations. For higher frequencies, since the wave will only add the dipole moments coherently over scales on the order of $\frac{1}{4}$ of a wavelength, the depolarization in the scattered field will remain.

Application of a radiative transfer model can yield different results depending on the assumptions used in calculation of the extinction coefficient, phase matrix, and effective permittivity. The independent scattering assumption gives overly high levels of backscatter due to overestimation of scattering. DMRT gives more realistic scattering coefficients, but neglects the first order depolarization effect. First order depolarization arises from coherent near field interaction among the spheres that creates

non-alignment of dipole moments. Using the phase matrix and scattering coefficient obtained from Monte Carlo simulations can produce co-polarized backscattering that is comparable to QCA-CP but also much higher levels of depolarized backscatter due to non-zero contributions from both first and second order effects. This combination results in a different snow depth and frequency dependence than indicated by conventional theory. Large increases in both copolarized and depolarized backscatter can be achieved by including the clustered nature of metamorphosed snow with a sticky particle model.

The effective permittivity of snow can be derived from the results of Monte Carlo simulations. The imaginary part of the effective wavenumber is related to the extinction coefficient for the incoherent wave and the real part corresponds to the phase progression of the coherent wave. The phase information is available both in the coherent scattering from the Monte Carlo volume as well as the oscillation of the internal dipole within the scatterers. The effective permittivity obtained from simulation yields an imaginary part that is in agreement with that predicted by QCA-CP. The real part of the permittivity agrees with that obtained from mixing formulas such as Clausius-Mossotti formula but is slightly lower than that predicted from QCA-CP.

6.1.4 Pair Function Retrieval from Planar Snow Sections

The 3-D pair distribution function can be related through Hanisch's integral equation to the 2-D probability of particle separation. This second quantity is easily obtained stereologically and the inverse of the integral equation yields the volume pair distribution function. This process has been tested with computer simulation and applied to snow sections.

The snow is modeled as a collection of spherical ice grains with a log-normal distribution of diameters. The parameters of the distribution are determined from stereological measurements. The recovered volume pair distribution function can be represented as a weighted sum of size specific pair distribution functions whose forms are determined through a least squares fit. Only those sizes in the distribution which have sufficient number density can be retrieved. To restrict the domain of the fit a set of physically meaningful rules is devised to guide the initial guess.

In multi-species systems different sized spheres have distinct roles in the collective scattering. The independent scattering contribution from each size particle is heavily weighted by its size. The correction terms account for the interaction of each species with the others and include the pair distribution function. Larger spheres which occur in small numbers have a major independent scattering contribution but relatively small correction terms. For small- to mid-range particles the opposite is true : the independent scattering is moderate but the correction terms are large due to the higher number densities.

In the snow data the grain sizes are approximated by seven discrete sizes where scattering from the largest two is calculated under the hole correction approximation. The five remaining sizes yield fifteen unique pair functions which are retrieved by the non-linear least squares fit. The resulting pair functions yield scattering rates that are comparable to those calculated under the Percus Yevick approximation.

6.2 Recommendations for Future Research

To accurately understand electromagnetic propagation and scattering in dense, discrete random media there needs to be, first, an accurate model of the random medium as well as, second, a rigorous method to compute the scattering.

The first consideration involves accurate modeling of a particle positions within the dense medium. When an aggregation of particles is formed under an external force (for example metamorphic processes involved in the sintering of snow) complicated microstructures can result. One way to produce these microstructures for the purpose of modeling the random medium is to understand the process sufficiently well so that the formation of the particle systems can be simulated, i.e., “grow” the snow. An alternate approach is to utilize observable quantities of the random medium - such as stereological data - to infer the structural details needed in an accurate model. The second major component is the ability to account for the wave interactions within the random media. In dense media, the correlation of the particles’ positions results in correlated scattering. Analytical theory such as QCA and QCA-CP take this into consideration through use of a pair distribution function but rely on use of reasonable approximations to obtain a closed form solution. The validity of dense media theory can be tested by the numerically exact formulation in the Monte Carlo simulations which explicitly accounts for all orders of multiple scattering. In this dissertation, computation of the extinction coefficient, absorption coefficient, phase matrix, and effective permittivity has been validated for the small particle case. Extension of this procedure to higher frequencies is desirable for many applications and would require future research to meet the challenges of the increased computational demands.

6.2.1 Specific Recommendations

Further investigation into the nature of the ice grain clusters that occur in snow is necessary to accurately evaluate their effect on the scattering physics. This dissertation research indicates that the microstructure of a particle system strongly effects the scattering. However, specific knowledge of this microstructure for snow is not yet available. The sticky hard sphere (SHS) pair distribution function is an attempt to address this problem. To use SHS to model geophysical media - such as snow - there needs to be a method to determine the stickiness parameter τ for the model.

In many types of random media three-dimensional information on the particle microstructure is unavailable. However, often it is possible to obtain two dimensional information stereologically and Hanisch's integral equation can then be used to recover a volume pair distribution function. When the particles are multi-sized this total pair function is a sum of the interactions between individual sizes weighted by their number density. The decomposition of the 3-D pair function into size specific pair functions needed for scattering computation poses a many-to-one problem. This dissertation restricts the inversion space by utilizing a set of rules to guide the least squares fit. However, these rules are postulated based on the observed behavior of particle systems (such as Percus-Yevick) and may not be widely applicable. More research needs to occur to determine a more rigorous method of restraining the solution space. One possibility is to obtain additional information from the random medium itself through sampling techniques.

The Monte Carlo simulations can be applied to higher frequencies if more spherical harmonics are retained in the series expansion. The inclusion of higher harmonics increases the memory and computational requirements for the simulations which can be accommodated by developing more advanced numerical methods. The ability to compute scattering at the higher frequencies can be used to determine radiative transfer quantities for passive microwave systems.

The research in this dissertation has concentrated on the application of remote sensing of snow. However, it could also be applied to determine properties of composite materials or in the application of non-destructive evaluation.

BIBLIOGRAPHY

- [1] Alley, Richard B., "Three-Dimensional Coordination Number from Two-Dimensional Measurements: A New Method", *Journal of Glaciology*, Vol. 32, No. 112, 1986
- [2] Ambach W. and Denoth, A., "Studies on the dielectric properties of snow", *Zeitschrift für Gletscherkunde und Glazialgeologie*, 8, 113-123, 1972
- [3] Barboy, B., "On a representation of the equation of state of fluids in terms of the adhesive hard-spheres model", *J. Chem. Phys.*, Vol. 61, pp 3194-3196, 1974.
- [4] R. J. Baxter, "Percus-Yevick equation for hard spheres with surface adhesion". *J. Chem. Phys.*, Vol 49, No. 6, pp. 2770-2773, Sept. (1968).
- [5] Baxter, R. J., "Ornstein-Zernike relation for a disordered fluid," *Aust. J. Phys.*, Vol. 21, 563-569, 1968.
- [6] Baxter, R. J., "Ornstein-Zernike relation and Percus-Yevick approximation for fluid mixtures", *J. Chem. Phys.*, Vol. 52, 4559-4562, 1970.
- [7] Bohren, C.F. and Battan, L.J. , "Radar backscattering of microwaves by spongy ice spheres", *J Atmosph. Sciences*, 39, 2623-2628, 1982
- [8] Chandrasekhar, S, Radiative Transfer, Dover, New York, (1960)

- [9] Chang, A. T. C., B.J. Choudhury, and P. Gloersen, "Microwave brightness of polar firn as measured by Nimbus 5 and 6 ESMR", *Journal of Glaciology*, 25(91), 85-91, 1980 16(74),23-39, 1976
 - [10] H.Y. Chen, and M. F. Iskander, "Light scattering and absorption by fractal agglomerates and coagulations of smoke aerosols", *Journal of Modern Optics*, Vol 37., No 2, 171-181, (1990).
 - [11] Chew, W.C. and Y. M. Wang, "A Fast Algorithm for Solutions of a Scattering Problem using a Recursive Aggregate τ Matrix Method", *Microwave Opt. Technol. Lett.*, Vol. 3, No. 5, 164-169, 1990
 - [12] Chew, W.C., Waves and Field in Inhomogeneous Media, Van Nostrand Reinhold, New York, 1990
 - [13] Colbeck, S., Akitaya, E., Armstrong, R., Gubler, H., Lafeuille, J., Lied, K., McClung, D., Morris, E., International Classification for Seasonal Snow on the Ground, Int. Comm. Snow and Ice (IAHS), World Data Center A for Glaciology, U. of Colorado, Boudler, CO, USA (1990)
 - [14] Colbeck, S.C., "An overview of snow metamorphism", *Reviews of physics and Space Physics*, Vol. 20, No. 1, 45-61, 1982
 - [15] Colbeck, S.C. , "The geometry and permittivity of snow at high frequencies", *J. Appl. Phys.*, 20, 45-61, 1982
 - [16] Colbeck, S.C. , " Classification of Seasonal Snow Cover Crystals", *Water Resources Research*, Vol. 22, No. 9, 59S-70S, Aug. 1986
-

- [17] Colbeck, S.C., "Statistics of Coarsening in Water-Saturated Snow", *Acta metall.*, Vol. 34, No. 3, pp. 347-352, 1986
 - [18] Cummings, W., "The dielectric pROperties of ice and snow at 3.2 cm.", *J. Appl. Phys.*, 23, 768-773, 1952
 - [19] Davis, Robert E., and Jeff Dozier, "Stereological Characterization of Dry Alpine Snow for Microwave Remote Sensing", *Adv. Space Res.*, Vol. 9, No. 1, 1245-1251, 1989
 - [20] V.A. Davis, and L. Schwartz, "Electromagnetic propagation in close-packed disordered suspensions", *Phys. Rev. B.*, Vol. 31, 5155-5165, (1985).
 - [21] Dimon, P., S.K. Sinha, D. A. Weitz, C. R. Safinay, G. S. Smith, W. A. Varady, and H. M. Lindsay, "Structure of Aggregated Gold Colloids", *Physical Review Letters*, Vo. 57, No. 5, 595-598, 1986
 - [22] Ding, K.H. and Tsang, L., "Effective Propagation Constants of Dense Nontenuous Media with Multi-Species of Particles", *Journal of Electromagnetic Waves and Applications*, Vol. 2, No. 8, 757-777, 1988
 - [23] Ding, K.H. and Tsang, L., *Progress in Electromagnetics Research*, vol. 1, (edited by J.A. Kong), Ch. 3, Elsevier Science Publishing Co., New York, 1989
 - [24] Ding, K.H. and Tsang, L., "Monte Carlo Simulations of Pair Distribution Functions of Dense Discrete Random Media With Multiple Sizes of Particles", *Journal of Electromagnetic Waves and Applications*, Vol. 6, No. 8, 1015-1030, 1992
-

- [25] Ding, K.H., Zurk, L. M. and Tsang, L., "Pair Distribution Functions and Attenuation Rates for Sticky Particles in Dense Media", *Journal of Electromagnetic Waves and Applications*, Vol. 8, No. 12, 1585-1604, (1994) †
- [26] Dougherty, Edward R., Mathematical Morphology in Image Processing, Marcel Dekker, New York, 1993
- [27] Dozier, Jeff, Robert E. Davis, "On the objective analysis of snow microstructure", *Avalanche Formation, Movement and Effects*, Proceedings of the Davos Symposium, Sept. 1986
- [28] A.W. England, *Radio Science*, 9, 447, 1975
- [29] A.W. England, "Thermal Microwave Emission From a Scattering Layer", *J. Geophys. Res.*, 80, 4484, 1975
- [30] Fikoris, J.G. and Waterman, P.C., "Multiple scattering of waves, II Hole corrections in the scalar case", *J. Math. Phys.*, 5, 1413-1420, 1964
- [31] Foldy, L.L., "The multiple scattering of waves", *Phys. Rev.*, 67, 107-119, (1945)
- [32] Good, Walter, "Thin subsections, serial cuts and 3-D analysis of snow", *Avalanche Formation, Movement and Effects*, Proceedings of the Davos Symposium, Sept. 1986
- [33] Gubler, H., "Model for Dry Snow Metamorphism", *Journal of Geophysical Research*, Vol. 90, No. D5, p8081-8092, Aug. 1985

† Portions of this publication have been reproduced in this thesis.

- [34] Hanisch, K.H., "On Stereological Estimation of Second-order Characteristics and of the Hard-core Distance of Systems of Sphere Centres", *Biometrical Journal*, Vo. 25, No. 8, 731-743, 1983
- [35] J. P. Hansen, and I. R. McDonald, Theory of Simple Liquids, (Academic Press, New York, 1986).
- [36] Harrington, Roger F., Field Computation by Moment Method, Macmillan, New York, 1968
- [37] Hobbs, P.V. and B.J. Mason, "The Sintering and Adhesion of Ice", *Proceeding of the Physical Society*, 181-197, Jan. 1964
- [38] A. Ishimaru, Wave Propagation and Scattering in Random Media, Academic Press, Ca., 1978
- [39] A. Ishimaru, and Kuga Y., "Attenuation constant of a coherent field in a dense distribution of particles", *J. Opt. Soc. Am.*, Vol. 72, 1317-1320, (1982).
- [40] Jakeman, A.J., and Anderssen, R.S., "Abel type integral equations in stereology. I. General discussion", *Journal of Microscopy*, Vol 105, Pt 2, Nov. 1975
- [41] J.W. Jansen, C.G. de Kruif, A. Vrif, *J. Colloid Interface Sci*, 114, pp. 481, 1986

- [42] Kendall, M.A. and Moran, P.A.P., Geometrical Probability, Hafner Publishing, New York, 1963
- [43] Kingery, W.D. "Regelation, Surface Diffusion, and Ice Sintering", *Journal of Applied Physics*, Vol. 31, 5, 833-838, May 1960
- [44] G. Koh, "Experimental study of electromagnetic wave propagation in dense random media", *Waves Random Media* 2, 39-48 (1992)
- [45] W.G.T. Kranendonk, and D. Frenkel, "Simulation of the adhesive-hard-sphere model", *Molecular Physics*, Vol. 64, No. 3, 403-424, (1988).
- [46] Kry, P.R., "Quantitative Stereological Analysis of Grain Bonds in Snow", *Journal of Glaciology* Vol. 14, No. 72, 467-477, 1975
- [47] Y. Kuga, and A. Ishimaru, "Retroreflectance from a dense distribution of spherical particles", *J. Opt. Soc. Am.*, Vol. 1, 831-835, (1984).
- [48] Y. Kuga, F. T. Ulaby, T. F. Haddock and R. D. DeRoo, "Millimeter-wave radar scattering from snow I. Radiative transfer model", *Radio Science*, vol. 26, No. 2, 329-341, March 1991
- [49] Lax, M., "Multiple scattering of waves", *Rev. Modern Phys.*, 23, 287-310, (1951)
- [50] C.C. Lu, W.C. Chew, et al, L., "The application of recursive aggregate T-matrix algorithm in the Monte Carlo simulations of the extinction rate of random distribution of particles", *Radio Science*, Vol. 30, No. 1, pp.25-28, Jan 1995.
- [51] B.B. Mandelbrot, The Fractal Geometry of Nature, (W. H. Freeman & Co. New York, 1983).

- [52] C.E. Mandt, Y. Kuga, Tsang, L., and A. Ishimaru, "Microwave propagation and scattering in a dense distribution of nontenuous spheres : experiment and theory", *Waves in Random Media*, Vol. 2, No. 3, 225-234, (1992).
- [53] Mätzler, Christian, "Applications of the Interaction of Microwaves with the Natural Snow Cover", *Remote Sensing Reviews*, Vol. 2, 259-387, 1987
- [54] J.C. Maxwell-Garnett, "Colours in metal glasses and in metal films", *Trans. of the Roy. Soc.*, V. CCIII, p 385-420, (1904).
- [55] Morse, P.M. and Feshback, H., Methods of Theoretical Physics, Part II, McGraw-Hill, New York, (1953)
- [56] K. Pak, Tsang, L., C. H. Chan, and J. Johnson, "Backscattering enhancement of scattering of electromagnetic waves from 2-D random rough surface", *J. Opt. Soc. Am. A*, in press, 1995
- [57] Papoulis, Athanasios, Probability, Random Variables, and Stochastic Processes, McGraw-Hill, New York, 1984
- [58] Penders, M.H.G.M., A. Vrij, "A turbidity study on colloidal silica particles in concentrated suspensions using the polydisperse adhesive hard sphere model", *J. Chem. Phys.*, Vol. 93, No. 5, pp. 3704-3711, Sept. 1990
- [59] Perla, R., J. Dozier and R.E. Davis, "Preparation of serial subsections in dry snow specimens", *Journal of Microscopy*, Vol. 141, 111-114, April 1986
- [60] Percus, J. K. and Yevick, G. J., "Analysis of classical statistical mechanics by means of collective coordinates", *Phys. Rev.*, Vol. 110, 1-13, (1958).

- [61] Peterson, B. and Ström, S., "T Matrix for electromagnetic Scattering from an Arbitrary Number of Scatterers and Representations of $E(3)^*$ ", *Physical Review D*, Vol. 8, No. 10, p.3661-2677, Nov. (1973)
- [62] Polder, D. and van Santen, J.H., "The effective permeability of mixtures of solids", *Physica*, XII(5), 30, 257-271, 1946
- [63] Press, William H., Flannery, Brian P., Teulosky, Saul A., and Vetterling, William T., Numerical Recipes in C, Cambridge University Press, 1988
- [64] Roth, L., "Effective medium approximation for liquid metals", *Phys. rev. B.*, Vol. 9,p. 2476-2484, (1974).
- [65] Russ, John C., The Image Processing Handbook,CRC Press, 1992
- [66] Schwartz L. and T. J. Plona, "Ultrasonic propagation in close-packed ordered and disordered suspensions", *J. Apl. Phys.*, 55, 3971-3977, 1984
- [67] Seaton, N.A., and Glandt, E.D., "Monte Carlo simulation of adhesive spheres", *J. Chem. Phys.*, Vol. 87, No. 3, 1785-1790, (1977).
- [68] Serra, J., Image Analysis and Mathematical Morphology,Academic Press, New York, 1982
- [69] Shalaev, V.M., Botet, R., and Jullien, R., "Resonant light scattering by fractal clusters",*Physical Review B*, Vol. 44, No. 22, 12,216-12,225, December (1991).
- [70] Shi, Jiancheng, Davis, Robert E., Dozier, Jeff, "Stereological determination of dry-snow paramters for discrete-scatterer microwave modeling", *Annals of Glaciology*, 17, 1993

- [71] Shin, R.T., and Kong, J. A., "Radiative transfer theory for active remote sensing of a homogenous layer containing spherical scatterers", *J. Apply. Phys.*, Vol. 52, No. 6, p 4221-4230, June 1981
- [72] Stiles, W.H., Ulaby, F. T., Aslam, A. and Abdelrazik, M., "Active microwave investigation of snowpacks: experimental data documentation, Colorado 1979-1980", University of Kansas Remote Sensing Lab. RSL Technical report 410-3
- [73] Stogryn, A., "The brightness temperature of a vertically structured layer", *J. Geophys. Res.*, 80, 4484-4496, (1970)
- [74] Stogryn, A., "Electromagnetic scattering by random dielectric constant fluctuations in a bounded medium", *Radio Science*, 9, 509-518, (1974)
- [75] Tiuri, M., Sihvola, A.H., Nyfors, E.G. and Hallikainen, M.T., "The complex dielectric constant of snow at microwave frequencies", *IEEE J. Oceanic Engin.*, OE-9, 377-382, 1984
- [76] Tsang, L., and Kong, J.A., "Multiple scattering of electromagnetic waves by random distribution of discrete scatterers with coherent potential and quantum mechanical formulism", *J. Appl. Phys.*, Vol. 51, 3465-3485, (1980).
- [77] Tsang, L. and Kong, J.A., "Scattering of electromagnetic waves from random media with strong permittivity fluctuations", *Radio Science*, Vo. 16, 3, 303-320, (1981)
- [78] Tsang, L., and Kong, J. A., "Multiple scattering of acoustic waves by random distributions of discrete scatterers with the use of quasicrystalline-coherent potential approximation", *J. Appl. Phys.*, Vol. 52, No. 9, Sept. (1981)

- [79] Tsang, L., and Kong, J. A., "Effective propagation constants for coherent electromagnetic wave propagation in media embedded with dielectric scatterers", *J. appl. Phys.*, Vol. 53, 7162-7173, (1982).
 - [80] Tsang, L., and Kong, J. A., "Scattering of electromagnetic waves from a half space of densely distributed dielectric scatterers", *Radio Science*, Vol. 18, 1260-1272, (1983).
 - [81] Tsang, L., J.A. Kong, and R.T. Shin, Theory of Microwave Remote Sensing, (Wiley-Interscience, New York, 1985).
 - [82] Tsang, L., "Passive Remote Sensing of Dense Nonteneous Media", *Journal of Electromagnetic Waves and Applications*, Vol. 1, No. 2, 159-173, 1987
 - [83] Tsang, L., and Akira Ishimaru, "Radiative wave equations for vector electromagnetic propagation in dense nontenous media", *Journal of Electromagnetic Waves and Applications*, Vol. 1, 809-813, 1992
 - [84] Tsang, L., and J.A. Kong, "Scattering of Electromagnetic Waves from a Dense Medium Consisting of Correlated Mie Scatterers with Size Distributions and Applications to Dry Snow", *Journal of Electromagnetic Waves and Applications*, Vol. 6, No. 3, 265-286, 1992
 - [85] Tsang, L., C. Mandt, and K. H. Ding, "Monte Carlo simulations of the extinction rate of dense media with randomly distributed dielectric spheres based on solution of Maxwell's equations", *Optics Letters*, Vol. 17, No. 5, 314-316, (1992).
 - [86] Tsolakis, A.I, I.M. Besieris, and W.E. Kohler, "Two-frequency radiative transfer equaataion for scalar wave in aa random distribution of discrete scatterers with pair correlation", *Radio Science*, Vol. 20, 1037-1052, 1985
-

- [87] Twersky, V., "On propagation in random media of scatterers", *Proc. Symp. Appl. Math.*, 16, 84-116, Am. Math. Soc., Providence, R.I., (1964)
 - [88] Twersky, V., " Multiple scattering of electromagnetic waves by arbitrary configurations", *J. Math. Phys.*, 8, 589-610, (1967)
 - [89] Twersky, V., "Coherent scalar field in pair-correlated random distributions of aligned scatterers", *J. Math. Phys.*, Vol 18, 2468-2486, (1977).
 - [90] Underwood, E.E., Quantitative Stereology, Addison-Wesley, Reading, Mass., 1970
 - [91] van de Hulst, H.C., Light Scattering by Small Particles, (Dover, New York, 1957)
 - [92] Varadan, V.K., Brongi, V. N., Varadan, V. A. and Ishimaru, A. "Multiple scattering theory for waves in discrete random media and comparison with experiments", *Radio Science*, Vol. 18, 321-327, (1983).
 - [93] Verlet, L. and Weis, J.J., "Equilibrium theory of simple liquids", *Phys. Rev. A.*, 5, 939-952, (1972)
 - [94] Viscek, T. Fractal Growth Phenomena, (World Scientific, New Jersey, 1992).
 - [95] Wang, Y.M., and W. C. Chew, "Electromagnetic Scattering form a Cluster of Spheres", *IEEE Antennas and Propagation Society International Symposium*, Vol. 3, 929-932, 1992
 - [96] Waterman P.C. and Truell, Rohn, "Multiple Scattering of Waves", *Journal of Mathematical Physics*, Vo. 2, No. 4, 512-537, (1961)
-

- [97] Waterman, P.C., "Matrix formulation of electromagnetic scattering", *Proc. IEEE*, 53, 805-811, (1965)
- [98] Wen, B., Tsang, L., Winebrenner, D.P., and Ishimaru, A., "Dense medium radiative transfer theory : Comparison with experiment and applications to microwave remote sensing and polarimetry", *IEEE Trans. Geosci. Remote Sens.*, 28, 46-59, 1990
- [99] West, R. Gibbs, D., Tsang, L. and Fung, A.K., "Comparison of optical scattering experiments and the quasi-crystalline approximation for dense media", *J. Opt. Soc. Am.*, Vol. 11, No. 6, June 1994
- [100] Zurk, L. M., Tsang, L., Ding, K. H., and Winebrenner, D. P., "Monte Carlo Simulations of the Extinction Rate of Densely Packed Spheres with Clustered and Non-Clustered Geometries", *J. of the Opt. Soc. of Am.*, Vol. 12, No. 8, Aug. 1995 †
- [101] Zurk, L.M., Tsang, L., and Winebrenner, D.P., "Scattering Properties of Dense Media from Monte Carlo Simulations with Application to Active Remote Sensing of Snow", submitted to *Radio Science*, July 1995 †
- [102] Zurk, L.M., Tsang, L., Winebrenner, D.P., Shi, Jiancheng, and Davis, Robert E., "Electromagnetic Scattering Calculated from Pair Distribution Functions Retrieved from Planar Snow Sections", submitted to *IEEE Trans. Geosci. Remote Sens.*, December 1995 †

† Portions of this publication have been reproduced in this thesis.

VITA

B.S. Computer Science	University of Massachusetts Amherst, Ma, 1985
M.S. Electrical and Computer Engineering	Northeastern University Boston, Ma. 1991

Professional Experience

1991 - 1995	Research Assistant, <i>Applied Physics Laboratory</i> , Instructor/Teaching Assistant, <i>Electrical Engineering Dept.</i> University of Washington, Seattle, Wa.
Summer 1991	Development Engineer, <i>BOSE Corporation</i> , Framingham, Ma.
1989 - 1991	Research/Teaching Assistant, <i>Northeastern University</i>
Summer 1990	Microwave Engineer, <i>Varian Associates</i> , Beverly, Ma.
1985 - 1989	Senior Software Engineer, <i>NOVA Biomedical</i> , Waltham, Ma.
1986 - 1991	Instructor, <i>Needham Adult Education</i> , Needham, Ma.
1983 - 1985	Research/Teaching Assistant, <i>University of Massachusetts</i>

Honors and Awards

Young Scientist Award	1995, URSI Commission B Symposium on Electromagnetic Theory St. Petersburg, Russia
Pew Teaching Leadership Award	1995
Lyall Zickrick Fellowship	1995
Sarah Denny Fellowship	1993

PUBLICATIONS : JOURNAL PAPERS

Zurk, L.M., Tsang, L., Winebrenner, D.P., Shi, Jiancheng, and Davis, Robert E., Electromagnetic Scattering Calculated from Pair Distribution Functions Retrieved from Planar Snow Sections, submitted to IEEE Trans. Geosci. Remote Sens., December 1995

Zurk, L.M., Tsang, L., and Winebrenner, D.P., Scattering Properties of Dense Media from Monte Carlo Simulations with Application to Active Remote Sensing of Snow, submitted to Radio Science, July 1995

Barabanenkov, Yu. N., Zurk, L.M. and Barabanenkov, M. Yu., Solution for modified radiative transfer equation near resonance scattering, submitted to Journal of Electromagnetic Waves and Applications, October 1995

Zurk, L.M. and Plant, W.J., Comparison of Actual and Simulated SAR Spectra of Ocean Waves Using SAXON-FPN Measurements, accepted for publication in the Journal of Geophysical Research, June 1995

Barabanenkov, Yu. N., Zurk, L.M. and Barabanenkov, M. Yu., Poynting's Theorem and Electromagnetic Wave Multiple Scattering in Dense Media Near Resonance, Journal of Electromagnetic Waves and Applications, Vol. 9, No. 11, pp 1393-1419, 1995

Zurk, L.M., Tsang L., Ding, K.H., and Winebrenner, D.P., Monte Carlo Simulations of the Extinction Rate of Densely Packed Spheres with Clustered and Non-Clustered Geometries, Journal of the Optical Society of America, August 1995, Vol. 12, No. 8, 1771-1781

Ding, K.H., Zurk, L.M., and Tsang, L., Pair Distribution Functions and Attenuation Rates for Sticky Particles in Dense Media, *Journal of Electromagnetic Waves and Applications*, Dec. 1994, Vol. 8, No. 12

Zurk, L.M. and Serafim, P.E., Relativistic Electron Motion in a Resonant Cavity with Time Varying and Inhomogeneous Magnetic Fields, *Journal of Electromagnetic Waves and Applications*, Jan. 1994, Vol. 8, No. 1, pp. 129-144

Barabanenkov, Yu. N. and Zurk, L.M., Radiative Transfer with Time Delay Near Resonance Scattering : Wave Energy Transport Velocity Approximation, *Turkish Journal of Physics*, 1994, Vol. 18, p. 978

PUBLICATIONS : PATENT

Rodamista, G., Dalke, D. and Zurk, L., "Modular Analyzer for Biomedical Fluids", Filed Sept. 18, 1989, Serial # 408696

PUBLICATIONS : CONFERENCE PAPERS

Zurk, L.M., Tsang, L., Shi, Jiancheng, and Davis, Robert E., Electromagnetic Scattering Based on Pair Distribution Functions Retrieved from Planar Snow Sections, submitted to 1996 IEEE International Geoscience and Remote Sensing Symposium, Lincoln, Nebraska, May 1996

Plant, W.P. and Zurk, L.M., Dominant Wave Directions Observed in SAR Imagery, 1995 IEEE International Geoscience and Remote Sensing Symposium, Florence, Italy, July 1995

Zurk, L. M., Tsang, L., and Winebrenner, D.P., Analysis of the Phase Matrix Obtained from Monte Carlo Simulations of Clustered and Non-Clustered Spheres, 1995 Progress in Electromagnetic Research Symposium, Seattle, Wa, July 1995

Grenfell, T. C., Wensnahan, M.R., Winebrenner, D.P., and Zurk, L.M., Passive Microwave and Infrared Observations of New and Young Sea Ice - The 1994 CRREL Pond Experiment, 1995 Progress in Electromagnetic Research Symposium, Seattle, Wa, July 1995

Barabanenkov, Yu. N., Zurk, L.M., and Barabanenkov, M. Yu., Solution for Modified Transfer Equation Near Resonance Scattering, 1995 Progress in Electromagnetic Research Symposium, Seattle, Wa, July 1995

Zurk, L.M., Modified Radiative Transfer Theory for Wave Multiple Scattering Near Resonance and Experiments on Pulse Transmission Through Dense Strongly Scattering Medium, 1995 URSI International Symposium on Electromagnetic Theory, St. Petersburg, Russia, May 1995

Zurk, L.M. and Plant, W.J., Two-Dimensional Simulations of SAR Imagery of Ocean Waves, IEEE International Geoscience and Remote Sensing Symposium, Vol. 4, p 2029-2031, Pasadena, Ca., August 1994

Zurk, L.M., Ding, K.H., Tsang, L., and Winebrenner, D.P., Monte Carlo Simulations of the Extinction Rate of Densely Packed Spheres with Clustered and Non-Clustered Geometries Based on Solution of Maxwell's Equations, 1994 IEEE International Geoscience and Remote Sensing Symposium, Vol. 1, p 535, Pasadena, Ca., Aug. 1994

Zurk, L.M. and Tsang, L., Monte Carlo Simulations of the Extinction Rate of Densely Packed Spheres Based on Solution of Maxwell's Equations, 1994 IEEE AP-S International Symposium and URSI Radio Science Meeting, Seattle, Wa., vol. 1, p 658-661, June 1994

Barabanenkov, Yu. N., and Zurk, L.M., Poynting's Theorem and Electromagnetic Wave Multiple Scattering in Dense Media Near Resonance, 1994 IEEE AP-S International Symposium and URSI Radio Science Meeting, Seattle, Wa., June 1994

Zurk, L.M. and Plant, W.J., Simulations of SAR Imagery of the Ocean Compared with Data, Proceedings of 1993 IEEE Oceans Symposium, Vol. 3, p 304-309, Victoria, B.C., Canada, Oct. 1993

Ding, K.H., Zurk, L.M., and Tsang, L., Pair Distribution Functions and Attenuation Rates for Dense Discrete, Random Media with Sticky Particles, Progress in Electromagnetic Research Symposium, p.436, Pasadena, Ca., July 1993

Zurk, L.M. and Plant, W.J., Results of Simulations of SAR Imagery from SAXON Data, SAXON-FPN Workshop, Seattle, Wa., Sept. 1992

Zurk, L.M., Davis, D., Njoku, E.G., Tsang, L. and Hwang, J., Inversion of Parameters for Semiarid Regions by a Neural Network, 1992 IEEE International Geoscience and Remote Sensing Symposium, Vol. 2, p. 1075-1077, Houston, Tx, May 1992

Treado, T.A., Zurk, L.M., Smith, R.S., Hansen, T.A., Jenkins, D.J. and Thomas, G.E., Experimental Results of Power Combining and Phase-Locking Magnetrons for Accelerators Applications, Intl. Electron Dev. Mtg. Tech. Digest, p 541-544, San Francisco, Ca., Dec. 1990

Zurk, L.M., Nolen, S. and Feetham, E., TA Program Evaluation as a Tool for Improving Graduate Programs, 5th National Conference on Education and Employment of Graduate Teaching Assistants, Denver, Colorado, November 1995